

LA-UR-20-29951

Approved for public release; distribution is unlimited.

Title: In-situ Radiography of Hydrogen Porosity Growth and Development in Aluminum Welds.

Author(s): Barraza, Alexyia Marie

Intended for: Thesis presented in partial fulfillment of the requirements for the Degree Master of Science through Ohio State University

Issued: 2021-05-11 (rev.3)

Disclaimer:

Los Alamos National Laboratory, an affirmative action/equal opportunity employer, is operated by Triad National Security, LLC for the National Nuclear Security Administration of U.S. Department of Energy under contract 89233218CNA000001. By approving this article, the publisher recognizes that the U.S. Government retains nonexclusive, royalty-free license to publish or reproduce the published form of this contribution, or to allow others to do so, for U.S. Government purposes. Los Alamos National Laboratory requests that the publisher identify this article as work performed under the auspices of the U.S. Department of Energy. Los Alamos National Laboratory strongly supports academic freedom and a researcher's right to publish; as an institution, however, the Laboratory does not endorse the viewpoint of a publication or guarantee its technical correctness.

In-situ Radiography of Hydrogen Porosity Growth and Development in Aluminum
Welds.

Thesis

Presented in Partial Fulfillment of the Requirements for the Degree Master of Science in
the Graduate School of The Ohio State University

By

Alexyia M. Barraza

Graduate Program in Welding Engineering

The Ohio State University

2021

Thesis Committee

Dr. Carolin Fink, Advisor

Dr. Boian Alexandrov

Dr. Carl E. Cross

Copyrighted by
Alexyia Marie Barraza
2020

Abstract

In aluminum welding, hydrogen contamination is the main cause of the welding defect, porosity. Porosity in welds can adversely affect the mechanical properties such as tensile strength, fatigue life and ductility. There have been a variety of solutions to help reduce porosity in aluminum welds including finding the source of hydrogen. However, in some cases the amount of hydrogen may be drastically reduced but impossible to completely eliminate. Another approach to this issue is to understand where a pore originates and how it moves and grows within the weld pool. This information may lead to a more innovative method for pore elimination during gas tungsten arc (GTA) welding of aluminum.

In-situ aluminum weld experiments were set-up to observe the porosity formation in aluminum welding. Aluminum alloys 1100, 4047, and 6061 were autogenously gas tungsten arc welded in a chamber while real-time digital radiography was performed. Hydrogen was added in parts-per-million through an argon-hydrogen shielding gas. The shielding gas hydrogen was varied between 0 and 1000 ppm of hydrogen and three travel speeds were tested: 1.69 mm/s, 2.54 mm/s and 3.39 mm/s.

The smallest pore measured was roughly 90 μ m, demonstrating this method of in-situ observation to be a useful way to monitor macro-porosity in aluminum welds. Micro-pores could be seen near the surface of weld pool but it was difficult to see their shape or

movement. The amount of hydrogen added through the shielding gas played an important role in macro-pore growth and well as travel speed. Pore growth rate increased with increase in hydrogen saturation and slower travel speed.

In Alloy 1100 macro-pores originated at the bottom of the weld pool, near the trailing portion of the weld pool in an elliptical shape. Macro-pores in Alloy 6061 originated at the leading edge of the weld pool, near the surface. Once the macro-pores reached a favorable size, they were then swept back to the trailing edge of the weld pool. A single macro-pore was observed during welding of Alloy 4047 indicated pore formation and movement similar to that of the macro-pores in Alloy 6061. Regardless of Alloy, macro-porosity remained on the outer “still” fusion boundary of the weld pool. Pores did not enter the bulk of the weld pool. Pore movement upward is influenced by buoyancy and fluid flow.

Micro-pores became fully engulfed with periodic oscillation of the weld pool leading to banding. The banding followed the shape of the weld pool. In Alloy 1100, when macro-pores were partially engulfed, this resulted in elliptical-shaped pores growing in the direction of the weld. Macro-pores in Alloy 6061 were not partially engulfed; when they were fully engulfed the macro-pores remained circular in shape.

Dedication

To Maria Isabela Perez, be brave.

Acknowledgments

This work was performed under DOE contract and internal LANL funding provided by Mike Steinzig. Special thanks to J.D. Montalvo and Jessica Lopez for metallographic support; Tim Baker for gravimetric measurement support; Chris Stull, Amber DeLaO, Timothy Ickes, and Kelley Vansyoc for radiographic technical support; and Jesse Martinez for your insight and welding support.

I would like to thank my family for accompanying me on this journey. I would not be where I am today without your helping hand after every stumble, your encouragement to take a breath at the top of every hill, and the reminder to look at the map when the trail wasn't clear.

Carl E. Cross, I am grateful to have had the chance to get to know you. Your guidance and patience is endless and reassuring. Your technical advice is whole-heartedly appreciated and was instrumental in the success of this study.

Thank you Dr. Carolin Fink for giving me the opportunity to work with you. I appreciate your guidance, feedback and support through this study.

Vita

2011..... B.S. Mechanical Engineering,
New Mexico Institute of Mining and Technology

2017..... A.S. Welding Technology,
Central New Mexico Community College

2013 to present..... Grad. Student, Welding Engineering,
The Ohio State University

Fields of Study

Major Field: Welding Engineering

Table of Contents

Abstract	ii
Dedication	iv
Acknowledgments	v
Vita	vi
List of Tables	ix
List of Figures	x
Chapter 1. Introduction/Objective	1
Chapter 2. Background	3
Welding Process.....	3
Hydrogen Solubility.....	8
Origin of Pores (nucleation).....	10
Growth of Pores	11
Threshold Hydrogen Levels.....	14
In-Situ Radiography.....	16
Chapter 3. Experimental	19
In-situ Videos.....	28
Gravimetric Testing	29
Metallography	31
Chapter 4. Results	33
In-Situ Radiography Data	33
Pore Formation and Migration.....	34

Pore Growth	51
Diffusional Pore Growth.....	55
Percent Porosity	59
Engulfment/Banding	71
Effervescence	73
Chapter IV. Conclusion	80
Radiographic Technique.	80
Influence of shielding gas hydrogen and travel speed.	80
Pore Formation.....	81
Pore Movement.	82
Pore Growth.	83
Engulfment.....	83
Bibliography	85
Appendix A. Sample Weld Parameters	89
Appendix B. Additional Data	91

List of Tables

Table 1: Prediction of threshold hydrogen content for pore formation based upon Woods [13] plots calculated for an arc contamination level of 400 ppm hydrogen.	16
Table 2: Nominal Aluminum Alloy Chemical Composition.....	19
Table 3: Gas tungsten arc welding parameters	21
Table 4: Controlled shielding gas mixtures of Ar and Ar-0.1% H_2	22
Table 5: Operating parameters used for digital radiography.	23
Table 6: Condensed version of aluminum samples welded during this study.	27
Table 7: Alloy 6061 tabulation of final pore diameter and average growth rate based on in-situ data.....	53
Table 8: Percent Porosity for welded samples based on metallography and gravimetric testing.....	60
Table 9: Weld Sample Parameters	90

List of Figures

Figure 1: Schematic of gas tungsten arc welding process [4].....	4
Figure 2: A schematic representation of a gas tungsten welding arc including the non-consumable electrode and the weld pool, showing important transport processes occurring within the system [5].	5
Figure 3: Buoyancy induced fluid flow in the weld pool [4].....	7
Figure 4: The electromagnetic force in the arc and weld pool [4].....	7
Figure 5: Surface and subsurface fluid flow in the weld pool. a) Negative surface tension temperature coefficient; b) positive surface tension temperature coefficient [8].	7
Figure 6: Solubility of hydrogen in aluminum [10].....	8
Figure 7: Schematic representation of the forces acting on the particle in the vicinity of the solid-liquid interface [23].....	13
Figure 8: Effect of weld pool convection on weld porosity: A) convection pattern favoring trapping of gas bubbles; B) convection pattern favoring removal of gas bubbles [6].....	14
Figure 9: Data from the work of Woods [13] showing amount of weld metal hydrogen, based upon gravimetric analysis, as a function of hydrogen added to shielding gas on different aluminum base plates and filler alloys.	15
Figure 10: Side view of experimental set-up in radiography chamber.....	23
Figure 11: Photograph of experimental set-up showing moving aluminum plate specimen, GTA welding torch and stationary aligned x-ray source (red).	24
Figure 12: Side view of welded plate specimen indicating the approximate location and size of each sample.	25
Figure 13: Density determination set-up with analytical balance and density kit [34]. ...	30
Figure 14: Typical weld cross-section showing bead shape of edge weld.	32
Figure 15: Alloy 1100 welded using 500 ppm shielding gas hydrogen at a travel speed of 1.69 mm/s, shows pore formation at the bottom of the weld pool and pore gas escape...	35
Figure 16: Alloy 1100 welded sample using 333 ppm shielding gas hydrogen at travel speed of 1.69 mm/s, shows pore formation at the bottom of the weld pool and elongated pore growth.	37
Figure 17: Alloy 4047 welded samples using 667 ppm shielding gas hydrogen at travel speed of 2.54 mm/s, shows micro-porosity at the leading and trailing edge of the weld pool.	39
Figure 18: Alloy 4047 welded sample using 1000 ppm shielding gas hydrogen at travel speed of 2.54 mm/s, shows pore movement.	40
Figure 19: Alloy 6061 welded sample using 667 ppm shielding gas hydrogen at a travel speed of 1.69 mm/s, shows pore escaping in the final frame and a steady stream of micro-pores solidified in the weld metal.	42
Figure 20: Alloy 6061 welded sample using 667 ppm shielding gas hydrogen at a travel speed of 1.69 mm/s, shows the coalescence of two pores in the weld pool.	43

Figure 21: Alloy 6061 welded sample using 667 ppm shielding gas hydrogen at a travel speed of 3.39 mm/s, shows macro-pore growth via hydrogen coalescence from micro-pores, shown underneath the black arrow, near the macro-pore.....	44
Figure 22: Alloy 6061 welded sample using 833 ppm shielding gas hydrogen at a travel speed of 1.69 mm/s, shows micro-pores formed at the trailing edge of the weld pool pointed out above the white arrow.....	46
Figure 23: Micrographs showing pore shape in a) Alloy 1100, b) Alloy 4047, and c) Alloy 6061.	48
Figure 24: Schematic demonstrating different fluid flow patterns and macro-pore formation in aluminum Alloy welds a) 1100 versus b) 6061 and 4047.....	49
Figure 25: The effect of travel speed can be seen with in-situ data pore measurements when comparing the macro- pore area (mm^2) observed during the different travel speeds at a) 333 ppm of shielding gas hydrogen and b) 667 ppm of shielding gas hydrogen.	52
Figure 26: The effect of shielding gas hydrogen can be seen with in-situ data pore measurements when comparing the macro- pore area (mm^2) observed during the amounts of shielding gas hydrogen at a travel speed of 2.5 mm/s.	53
Figure 27: Schematic showing the exposure time the weld pool experiences.....	55
Figure 28: Schematic of hydrogen diffusion controlled pore formation [42].....	58
Figure 29: Radial pore growth in Alloy 6061 over time at travel speed 2.5mm/s and varying levels of shielding gas hydrogen.....	59
Figure 30: Alloy 1100 at travel speed of 3.39 mm/s using a) 0 ppm of shielding gas hydrogen with 0.055% porosity, b) 333 ppm of shielding gas hydrogen with 0.82% porosity, c) 667 ppm of shielding gas hydrogen with 1.12% porosity, and d) 1000 ppm of shielding gas hydrogen with 1.89% porosity.	62
Figure 31: Volumetric percent porosity calculated from gravimetric testing showing the results from varying the amount of shielding gas hydrogen at different travel speeds in Alloy 1100.	63
Figure 32: Alloy 4047 at travel speed of 3.39 mm/s with the following levels of shielding gas hydrogen: a) 0 ppm contained 0.048% porosity, b) 333 ppm contained 0.47% porosity, c) 667 ppm contained 0.94% porosity , and d) 1000 ppm contained 0.50% porosity.	65
Figure 33: Volumetric percent porosity using various amounts of shielding gas hydrogen at different travel speeds in Alloy 4047.....	66
Figure 34: Alloy 6061 at travel speed of 3.39 mm/s with the following levels of shielding gas hydrogen: a) 0 ppm, b) 333 ppm, c)667 ppm , and d) 1000 ppm.....	68
Figure 35: Volumetric percent porosity using various amounts of shielding gas hydrogen at different travel speeds in Alloy 6061.....	69
Figure 36: Area percent porosity using various amounts of shielding gas hydrogen on different alloys at a travel speed of 3.39 mm/s.	70
Figure 37: Volumetric percent porosity using various amount of shielding gas hydrogen on different alloys at a travel speed of 3.39 mm/s.	70
Figure 38: Welded sample using 667 ppm of shielding gas hydrogen, is an Alloy 1100 showing pore banding forming and solidification.	73

Figure 39: Alloy 4047 showing effervescence at the leading and trailing edge of the weld pool surface.	75
Figure 40: Photograph of 1100 weld metal, exhibiting sub-surface porosity with varying amounts of shielding gas hydrogen at a travel speed of 3.39 mm/s.	76
Figure 41: Photograph of 4047 weld metal, exhibiting sub-surface porosity with varying amounts of shielding gas hydrogen at a travel speed of 3.39 mm/s.	77
Figure 42: Photograph of 6061 weld metal, exhibiting sub-surface porosity with varying amounts of shielding gas hydrogen at a travel speed of 3.39 mm/s.	78
Figure 43: Alloy 1100 welded sample welded with 0 ppm of hydrogen at a) 1.69 mm/s and b) 3.39 mm/s.....	92
Figure 44: Alloy 1100 welded using 167 ppm of shielding gas hydrogen at 1.69 mm/s.	93
Figure 45: Alloy 1100 welded using 333 ppm of shielding gas hydrogen at 1.69 mm/s.	94
Figure 46: Alloy 1100 welded using 333 ppm of shielding gas hydrogen at 1.69 mm/s.	95
Figure 47: Alloy 1100 welded using 333 ppm of shielding gas hydrogen at a) 1.69 mm/s and b) 3.39 mm/s.....	96
Figure 48: Alloy 1100 welded using 500 ppm of shielding gas hydrogen at 1.69 mm/s.	97
Figure 49: Alloy 1100 welded using 667 ppm of shielding gas hydrogen at 1.69 mm/s.	98
Figure 50: Alloy 1100 welded using 667 ppm of shielding gas hydrogen at 2.54 mm/s.	99
Figure 51: Alloy 1100 welded using 667 ppm of shielding gas hydrogen at 3.39 mm/s.	100
Figure 52: Alloy 1100 welded using 833 ppm of shielding gas hydrogen at 1.69 mm/s.	101
Figure 53: Alloy 1100 welded using 1000 ppm of shielding gas hydrogen at 3.39 mm/s.	102
Figure 54: Alloy 4047 welded using 0 ppm of shielding gas hydrogen at a) 2.54 mm/s and b) 3.39 mm/s.....	103
Figure 55: Alloy 4047 welded using 333 ppm of shielding gas hydrogen at a) 2.54 mm/s and b) 3.39 mm/s.....	103
Figure 56: Alloy 4047 welded using 667 ppm of shielding gas hydrogen at a) 2.54 mm/s and b) 3.39 mm/s.....	103
Figure 57: Alloy 4047 welded using 1000 ppm of shielding gas hydrogen at a) 2.54 mm/s and b) 3.39 mm/s.....	104
Figure 58: Alloy 6061 welded using 0 ppm of shielding gas hydrogen at 1.69 mm/s ...	105
Figure 59: Alloy 6061 welded using 0 ppm of shielding gas hydrogen at 2.54 mm/s. ..	105
Figure 60: Alloy 6061 welded using 0 ppm of shielding gas hydrogen at 3.39 mm/s. ..	106
Figure 61: Alloy 6061 welded using 167 ppm of shielding gas hydrogen at 1.69 mm/s.	106
Figure 62: Alloy 6061 welded using 167 ppm of shielding gas hydrogen at 2.54 mm/s.	107
Figure 63: Alloy 6061 welded using 333 ppm of shielding gas hydrogen at 1.69 mm/s.	108
Figure 64: Alloy 6061 welded using 333 ppm of shielding gas hydrogen at 2.54 mm/s.	109

Figure 65: Alloy 6061 welded using 333 ppm of shielding gas hydrogen at 3.39 mm/s.	110
Figure 66: Alloy 6061 welded using 500 ppm of shielding gas hydrogen at 1.69 mm/s.	111
Figure 67: Alloy 6061 welded using 500 ppm of shielding gas hydrogen at 2.54 mm/s.	112
Figure 68: Alloy 6061 welded using 667 ppm of shielding gas hydrogen at 1.69 mm/s.	113
Figure 69: Alloy 6061 welded using 667 ppm of shielding gas hydrogen at 3.39 mm/s.	114
Figure 70: Alloy 6061 welded using 833 ppm of shielding gas hydrogen at 1.69 mm/s.	115
Figure 71: Alloy 6061 welded using 1000 ppm of shielding gas hydrogen at 3.39 mm/s	116

Chapter 1. Introduction/Objective

While porosity in aluminum welds continues to be a difficult problem for industry, there has been little research performed to understand where it originates and how it moves and grows within the weld pool. Weld porosity, found in many different metal alloy systems, is normally related to a drop in solubility of interstitial elements during solidification. Pores can also form from keyhole and arc instabilities, the partial pressure of dissolved interstitials are still involved. Porosity in aluminum is specifically associated with hydrogen contamination [1], but how and where it nucleates, moves, and grows has been left to speculation.

Most structural aluminum welds are evaluated according to specifications that limit the amount and/or size of pores that can be tolerated. Uniformly distributed porosity itself does not necessarily lower mechanical properties, aside from reducing load-bearing area [2]. But at high volume levels or for closely spaced linear porosity, problems with crack initiation, propagation, and leak-tightness may be encountered, particularly found in fatigue loading. Post-weld radiography and cross-sectional metallography are common tools used to characterize weld porosity. However, these techniques do not show the origin of pores and indicate only the location where pores were over-grown (i.e. engulfed) by the advancing solid/liquid interface. Additionally, there is no indication of the number of pores that escaped.

This in-situ study is unique in that it used radiography to examine porosity caused by controlled additions of hydrogen through the shielding gas. The thin section coupons used here (3 mm thick) were edge welded using autogenous gas tungsten welds that allowed for better resolution of pores when viewed normal to the weld in-situ. Although, narrow weld pools also have a down side in that they do not necessarily represent what happens in wide, 3-dimensional weld pools. Pore behavior observed showed micro-pores could not be resolved, thus what happens to interdendritic porosity remains unknown. For larger pores, macro-pores, their behavior in the weld pool has been documented and quantified here, thus ending the need for speculation. The three aluminum alloys studied (1100, 4047, and 6061) gave insight into their distinctive macro-pore shape, the macro-pore behavior during growth, and migratory pattern.

Metallography and gravimetric analysis performed on each welded coupon yielded an approximate amount of absorbed hydrogen in the weld metal based on the percent area and percent volumetric porosity. This data allowed for a comparison of the effects of welding travel speed and the parts-per-million of shielding gas hydrogen on each alloy welded.

This mode of observation demonstrated the useful means of monitoring porosity through in-situ radiography. Macro-pores were the primary focus of this study, demonstrating how real-time radiography may be effectively used to improve our understanding of aluminum porosity.

Chapter 2. Background

Welding Process

Gas tungsten arc welding (GTAW) is a part of the group of arc welding processes that produces an electric arc to heat, melt and join metals. GTAW uses a non-consumable tungsten electrode to strike an arc on the workpiece. Current is carried and sustained through the tip of the tungsten electrode to the workpiece. GTA welding equipment consists of a welding torch, non-consumable tungsten electrode, welding power supply, a source of inert gas, and optional filler wire. Although a constant current welding power supply is used in GTAW, the polarity may be changed to obtain the desired welding characteristics. In general, aluminum welding is conducted on alternating current (AC) due to the arc cleaning action produced on the surface of the workpiece during the electrode positive half of the AC cycle to remove the aluminum oxide layer from the surface of the material. The electrode, arc, and weld pool is shielded with inert gas. This gas shield protects these items from contamination, oxidation, corrosion, and contributes to the required arc characteristics [3]. In this study, autogenous GTA welds were performed on single plates. An autogenous weld does not use filler metal thus removing the influences it has on fluid flow, solidification, and contamination in the weld pool. A schematic of the GTAW process is shown in Figure 1.

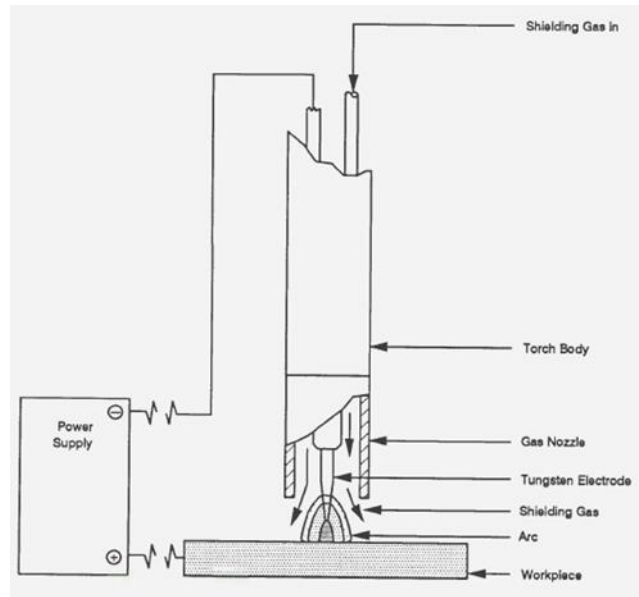


Figure 1: Schematic of gas tungsten arc welding process [4]

As thermal energy is transferred to the workpiece via the arc, there is important transport phenomena occurring in the GTA welding system [5]. Figure 2 shows the schematic representation of this energy transport showing heat and current flux distributions to the weld pool, interaction of the arc with the free surface, convective heat transfer due to fluid flow in the weld pool, thermal conduction into the solid workpiece, convective and radiative heat losses, heat and mass losses due to vaporization, transient solidification and melting, and electromagnetic stirring due to the divergent current path [5].

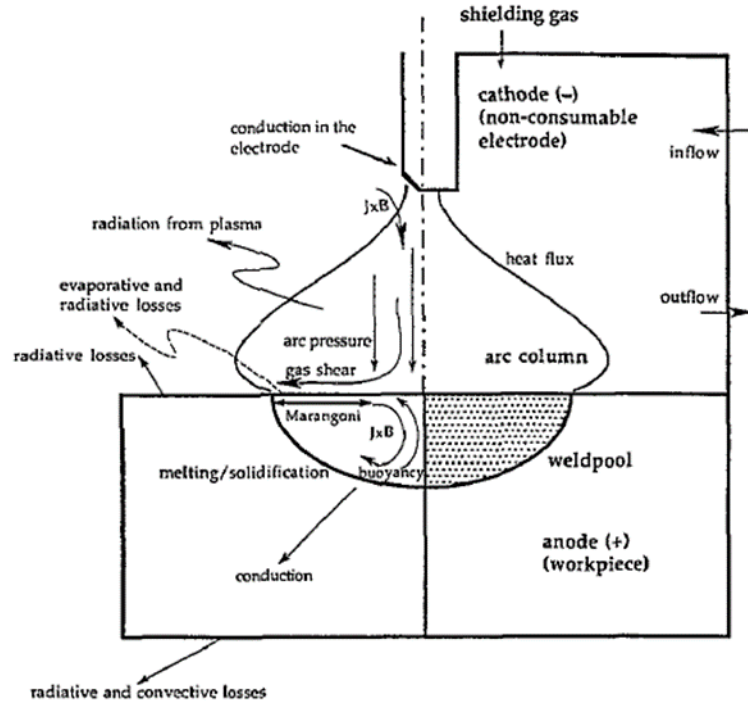


Figure 2: A schematic representation of a gas tungsten welding arc including the non-consumable electrode and the weld pool, showing important transport processes occurring within the system [5].

The weld pool, a complex area experiencing convective heat transfer due to fluid flow, is heavily influenced by three driving forces: buoyancy, electromagnetic, and surface-tension. The competition between these forces dictate the fluid flow in the weld pool. Buoyancy force causes fluid flow in a weld pool to be similar to that seen in Figure 3. This is caused by temperature gradients within the weld pool [6]. Fluid flow driven by the electromagnetic force, Lorentz force, from the current flow crossed by the magnetic field cause the weld pool to circulate radially inward and downward, transferring the centrally, high temperature fluid to the bottom of the weld pool [4].

Surface tension driven fluid flow, Marangoni fluid flow, occurs when the surface tension gradient exists on the surface of a liquid and the fluid is drawn along the surface from the regions of lower surface tension to those of higher surface tension. Surface tension is temperature dependent and due to the large temperature gradients on the weld pool surface, it creates surface tension gradients [7]. For weld pools with a decreasing surface tension as temperature increases, the surface tension is the highest at the coolest part of the pool surface, the edges, while surface tension is the lowest on the hottest part of the pool surface, directly under the arc near the center of the pool, producing and outward surface fluid flow, represented in Figure 5(a). This fluid flow pattern transfers heat efficiently from the center of the weld pool, hottest region, to the edges, cooler regions, [7]. Figure 5(b) shows a positive surface tension temperature coefficient that is typically observed when there are certain surface active element in molten metals. These surface active elements segregate preferentially to the surface of the liquid metal and lower the magnitude of the surface tension. The addition of a small concentration of the surface active elements can change the temperature dependence of the surface tension causing the surface tension to increase with increasing temperature. The surface tension will be the highest near the center of the weld pool causing the fluid to flow inward along the surface of the weld pool and then down, efficiently transferring heat to the bottom of the weld pool [7].

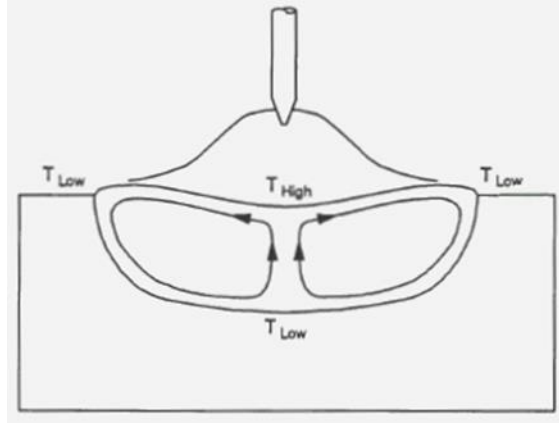


Figure 3: Buoyancy induced fluid flow in the weld pool [4].

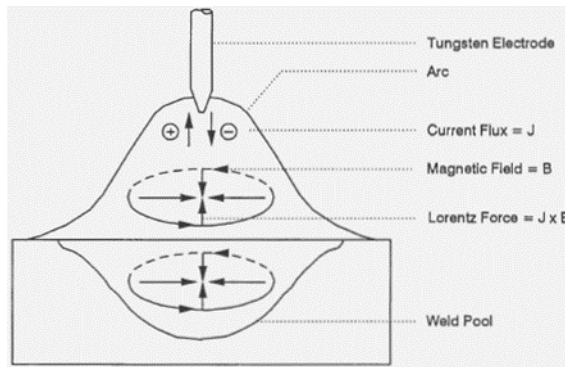


Figure 4: The electromagnetic force in the arc and weld pool [4].

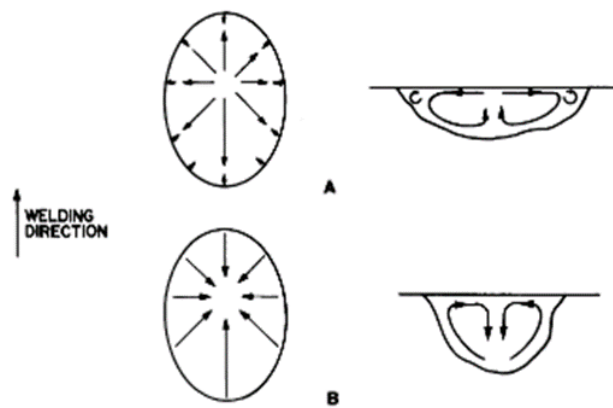


Figure 5: Surface and subsurface fluid flow in the weld pool. a) Negative surface tension temperature coefficient; b) positive surface tension temperature coefficient [8].

Hydrogen Solubility

Hydrogen contamination can come from many sources, including shielding gas moisture and hydrated surface oxides on wire and weld joint [9]. Figure 6 shows the solubility of hydrogen in pure aluminum with respect to temperature. It can be seen at the transition from liquid to solid, there is a significant drop in hydrogen solubility.

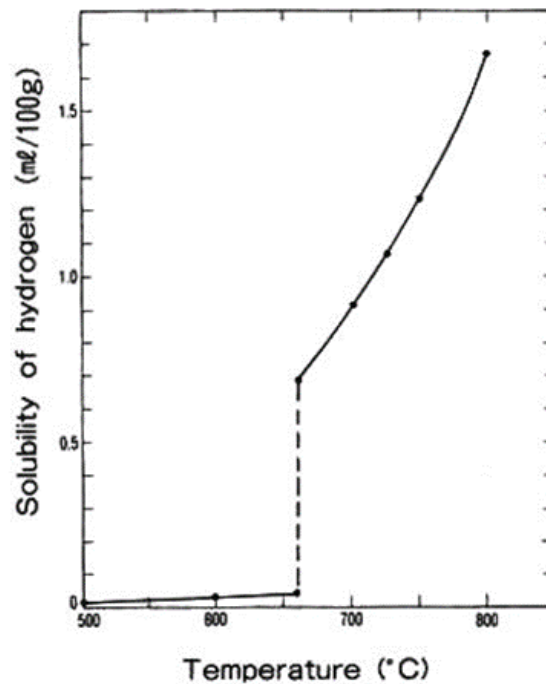


Figure 6: Solubility of hydrogen in aluminum [10].

Limited knowledge is available regarding how effectively hydrogen is transferred to the weld pool or how much hydrogen can be tolerated before getting porosity. It is clear however, that aluminum weld metal exhibits a much higher solubility than equilibrium predictions made using Sievert's Law [11], [10]. The equilibrium solubility

of hydrogen in a pure aluminum is used to determine the dissolved hydrogen content at equilibrium, H [10]:

$$H = K\sqrt{p_{H_2}} \quad \text{Equation 1}$$

where $\log K = [(-2760)/T + 2.796]$, T = temperature in Kelvin and p_{H_2} = partial pressure of diatomic hydrogen and concentration in ml/100g.

Assuming the weld pool is superheated to approximately 800°C, commonly observed in aluminum welds [12], Equation 1 predicts a solubility of 0.25 ml/100g at a partial pressure of 0.04 atm. This solubility is significantly lower when compared against observed values of 1-2 mL/100g reported by Woods [13]. This large deviation from equilibrium has also been observed in ferrous systems and is believed to be associated with the monatomic form of interstitial in the arc plasma, as opposed to the diatomic form assumed in Sievert's Law [14]. Also, high weld pool surface temperatures approaching the vaporization temperature [14] may account for higher solubility. High concentrations of hydrogen at the pool surface, related to this high temperature, can then become mixed into the bulk liquid through convection.

Additional factors can affect hydrogen pick-up in the weld pool, such as weld parameters that influence arc and weld pool size [13]. Large pool surface area allows more hydrogen to enter (or escape) the weld pool. Arc-pool exposure time, determined by weld travel speed, also affects this. Travel speed also limits the time for nucleation, growth, and escape. Buoyancy forces act to cause some pores to migrate against gravity

and escape, depending upon the orientation of welding. Some porosity evaluation tests require that welds are made over-head to avoid escape. Material composition may also have a large effect [14].

Origin of Pores (nucleation)

Porosity formation can be influenced by solidification and can reasonably be assumed to originate first between dendrites, since this is where hydrogen is concentrated during solidification due to partitioning of interstitial atoms into the liquid between the dendrites [15]. It has been suggested that interdendritic micro-pores ($< 10 \mu\text{m}$ dia.) may be washed ahead of the solidification front where they grow and coalesce [16]. The partition coefficient for hydrogen in pure aluminum is small, $k = [H]_S/[H]_L = 0.05$ [1], which represents a significant drop in solubility during solidification. In order for pores to nucleate, sufficient hydrogen super-saturation is required to overcome surface tension and external pressure. Internal pressures on the order of 1,760 atm have been proposed as needed for heterogeneous liquid fracture [17]. The interdendritic pressure drop associated with solidification aids in achieving this condition. Based upon this fracture strength, a calculated weld pool hydrogen concentration of 1.6 ml/100g is needed to nucleate micro-pores at the base of dendrites in Alloy 6060 aluminum [16].

Many researchers have studied the effects of porosity on mechanical properties. Rudy et. al [18] found in their study of GTA welded aluminum alloys 2014 and 2219 an increase in porosity reduced tensile strength both in the transverse and longitudinal direction. Small amounts of porosity was found to negatively impact other mechanical

properties such as fatigue life and ductility as found by a study conducted on aluminum Alloy 7039 [19]. Pore size and distribution of porosity was reported to play a key role in the degradation of the mechanical properties [15]. The location of micro-porosity and macro-porosity present in weld metal impact the degree in which the mechanical properties are effected. For example, aligned and closely space macro-porosity in the weld proved to be more detrimental than randomly distributed macro-porosity [18]. Post-weld radiography and cross-sectional metallography are common tools used to characterize weld porosity. However, these techniques do not show the origin of pores and indicate only the location where pores were engulfed by the advancing solid/liquid interface. Additionally, there is no indication of the number of pores that escaped. Understanding the pore formation, growth, and movement in aluminum welds may lead to a more informed decision for minimizing porosity during the welding process.

Growth of Pores

Movement, Engulfment, and Escape. It is reasonable to assume that pores cannot move freely within the bulk of the weld pool, where fluid flow velocities of 0.1 meters per second have been estimated [20]. Associated drag and shear forces would tear macro-pores apart. Hence, they most likely reside next to the solid/liquid interface, in a diffuse unmixed region where flow velocities tend to zero [21]. The velocity of liquid motion must approach zero at the solid-liquid interface even when the bulk of the weld pool is in turbulent motion. But what causes pores to become overgrown by the advancing solid/liquid interface?

If pores behave in a manner similar to oxide particles, there exists a critical velocity, depending upon size, above which the drag force promotes engulfment [22] [23]. At the particle-S/L interface interaction, Figure 7 illustrates the velocities and force vectors found to be active on a particle near the solid-liquid interface where V_{SL} is the solidification velocity, V_L is the velocity induced by natural convection, F_D is the drag force, F_g is the force of gravity, F_L is lift force produced by the liquid flow parallel to the interface, F_Y is the interaction force between the particle and the solid-liquid interface [23]. The larger the oxide, the greater the drag force and the lower the critical velocity needed for engulfment. Applying this to the instance of a pore in the weld pool instead of a particle, if the pore is not engulfed, buoyancy works on the pore to move it against gravity, which may involve eventual escape at the pool surface. This outgassing, i.e. violent bursting of pores at the pool surface, can be observed when welding material with high hydrogen content.

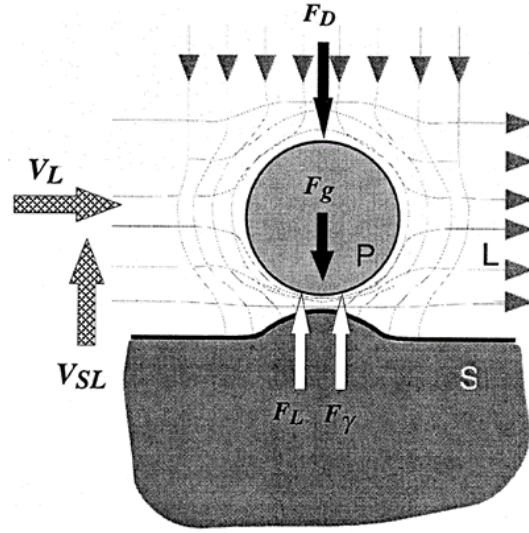


Figure 7: Schematic representation of the forces acting on the particle in the vicinity of the solid-liquid interface [23].

As will be shown in this study, the liquid flow pattern within the weld pool can also affect pore movement. Kou et. al [6] postulated in their study of weld pool convection the movement of pores as seen in Figure 8. Fluid flow as seen in Figure 8(A) is a product of low surface tension due to the lack of surface active elements, the fluid flows outward from the center of the weld pool then downwards to the weld root. If the fluid flows appears as that shown in Figure 8(A), the pores can be caught up by the solidification front and become pores in the solidified weld; not reducing weld porosity [6]. Fluid flow as seen in Figure 8(B) is a product of high surface tension due to the presence of surface active elements, the fluid flows inward along the surface of the weld pool toward the center and then downwards to the root of the weld. If the fluid flow appears as that shown in Figure 8(B) the pores would be swept in the upward direction

allowing the pores to reach the free surface and escape before being caught up by the solidification front; resulting in fewer pores trapped in the solidified weld [6].

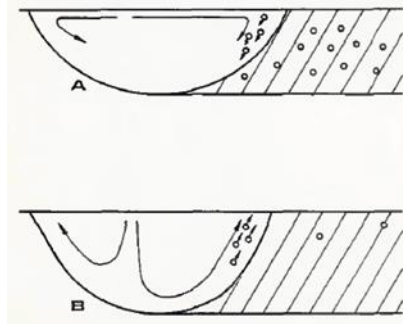


Figure 8: Effect of weld pool convection on weld porosity: A) convection pattern favoring trapping of gas bubbles; B) convection pattern favoring removal of gas bubbles [6].

Threshold Hydrogen Levels.

Woods [13] demonstrated that hydrogen solubility in aluminum welds increases with the square root of hydrogen partial pressure (Sievert-type relationship), and varies with alloy content, see Figure 9. He used the gravimetric method to analyze the hydrogen content in the weld metal. The gravimetric measurements yielded the total volume of hydrogen in the material-both weld metal and base metal were tested independently. Woods then compared the weld metal values to the base metal values to determine the amount of hydrogen absorbed in the weld metal from the arc. When the hydrogen content became greater than zero, this signaled that pores were present and thus indicated the contamination level needed for pore formation. Woods suggested that pores form when superheated and supercharged molten metal, located directly under the arc, is rapidly transferred to cooler regions of the pool leading to super-saturation. Figure 9 shows, that

regardless of alloy type, an increase in hydrogen input resulted in an increase in hydrogen absorption in the weld metal. This data was translated to the current study by assuming a higher hydrogen content in the shielding gas will yield a higher hydrogen content in the weld pool.

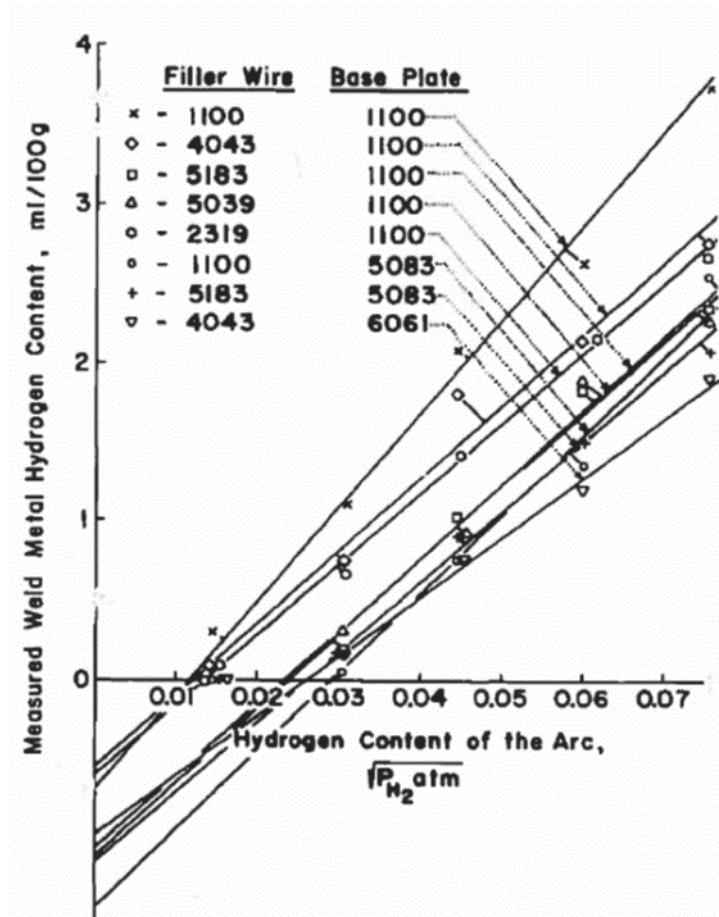


Figure 9: Data from the work of Woods [13] showing amount of weld metal hydrogen, based upon gravimetric analysis, as a function of hydrogen added to shielding gas on different aluminum base plates and filler alloys.

Table 1: Prediction of threshold hydrogen content for pore formation based upon Woods [13] plots calculated for an arc contamination level of 400 ppm hydrogen.

Welding Process	Aluminum Alloy	Threshold Hydrogen Content (mL/100g)
Autogenous GTA Weld [13]	2219	0.45
	Al + 6.5% Zn	0.5
	1100	0.7
	Al + 1% Mg	0.75
	3003	0.95
	5083	1.1
	Al+ 1% Zn	1.15
	Al + 6.5% Mg	1.25
	7039	2.3
GMA Weld [13]	1100/1100	0.7
	4043/6061	1.0
	5183/5083	1.2

A tabulation of critical hydrogen levels needed for pore formation, measured directly from Figure 9, are compared in Table 1 for different base and filler metal combinations [13]. The solubility of hydrogen in the weld metal was impacted by the chemical composition. However, from Figure 9, Alloy 1100 shows the greatest pick-up of hydrogen for a given exposure in the arc. And from Table 1, it shows that Alloy 1100 is among the easiest to nucleate pores. Based on this data, the current study should see the Alloy 1100 be the most susceptible to porosity as it has the greatest liquid solubility compared to other alloys with magnesium and zinc.

In-Situ Radiography

A challenging issue to overcome has been the direct observation of the sub-surface weld pool. Previous studies have used in-situ radiography to examine welding. Dixon et al. [24] in 1988 were among the first to report this technique. Placing an x-ray source above a moving GTA weld on a thin (0.9 mm) steel plate, and pre-stressed to

induce cracking, they observed porosity and solidification cracks. Done prior to the existence of digit movie cameras, they used a video tape cassette camera to record images directly off a phosphorous intensifier screen. Rokhlin and Guu [24] used a similar method to monitor weld defects and lack of penetration in submerged arc welding, which when combined with digital image analysis, provided information for adaptive feedback control. Fujinaga et. al [25] and Katayama, et. al [26] used in-situ radiography to observe keyhole behavior and weld defects in laser welding. Most recently Yamada et.al [27] developed a method for real-time in-process radiography for laser welding and Boateng et.al [28] used real-time radiography to reconstruct three dimensional crack growth data from gas tungsten arc welding.

Recently, Hojjatzadeh, et. al [29], observed pore dynamics, movement, and driving forces of pore motion and elimination using in-situ high-speed radiography on AlSi10Mg in laser powder bed fusion. This particular study observed a range of pore diameters of 10 μ m to 60 μ m. Hojjatzadeh, et. al combined in-situ experiments and physics modeling of pores in laser powder bed fusion experiments where they found a mechanism for effectively eliminating pores in 3D printing of metals [29]. Their physics model included the three primary forces acting on a pore: buoyant force (F_b), drag force (F_d), and Marangoni force (F_t). The competition of these 3 forces dictated the pore motion in different regions of the weld pool. After studying the different regions of the weld pool and the size of the pores disbursed in each region, it was found that the main driving force for pore elimination was the thermocapillary Marangoni force.

The in-situ study presented in this thesis is unique in that it examines porosity caused by controlled additions of hydrogen. The thin section coupons used here (3 mm thick) allows for better resolution of pores. Although, narrow weld pools also have a down side in that they do not necessarily represent what happens in wide, 3-dimensional weld pools. Micro-pores could not be resolved, thus what happens to interdendritic porosity will not be discussed. For larger pores, their behavior in the weld pool has been documented and quantified here, thus ending the need for speculation.

Chapter 3. Experimental

Autogenous, automatic, gas-tungsten arc welds were made along the edge of single 3 mm thick specimens (76 mm tall x 127 mm long) cut from 3 mm rolled plate. Welds were made in the direction of rolling. Weld preparation consisted of abrading the weld edge with a scouring pad and wire brush followed by acetone cleaning to remove abraded oxidation and any residual oil. Three different aluminum alloys were examined (Alloys 1100-H14, 4047-F, and 6061-T6) representing a broad spectrum of weldability and anticipated pool behavior. Chemical composition of these alloys can be seen in Table 2. Alloy 1100 H14 and 4047-F chemical composition reported in Table 2 was based on the manufacturer's certificate of chemical analysis. Alloy 6061-T6 manufacturer's certificate of chemical analysis was not found, therefore the reported values are per ASTM specification.

Table 2: Nominal Aluminum Alloy Chemical Composition

Alloy Type	Material Spec.	Weight Percent (Spec max) Actual							
		Si	Fe	Cu	Mn	Zn	Ti	Mg	Al
1100 H14	ASTM B209-14	(0.95)		(0.05-0.2)	(0.05)	(0.1)	(-)	(-)	(99.0)
		0.13	0.60	0.12	0.01	0.0	0.00	0.00	Bal.
4047-F	Similar to AWS A5.8	(11.0-13.0)	(0.8)	(0.30)	(0.15)	(0.20)	(-)	(0.10)	Bal.
		11.6	0.3	0.03	0.06	0.12	0.02	0.08	
6061-T6	ASTM B209-14	(0.4-0.8)	(0.7)	(0.15-0.40)	(0.15)	(0.25)	(0.15)	(0.8-1.2)	Bal.

Alloy 1100 is unalloyed (99 wt.% commercial purity) and has a high melting point and narrow solidification range (657-643°C) [30]. Alloy 4047 contains nominally 11-13 wt.% silicon. It is a near eutectic composition useful for brazing, and can be characterized as having exceptional pool fluidity, low melting point and a narrow solidification range (582-577°C) [30] [31]. Alloy 6061 is a heat treatable grade, alloyed with magnesium (0.8-1.2 wt.%) and silicon (0.4-0.8 wt.%). This alloy has a large solidification range (652-582°C) and tends to form a thick pool oxide, contributing to its pool sluggishness [30].

An alternating current (AC) power supply was chosen because of its controllable heat input and cleaning action. In AC welding, the electrode-positive (EP) portion of the cycle provides a stream of positive ions that bombard the part surface and crack the oxide layer. The cracked oxide particles are removed in the arc plasma, proving the oxide cleaning action [15]. The 75% electrode-negative (EN)/25% EP balance control was selected to give the optimum welding result for this application. The ceriated tungsten electrode, diameter of 2.38 mm (3/32 in.), was ground to a point. During the electrode positive portion of the cycle, the electron flow to the electrode resulted in electrode heating and melting of the tip, forming a rounded end. This expected characteristic was apparent in the radiographs. During the electrode negative portion of the cycle, electron flow to the plate results in base metal melting.

Welding parameters are given in Table 3, where welding current was adjusted to maintain a nominal weld pool depth of approximately 3 mm (0.125 in.) for the various travel speeds, hydrogen contents, and alloys examined. Weld travel speed was varied in order to identify kinetic effects on pore growth. Alloy 1100 required higher current because of its higher thermal conductivity. Welds made with high hydrogen shielding gas required reduced current due to the higher thermal conductivity of hydrogen and hotter arc. Hydrogen addition to argon increases the voltage drop in the arc and increases the energy concentration [32]. An increase in speed required an increase in current to achieve the desired nominal weld pool size. A full set of parameters for each welded sample can be found in Appendix A. Sample Weld Parameters.

Table 3: Gas tungsten arc welding parameters

AC Balanced Square Wave	75% EN, 25% EP
Arc Current	50-80 amps (rms)
Arc Voltage	12 volts
Travel Speed	1.69, 2.54, 3.39 mm/s
Ceriated Tungsten Electrode	2.38 mm dia., 30° tip angle

Variable hydrogen content in the argon shielding gas mixture was achieved by mixing controlled amounts (i.e. flow rates) of 99.999% argon and pre-mixed 99.999% argon + 1000 parts per million (ppm) of hydrogen. The actual mixtures that were used are tabulated in Table 4 (0-1000 ppm hydrogen). The total hydrogen reported in Table 4 were calculated based on the known flow rates of the shielding gas. This selected span of hydrogen contamination was based upon preliminary work, using post-weld still radiography on 6061-T6 aluminum. These preliminary welds showed macro-pores

solidified in the weld at hydrogen levels of 167 ppm and 333 ppm. These preliminary welds can be seen in LA-UR-18-30419: Hydrogen Contamination and Porosity Formation in Aluminum Welds [33].

Table 4: Controlled shielding gas mixtures of Ar and Ar-0.1% H_2

Shielding Gas flow rate = 30 cfh		Total H_2 ppm
Ar (cfh)	Ar+0.1% H_2 (cfh)	
0	30	1000
5	25	833
10	20	667
15	15	500
20	10	333
25	5	167
30	0	0

The entire weld pool was imaged (transverse to welding direction) during welding using digital radiography. Figure 10 shows a basic sketch of the experimental set-up side view of the radiography chamber. The digital x-ray radiography equipment used in this study was a Hamamatsu 150 eV X-ray source, with the North Star™ X25 industrial x-ray inspection system, normally used for 3-dimensional topographic analysis, coupled with a PaxScan 2520DX digital x-ray flat panel detector. Frame rate and magnification were varied during initial development to achieve the optimum resolution. Two different radiographic operating parameters were selected for this experiment and can be seen in Table 5.

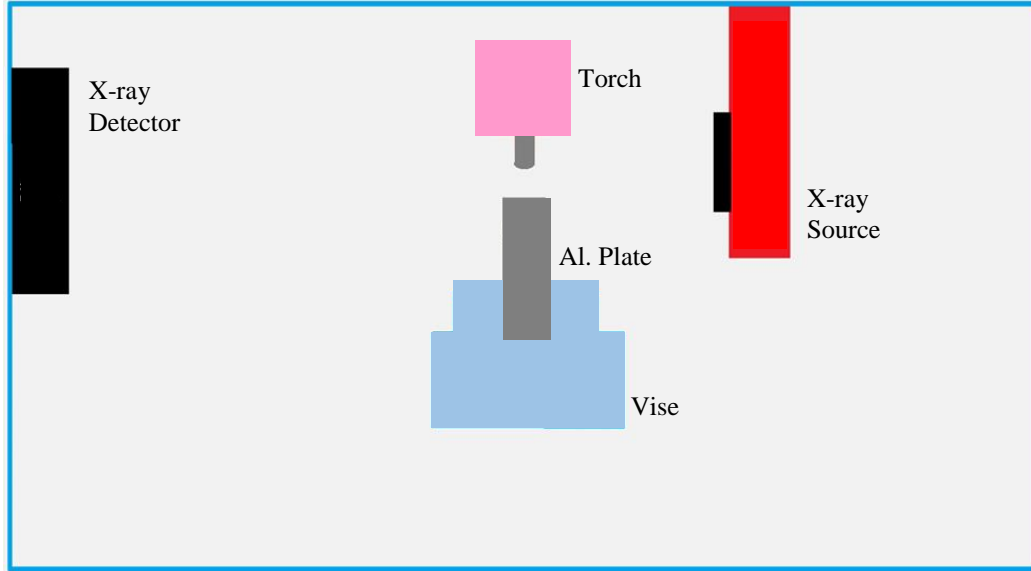


Figure 10: Side view of experimental set-up in radiography chamber.

Table 5: Operating parameters used for digital radiography.

Parameter	Set 1	Set 2
Energy (keV)	100	100
Current (μA)	100	100
Frame Rate (fps)	7.5	30
Source to Detector Distance (mm)	762	381
Source to Part Distance (mm)	76.2	38.1
Magnification	10X	10X
Binning	2	2
Effective Pixel Size (μm)	25.4	25.4

Figure 11 is a photograph of the experimental set-up inside the radiography chamber. The aluminum test specimen was secured in a vise on a moving slide table. The GTAW torch was mounted to a stationary arm, fixed to the floor of the experimental

chamber. The slide table traversed the aluminum plate underneath the stationary torch. The electrode to work piece distance was maintained at 2.38 mm (0.09375 in.) by leveling the welding edge of the aluminum plate in the vise. The x-ray source was positioned perpendicular to the plate to observe the weld pool during the welding process.

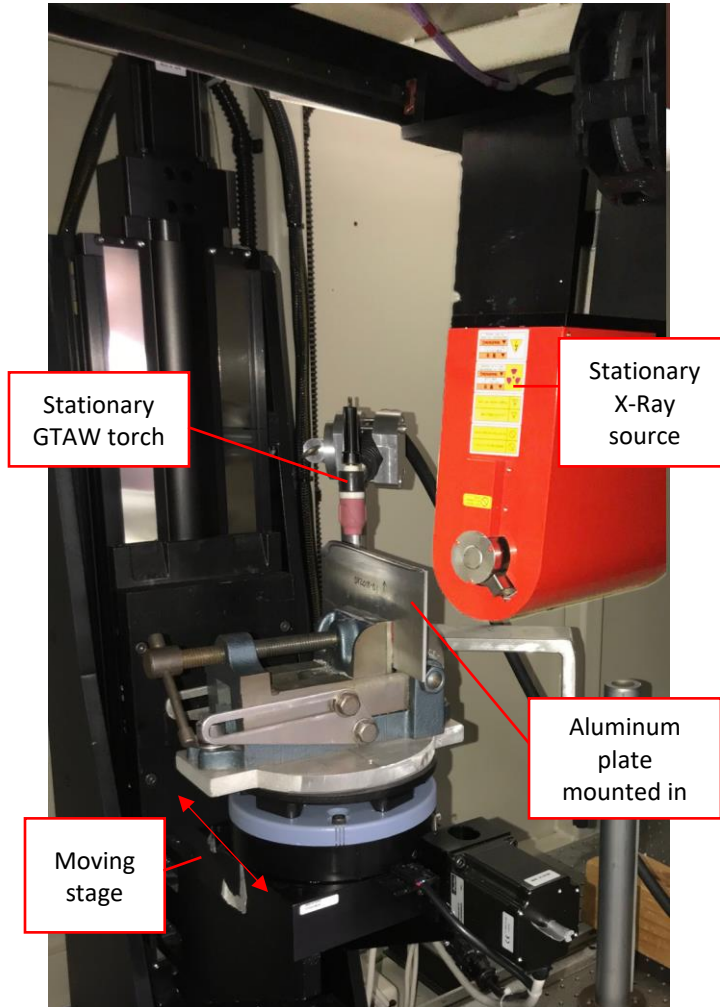


Figure 11: Photograph of experimental set-up showing moving aluminum plate specimen, GTA welding torch and stationary aligned x-ray source (red).

The welded aluminum specimens were analyzed using the in-situ radiography, gravimetric analysis, and metallography. In-situ radiography provided viewing of pore formation, pore growth rate, and pore movement. Afterwards weld metal was removed from the aluminum plate and sent for gravimetric analysis and metallography to determine the percent volume porosity and percent area porosity, respectively.

Figure 12 shows a drawing of the specimen map. Care was taken to minimize the possibility of outside hydrogen contamination during weld metal removal. A bandsaw was used to roughly cut the welded area from the plate, a significant distance from the weld metal to minimize contamination from the equipment. The weld metal was then trimmed with a hand operated shear cleaned with ethanol prior to use. Before the gravimetric, metallography, and Leco samples were taken, the first 19.05 mm (3/4 in.) of the weld was discarded due to the irregularities found in the weld start region.

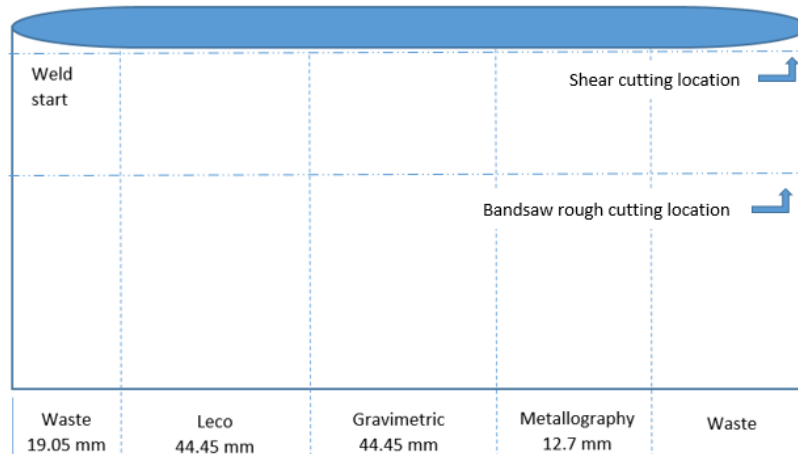


Figure 12: Side view of welded plate specimen indicating the approximate location and size of each sample.

Table 6 is a condensed version of the welded sample matrix, indicating there were 37 aluminum plate samples welded for this study. Not all samples had pores that could be tracked or measured during the in-situ radiography, but all samples were evaluated by gravimetric analysis and metallography. The results of each sample can be found in Appendix B.

Table 6: Condensed version of aluminum samples welded during this study.

Aluminum Alloy	Shielding Gas Hydrogen (ppm)	Travel Speed (mm/s)
1100	0	1.69
		3.39
	167	1.69
	333	1.69
		3.39
	500	1.69
	667	1.69
		2.54
		3.39
	833	1.69
	1000	3.39
4047	0	2.54
		3.39
	333	2.54
		3.39
	667	2.54
		3.39
	1000	2.54
		3.39
6061	0	1.69
		2.54
		3.39
	167	1.69
		2.54
	333	1.69
		2.54
		3.39
	500	1.69
		2.54
	667	1.69
		3.39
	833	1.69
	1000	3.39

In-situ Videos

The raw data from the in-situ radiographs were recorded. The radiographs, referenced from the point forward as a frame, were processed to enhance the contrast and then cropped to bring the area of interest to center view. The frames were stacked together to create a movie and Tiff stack. The Tiff stack, a time series of .tiff images under one filename, was opened in an image processing software, ImageJ, to take pixel measurements. One Tiff stack, representing one welded specimen, was analyzed at a time. The known electrode diameter measurement was taken using the image processing program, yielding the diameter measurement in pixels. Pores were tracked through frames and their diameters were measured using the image processing software. These pixel measurements were converted to millimeters using Equation 2. These pore measurements were used to compute average growth rate, Equation 3. The movies were also used to qualitatively observe pore formation and movement.

$$P_{\emptyset} = \frac{E_{\emptyset}}{E_P} * P_P \quad \text{Equation 2}$$

E_{\emptyset} = electrode diameter in millimeters

E_P = electrode diameter in pixels

P_{\emptyset} = measurement of feature in millimeters

P_P = measurement of feature in pixels

$$\Delta P = \text{average pore growth rate } \left(\frac{\text{mm}^2}{\text{s}} \right)$$

$$\Delta P = \frac{\sum \pi(r_2^2 - r_1^2) * \text{frame rate}}{\text{\#frames}} \quad \text{Equation 3}$$

r_1 = pore radius in frame 1 (mm)

r_2 = pore radius in frame 2 (mm)

frame rate = 30 or 7.5 frames per second(fps)

frames = number of frames with pore measurements

Gravimetric Testing

The gravimetric test was conducted to determine the percent volumetric porosity in the sample's weld metal. The test required the use of the following equipment: analytical balance, sample holder, immersion vessel (glass beaker), thermometer, and deionized water. A Mettler Toledo analytical balance and density kit [34] were used for this analysis. The test was conducted in a temperature controlled environment. The gravimetric sample specimens were approximately 44.45 mm (1.75 in.) long and were provided in the as-welded condition. Each sample specimen's surface was thoroughly cleaned with ethanol to remove any residual oils, grease, and dust. The glass beaker was then filled with deionized water and the thermometer was then mounted to the inside of the beaker. The beaker was then placed on the balance and sample holder was suspended mid-way into the beaker of water. The water was allowed to degas prior to performing measurements. Figure 13 shows the approximate set-up.

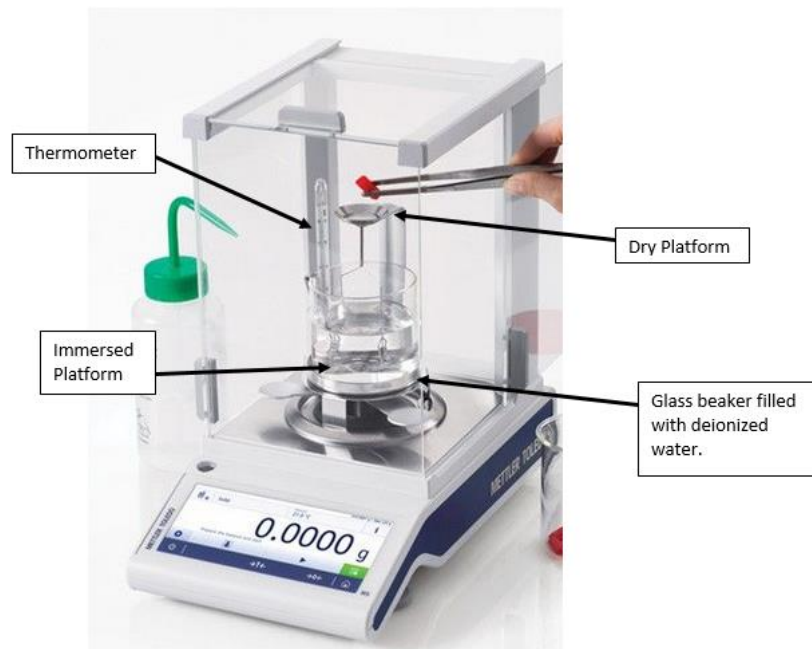


Figure 13: Density determination set-up with analytical balance and density kit [34].

Using the analytical balance, each specimen was weighed five times on the dry platform. The specimen was then placed on the sample platform immersed in water. The immersed mass measurement was recorded once the water was free of visible air bubbles. The water temperature was measured and recorded. Following the immersed measurement, the specimen was removed from the water and given a quick shake to remove excess water from the specimen. The wet specimen was then placed on the dry platform for a wet mass measurement. The immersed mass and wet mass were measured 5 times for each specimen.

The data taken was then used to calculate the percent porosity and percent open porosity. The specimen density, percent volumetric porosity, and percent surface porosity were calculated using Equation 4 through Equation 6.

$$\rho_m = \frac{mass}{volume} = \frac{m_d}{\left(\frac{m_d - m_i}{\rho_w}\right)} \quad \text{Equation 4}$$

$$\% \text{ Porosity} = \left(\frac{(\rho_T - \rho_m)}{\rho_T}\right) * 100 \quad \text{Equation 5}$$

$$\% \text{ Open Porosity} = \left(\frac{m_w - m_d}{m_i - m_w}\right) * 100 \quad \text{Equation 6}$$

where:

ρ_m = calculated density of specimen

m_d = mass of dry specimen (grams)

m_i = mass of specimen while immerse in water (grams)

m_w = mass of wet specimen on dry platform (grams)

ρ_T = theoretical density of specimen (alloy specific)

% Porosity = volumetric porosity in specimen

% Open Porosity = % of porosity that is open to the surface

Metallography

Metallographic samples were cut transverse to the weld and mounted in epoxy. Preparation of each sample required grinding with 240, 360, 400, 600, 800, and 1200 grit paper for approximately 1 minute each followed by an initial polish with 3 micron, 1 micron, and 0.25 micron diamond suspension paste for approximately 10 minutes each. A final polish using 0.25 micron colloidal silica paste was then conducted for 5 minutes.

The micrographs, taken at 25X, 50X, and 100X magnification, were then used to calculate percent area porosity. First the total sample area, A_T (pixels), was calculated in pixels. The area for each pore was then calculated and added together yielding a total area of porosity, A_p (pixels). Equation 7 represents the calculation for the percent area porosity.

$$\% \text{ Area Porosity} = \left(\frac{A_p}{A_T} \right) * 100 \quad \text{Equation 7}$$

Figure 14, alloy 4047 with 0 ppm of shielding gas hydrogen added, shows a typical weld metal cross-section. A micro-pore seen on the bottom left portion of the weld metal. It is observed that the fused area appears like a truncated circle, with a nominal diameter of 4.5 mm, only slightly larger than the plate thickness.

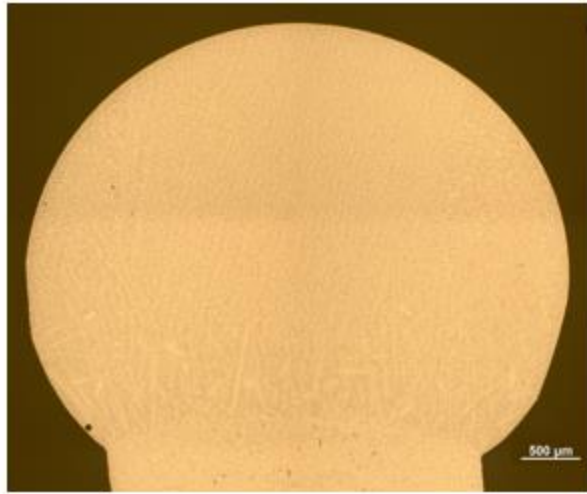


Figure 14: Typical weld cross-section showing bead shape of edge weld.

Chapter 4. Results

In-Situ Radiography Data

There were a total of 37 videos captured during welding of aluminum Alloys 1100, 4047, and 6061. Presented in this section are figures showing selected in-situ data through a series of frames, the welding direction is from right to left. In the top left corner of each image is a number indicating the frame number. Each frame shows an approximate outline of the weld pool for orientation purposes. In some frames, a macro-pore is outlined to indicate the pore that is being tracked and measured for the weld. Although all the videos were informative on some level, not all videos had traceable macro pores.

Due to the inability to resolve micro-pores in this study ($<10\text{ }\mu\text{m}$), the topic of interdendritic pore nucleation cannot be assessed. It can only be stated that pores appear to originate either at the pool bottom (Alloys 1100 and 4047) or pool front (Alloy 6061), irrespective of whatever is happening interdendritically from hydrogen partitioning. This gives support for Woods' [13] hypothesis that pores nucleate within the weld pool due to the rapid cooling of supercharged liquid moving from the pool surface (under the torch) to the pool periphery [13]. The pore nucleation size is unknown, although they are assumed to be micron size. When pores are first observed in this study, they are approximately $90\text{ }\mu\text{m}$ in diameter.

Pore Formation and Migration

Figure 15 shows an Alloy 1100 sample, welded with 500 ppm shielding gas hydrogen at a travel speed of 1.69 mm/s. The tracked pore is first observed in frame 47 as a micro-pore at the bottom edge of the weld pool, trailing the electrode. It is within 0.133 seconds, the time between frames that the pore transforms into a measureable macro-pore. The trailing edge of the pore seems to be pinned in the solidified region causing the pore to grow in an elliptical shape. As the top half of the pore continues to accumulate hydrogen, the shape becomes spherical yielding a light bulb shaped pore. The rapid pore growth ends in frame 53, when the pore gas escapes at the surface which can be seen as a halo over the weld pool. In frame 54, the void left behind from the pore was quickly back filled with molten metal, leaving behind a small cavity that had already been overcome by the solidification front. The final pore size, as seen in frame 53, had a maximum diameter of approximately 2.045 mm and was approximately 2.688 mm in length. Due to the irregular growth, the average growth rate was not calculated. The time for this pore to grow and gas escape was approximately 0.93 seconds.

It can also be seen throughout this set of frames that not every macro-pore breached the surface. The macro-pores to the right of the previously mentioned macro-pore have been completely engulfed by the solidified weld metal.

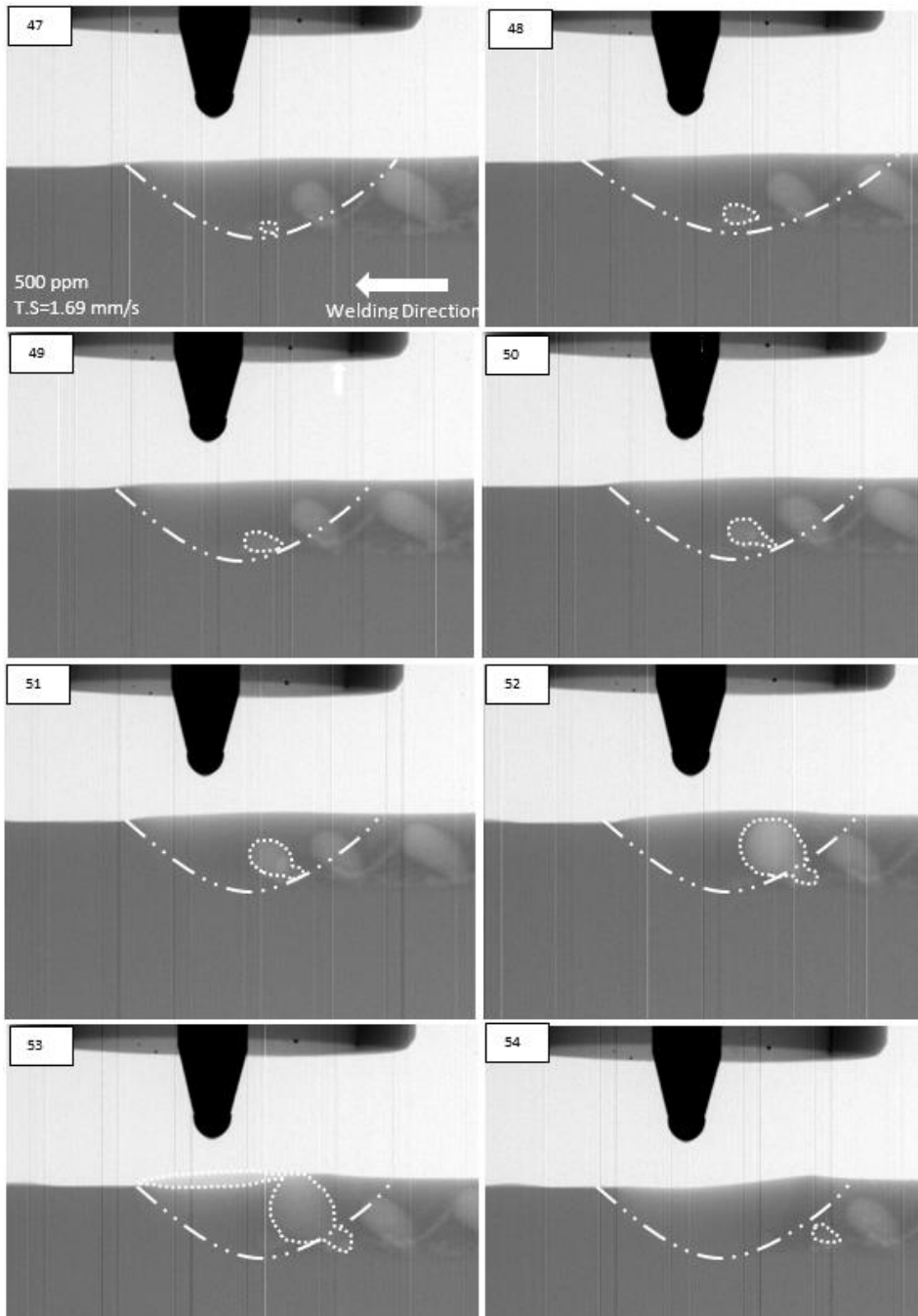


Figure 15: Alloy 1100 welded using 500 ppm shielding gas hydrogen at a travel speed of 1.69 mm/s, shows pore formation at the bottom of the weld pool and pore gas escape.

Figure 16 is an Alloy 1100 sample welded with 333 ppm shielding gas hydrogen at a travel speed of 1.69 mm/s. Figure 16 follows a macro-pore through pore growth until it eventually becomes partially engulfed by the solidification front. The macro-pore, through this set of frames, exhibits similar formation and growth as described in Figure 15. In Frame 107, the macro-pore has grown so large that it reaches the weld pool surface. In Frame 108, approximately a quarter of the macro-pore had backfilled with molten metal. This indicated the majority of the pore had already become entrapped by the solidified region by the time the pore had reached the weld pool surface and that partial pore engulfment contributes to the pore shape.

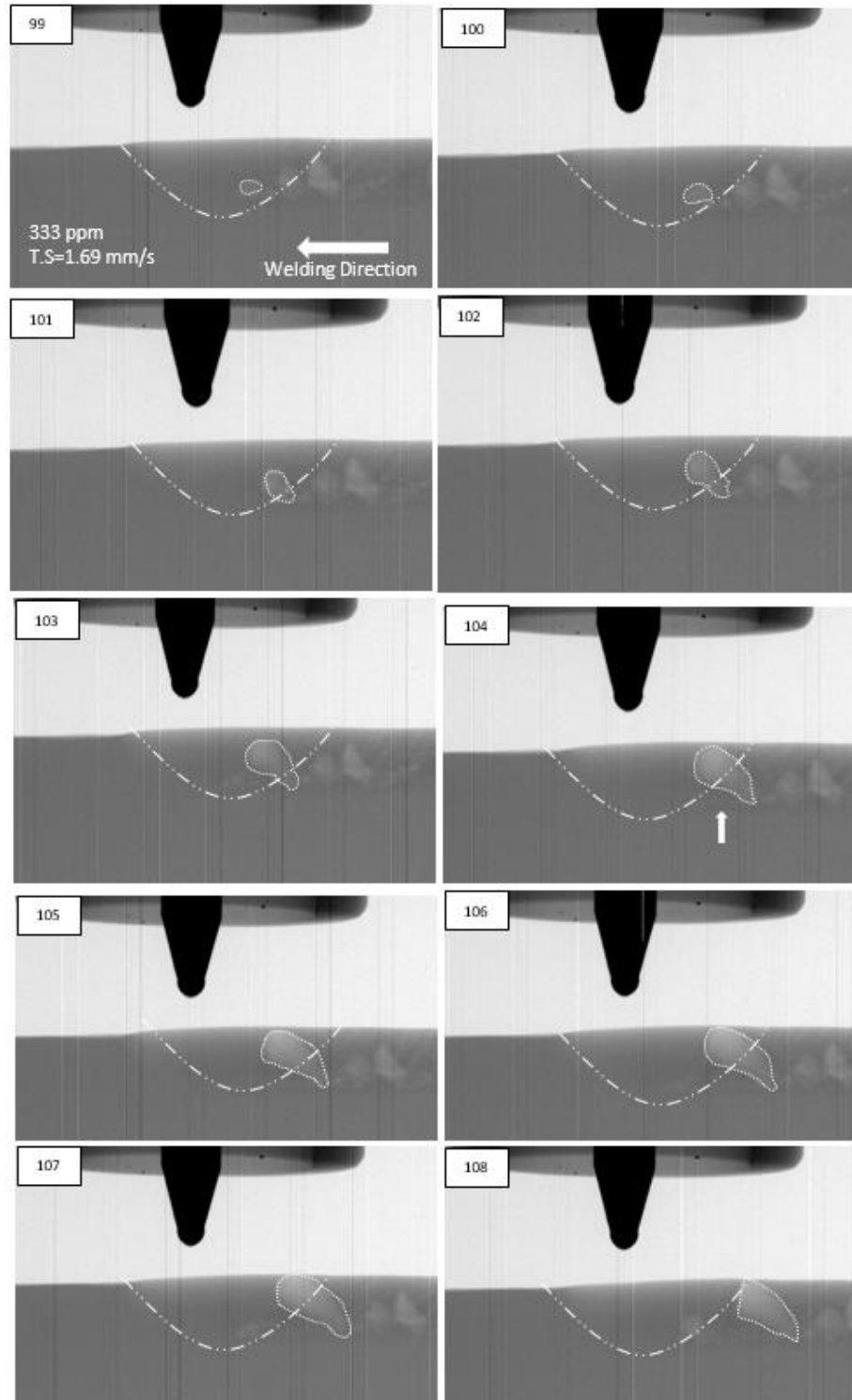


Figure 16: Alloy 1100 welded sample using 333 ppm shielding gas hydrogen at travel speed of 1.69 mm/s, shows pore formation at the bottom of the weld pool and elongated pore growth.

In Alloy 1100, macro-pores were observed to form at the bottom of the weld pool and behind the centerline of the electrode. The macro-pores do not free float in the weld pool or enter the bulk of the weld pool. The macro-pores appeared to be pinned down at the root of the weld with little to no migration in the weld pool. The pores, through hydrogen gas coalescence and diffusion, grew in an elliptical shape as the weld progressed. General observation of Alloy 1100 showed single pores growing rapidly, expanding in diameter upward, eventually either escaping or becoming entrapped as an elongated, elliptical pore.

Figure 17 shows one representative frame from an Alloy 4047 sample welded with 667 ppm of hydrogen in the shielding gas at a travel speed of 2.54 mm/s. Micro-pores were observed on the weld pool surface, seen above the dashed line in Figure 17. No macro-pores were resolvable within the weld pool. However, there were clear indications of micro-pores clustered at the leading and trailing edge of the weld pool surface. This behavior was observed throughout the Alloy 4047 welded samples beginning at shielding gas hydrogen levels of 333 ppm and greater. In Figure 17, the entrapped micro-pores can be seen near the top edge of the weld. During the experiments with slower travel speed, 2.54 mm/s, the areas micro-porosity showed up as brighter clusters on the images, indicating a more densely populated area with micro-pores.

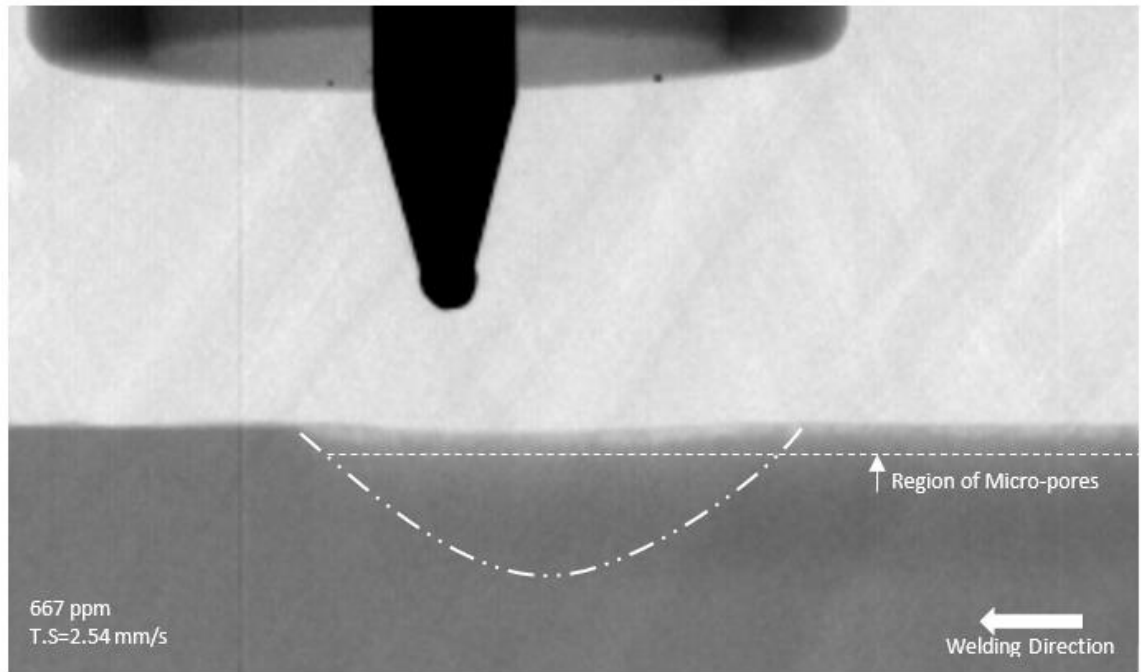


Figure 17: Alloy 4047 welded samples using 667 ppm shielding gas hydrogen at travel speed of 2.54 mm/s, shows micro-porosity at the leading and trailing edge of the weld pool.

Figure 18 shows an Alloy 4047 sample welded with 1000 ppm of hydrogen in the shielding gas at travel speed of 2.54 mm/s. This set of frames captured the only macro-pore observed in the Alloy 4047 welded samples. It appeared at weld start thus it was discarded from measuring and recording pore growth rate. It was thought this region did not represent the nominal weld due to irregularities or instabilities experienced during weld start. However, it gives insight into the potential macro-pore shape and behavior in Alloy 4047. The macro-pore, shown in Frame 66, formed at the leading edge of the weld pool and remained in the shape of a sphere during its growth period. The macro-pore stayed in the top of the weld pool until it was swept downward and back, towards the

trailing of the weld pool. The macro-pore then floated upwards toward the surface of the weld pool where it eventually breached the surface losing the trapped gas. The final pore size, as seen in Frame 83, had a diameter 1.483 mm.

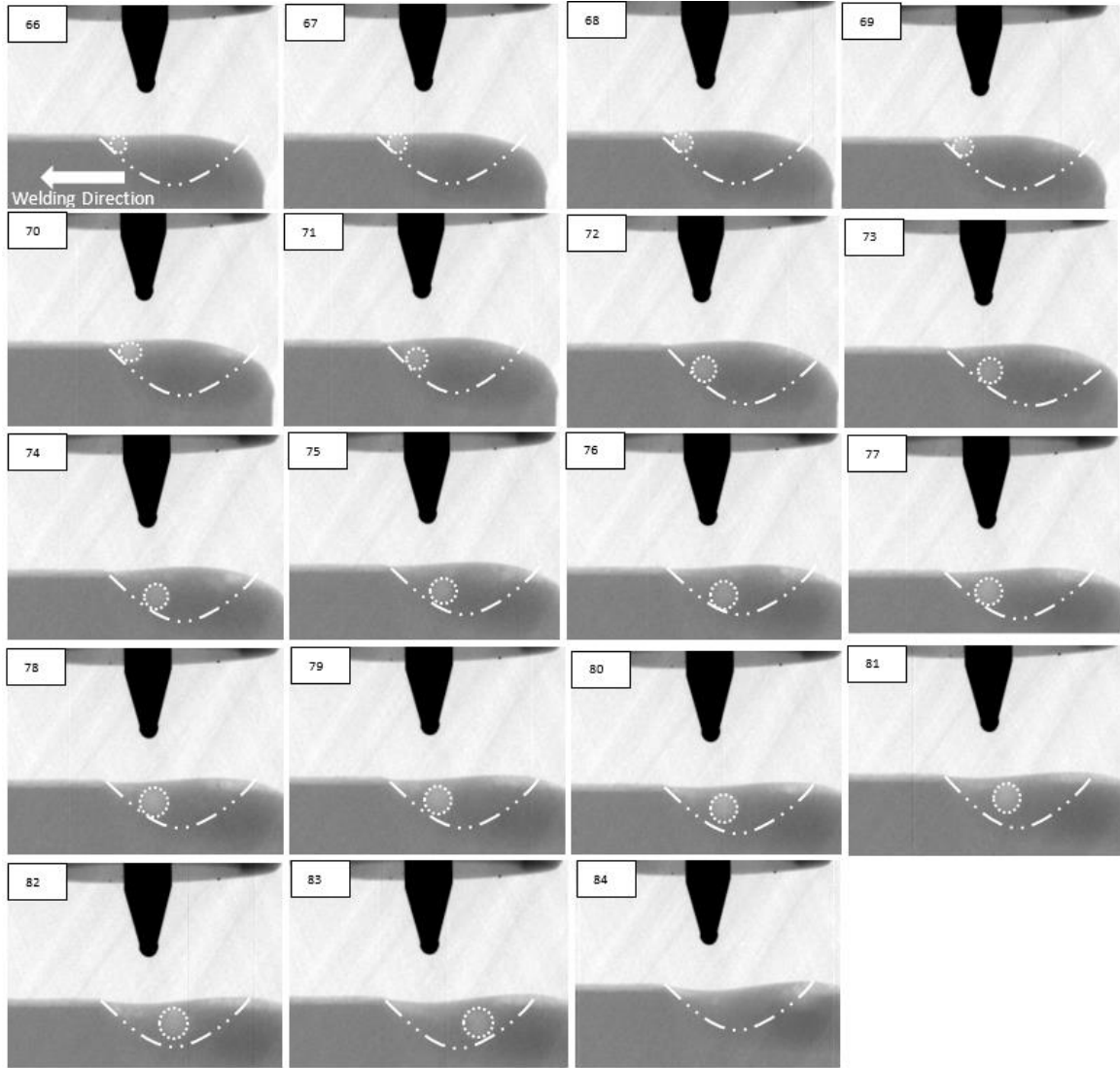


Figure 18: Alloy 4047 welded sample using 1000 ppm shielding gas hydrogen at travel speed of 2.54 mm/s, shows pore movement.

Figure 19 shows an Alloy 6061 sample, welded with 667 ppm shielding gas hydrogen at a travel speed of 1.69 mm/s. Frame 118 presents a macro-pore which has formed at the leading edge of the weld pool. The macro-pore is spherical in shape. Within a few milliseconds, the macro-pore was pushed to the bottom of the weld pool and swept quickly to the trailing edge of the weld pool. At the bottom of the solidified weld metal, a stream of micro-pores is observed. It is unclear at which point these micro-pores have formed, or their migratory pattern. In the final frame where the pore is observed, frame 125, the pore had breached the weld pool surface and the pore gas is seen escaping and covering the weld pool surface. The final pore size, as seen in frame 124, had a diameter 1.82 mm with an average growth rate of $3.14 \text{ mm}^2/\text{s}$ as calculated from cross-sectional area of the pore. The time for this pore to grow was approximately 1.06 seconds.

Figure 19, Frame 121 captured the motion blur of the macro-pore traveling in the weld pool at a faster velocity than the frame rate. From this occurrence, the macro-pore may have entered into a region of high velocity during its migration to the trailing edge of the weld pool. There were many instances when this type of feature was captured during Alloy 6061 in-situ observation.

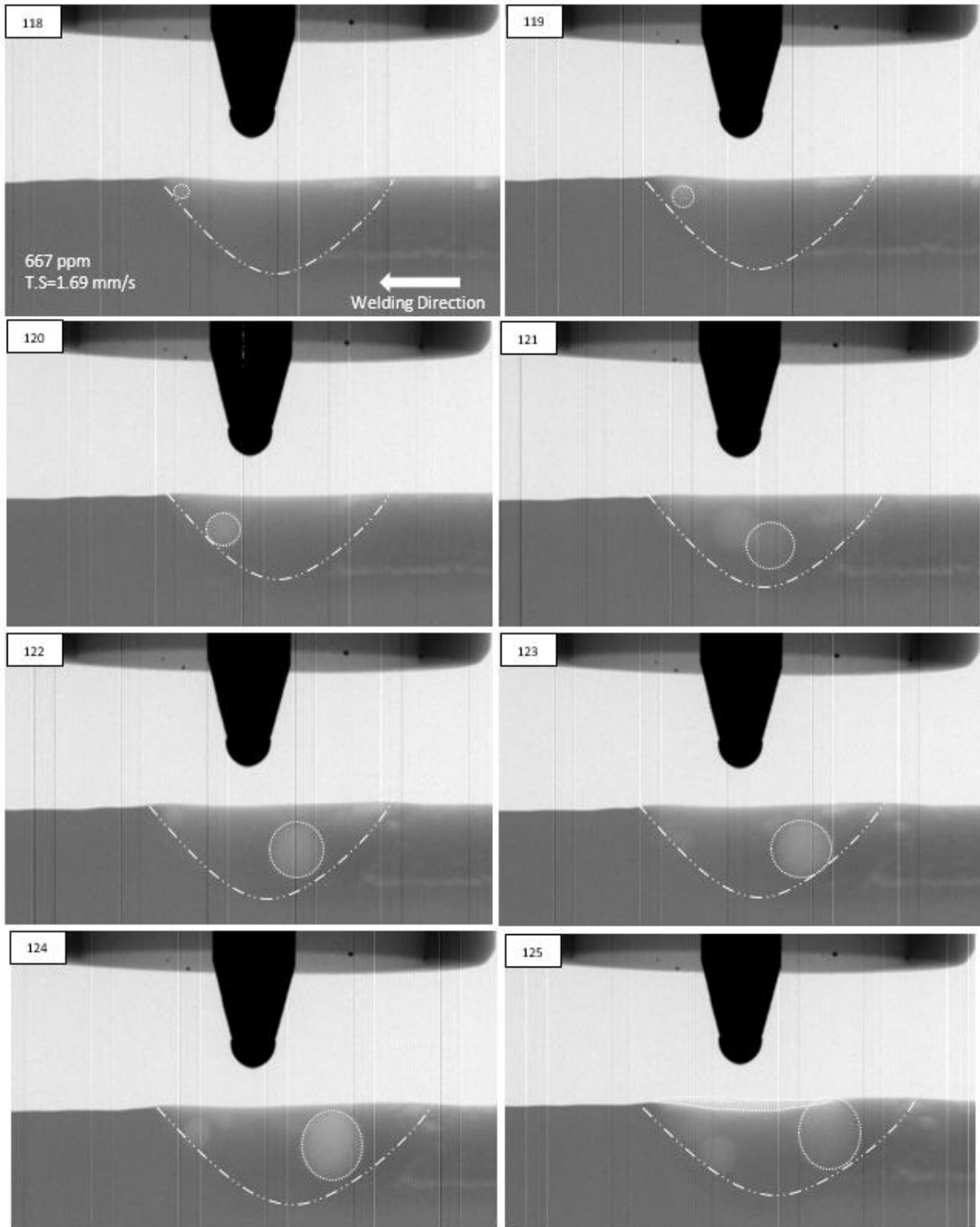


Figure 19: Alloy 6061 welded sample using 667 ppm shielding gas hydrogen at a travel speed of 1.69 mm/s, shows pore escaping in the final frame and a steady stream of micro-pores solidified in the weld metal.

Although the growth of the pores can be attributed to the diffusion of hydrogen, the coalescence of macro-pores can also be observed. Figure 20 shows two macro-pores at the leading edge of the weld pool join together to form one larger macro-pore. Another instance of coalescence can be seen in Figure 21. Over three frames, the macro-pore located at the leading edge of the weld pool, moves up and down in the weld pool collecting the micro-pores floating near the surface of the weld pool.

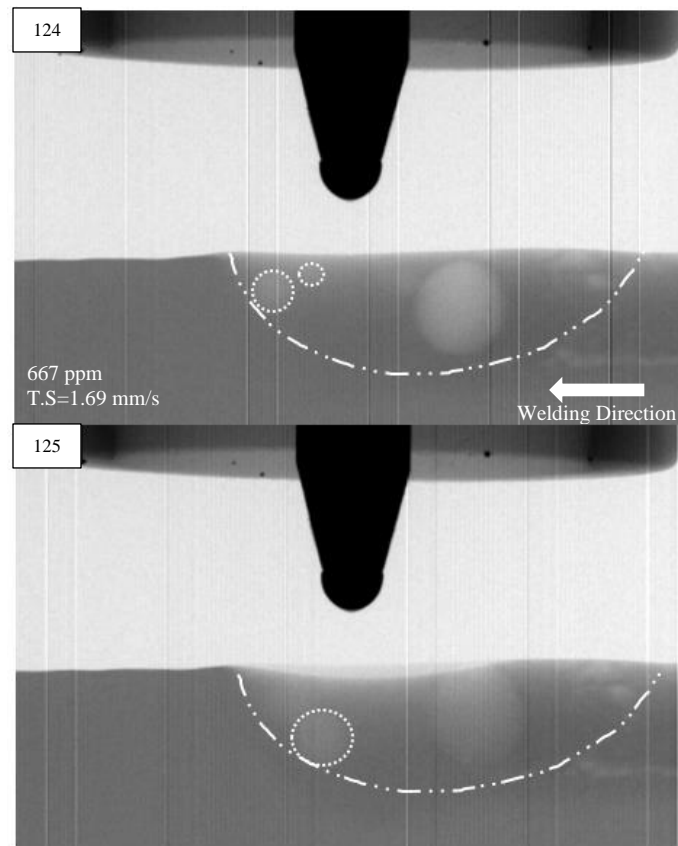


Figure 20: Alloy 6061 welded sample using 667 ppm shielding gas hydrogen at a travel speed of 1.69 mm/s, shows the coalescence of two pores in the weld pool.

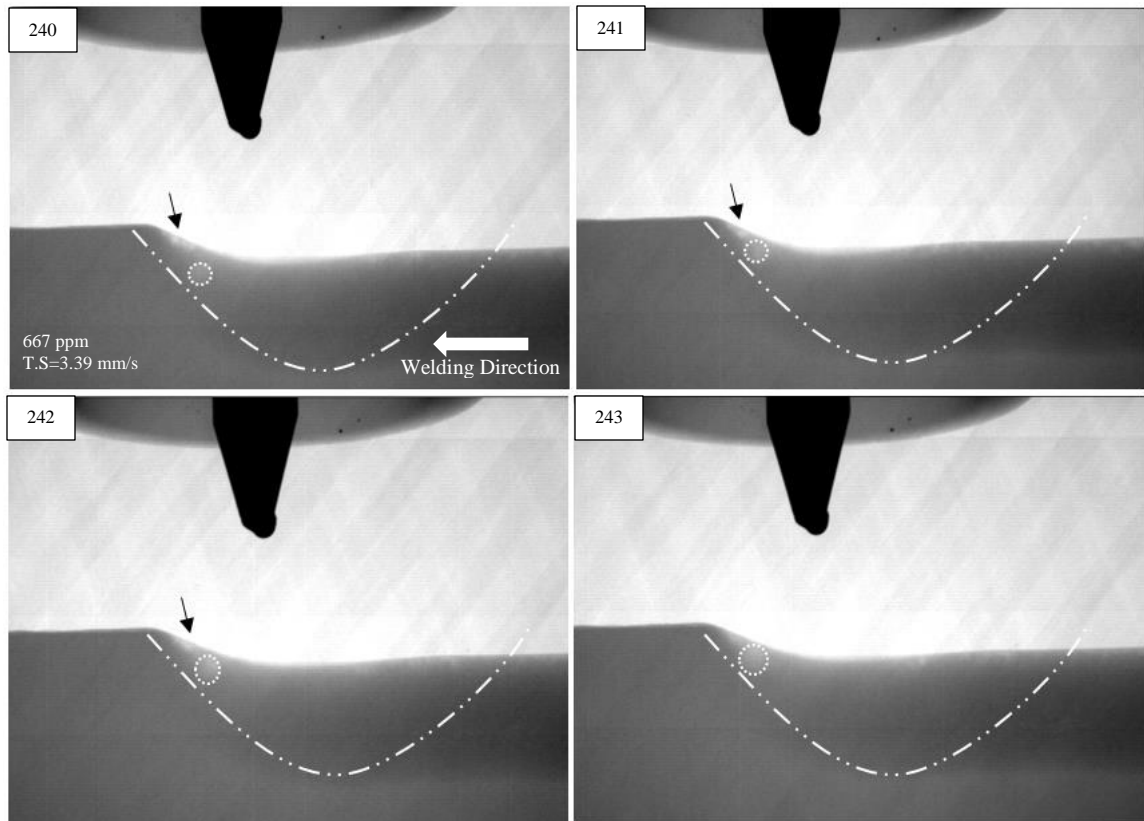


Figure 21: Alloy 6061 welded sample using 667 ppm shielding gas hydrogen at a travel speed of 3.39 mm/s, shows macro-pore growth via hydrogen coalescence from micro-pores, shown underneath the black arrow, near the macro-pore.

Figure 22 is another example of an Alloy 6061 sample welded with 833 ppm shielding gas hydrogen at a travel speed of 1.69 mm/s. The macro-pore formation and movement observed was the same as seen in Figure 19. At these higher levels of hydrogen, Alloy 6061 macro-pores were observed both at the leading and trailing edge of the weld pool. This behavior can be seen when looking at Frame 64 and Frame 65. In Frame 64, a cluster of micro-pores is seen just below the surface at the trailing edge of the weld pool, shown just above the long arrow. In Frame 65, this cluster of micro-pores combines to make a few macro-pores; macro-pores observed to be a more clearly defined

shape and measurable. This combination occurs rapidly, within the 0.133 seconds between frames.

It can be noted that the macro-pore outlined in frame 67, almost instantaneously, breached the surface, the trapped gas quickly escaped, and the pore void quickly backfilled with molten metal. These actions occurred between Frame 67 and 68. The final pore size, as seen in frame 67, had a diameter of 1.628 mm with an average growth rate of $2.910 \text{ mm}^2/\text{s}$ as calculated from the cross-sectional area of the pore. The time for this pore to grow was approximately 0.80 seconds.

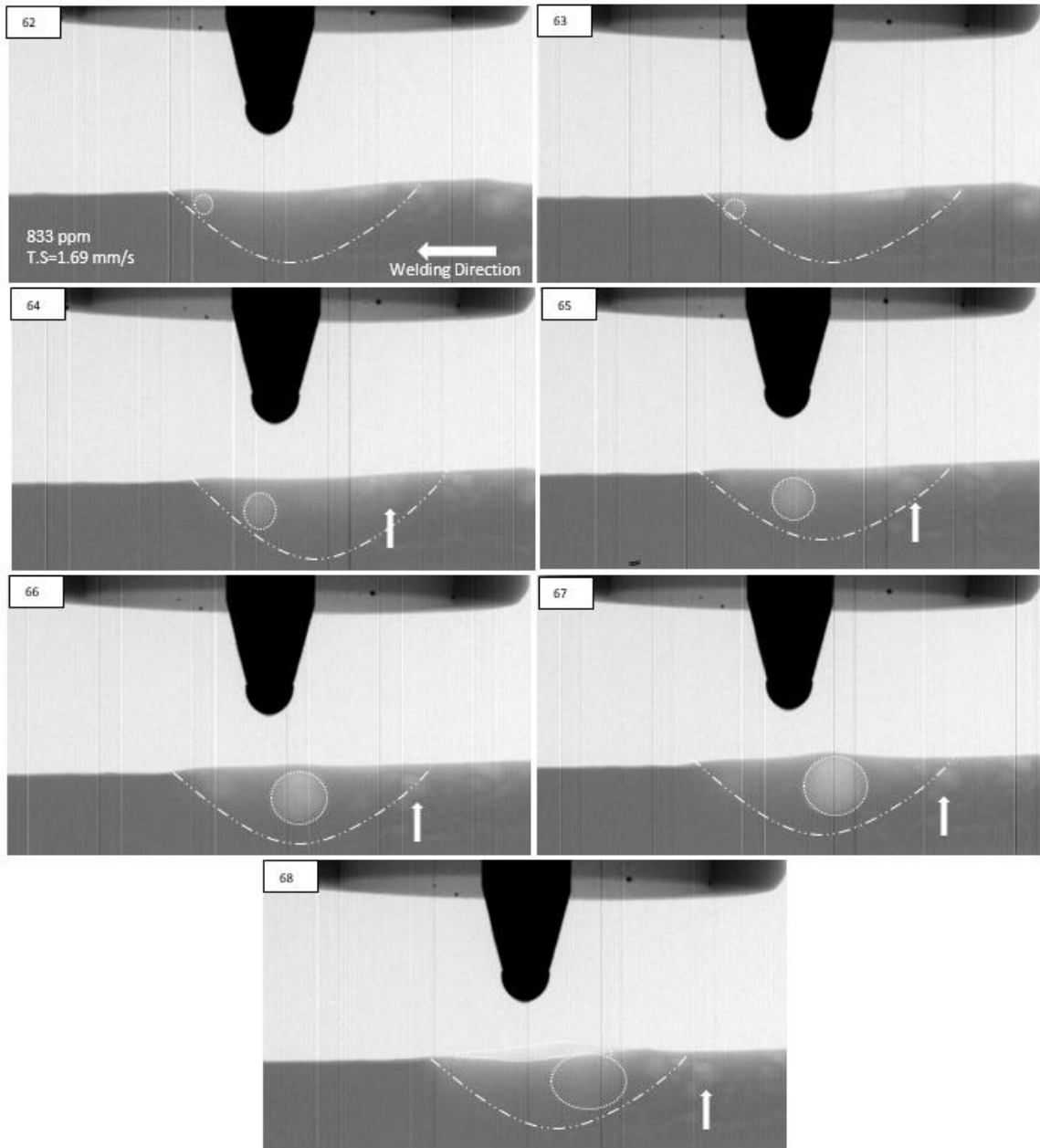


Figure 22: Alloy 6061 welded sample using 833 ppm shielding gas hydrogen at a travel speed of 1.69 mm/s, shows micro-pores formed at the trailing edge of the weld pool pointed out above the white arrow.

In Alloy 6061, the majority of macro-pores were observed to form at the leading edge of the weld pool just below the surface. General observation of Alloy 6061 showed

spherical pore growth and periodic engulfment throughout the varying levels of hydrogen. Micro-porosity was present throughout the weld regardless of the amount of shielding gas hydrogen. The presence of macro-porosity and micro-porosity increased as the amount of shielding gas hydrogen increased. Due to the selected frame rate, it was difficult to observe the movement of micro-pores. This was one limitation of the radiographic technique, which will be discussed in more detail later.

The micrographs from each Alloy with porosity agreed with the observations from the in-situ data. Figure 23(a) shows Alloy 1100 welded with 500 ppm of shielding gas hydrogen at a travel speed of 1.69 mm/s. The macro-pores are located at the bottom of the weld with an elliptical shape along with micro-pores throughout the cross-section. Figure 23(b) shows Alloy 4047 welded with 1000 ppm of shielding gas hydrogen at 2.54 mm/s. There are micro-pores throughout the cross-section, with what seems to be an area of clustering near the crown of the weld. Figure 23(c) shows Alloy 6061 welded with 333 ppm of shielding gas hydrogen at a travel speed of 2.54 mm/s. This weld cross-section contains a mixture of macro and micro-pores with the larger macro-pores near the crown of the weld. All the pores in Alloy 1100, 4047, and 6061 cross-sections were entrapped at the trailing edge of the pool.

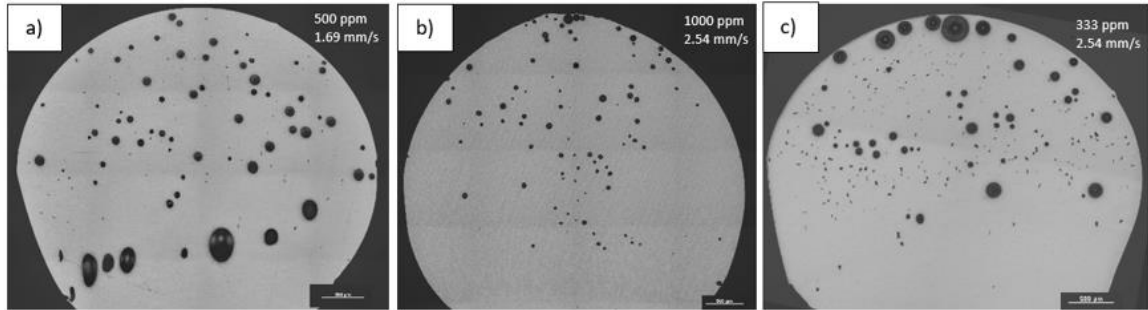


Figure 23: Micrographs showing pore shape in a) Alloy 1100, b) Alloy 4047, and c) Alloy 6061.

In the case of Alloy 1100, it can be argued that superheated and supercharged aluminum at the pool surface moves rapidly to the pool bottom, aligned directly below the torch, where the liquid is rapidly cooled and pores are nucleated. This location is also where the macro-pores began to form in Alloy 1100, as reported in the in-situ data. This suggests a fluid flow pattern as described in Figure 24(a). Likewise the pores are then moved upward by this flow cell, in addition to buoyancy. In the case of Alloy 6061 and Alloy 4047, superheated and supercharged aluminum flows outward where it is cooled at the front of the pool and pores are nucleated. This is the location where the majority of macro-pores began to form for Alloy 6061 as reported in the in-situ data. Pores are then forced downward by an interaction with flow cell as suggested in Figure 24(b). Once collected at the bottom, they become influenced by upward buoyancy and liquid flow.

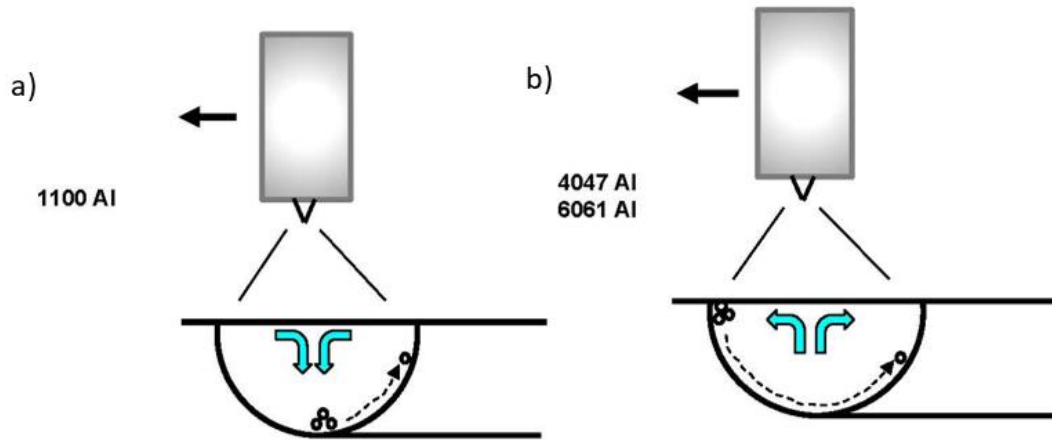


Figure 24: Schematic demonstrating different fluid flow patterns and macro-pore formation in aluminum Alloy welds a) 1100 versus b) 6061 and 4047

It is of particular interest to note that pores were not observed to move within the bulk of the weld pool, but only along its outer boundaries. This behavior was predicted earlier in the background section and was tied to an incompatibility between the rapid fluid flow and the pores. Nevertheless, it follows that the movement of a pore along the pool boundary may still be influenced by internal fluid flow patterns, i.e. flowing past it and pushing it along the boundary zone. Hence, the difference in macro-pore migration behavior between Alloys 1100, 4047, and 6061 may be related to differences in flow patterns, likely associated with Marangoni (surface tension driven) flow.

Unlike for stainless steel, there has been only a limited number of studies modeling flow patterns within aluminum weld pools. Since our welds were made at relatively low current (< 80 amps, rms), it is possible that flow could be affected by Marangoni surface tension. Kou, et al. [35] demonstrated in predictions for flow in a Al 6061 weld, assuming a current of 150 amps and a negative surface tension temperature coefficient ($dy/dT = -0.35 \text{ mN/m}^\circ\text{C}$), that surface tension overpowers electromagnetic and

buoyancy forces resulting in outward flow at the surface. This would be analogous to welding a low sulfur stainless steel. This is what could be happening with the Alloy 6061 and 4047 welds.

For the case of 1100 aluminum, the surface tension temperature coefficient for commercial pure aluminum has been measured in argon to be $-0.15 \text{ mN/m}^\circ\text{C}$ [36]. This is less than half the $-0.35 \text{ mN/m}^\circ\text{C}$ value used by Kou for Al 6061. This lower $d\gamma/dT$ slope may explain the reversed flow observed in this study, where the weaker outward contribution from Marangoni flow becomes overpowered by the inward electromagnetic driven flow. Hypothetical calculations by Kou and Wang [37] have demonstrated that smaller or positive values of surface tension temperature coefficient can reverse flow direction from outward to inward at the surface. In this same paper, the authors postulated that outward flow at the surface would interfere with pore escape, resulting in more pores becoming entrapped. Although this study did not analyze this effect directly, this could be why the macro-pores that formed near the surface of the leading edge of the weld pool were able to grow in Alloy 6061.

Recent sessile drop experiments on high purity aluminum and aluminum alloys showed that surface tension values are strongly affected by alloying and the nature of surface oxide formed on the drops [38]. It is reasonable to assume that oxygen is a surface-active element, but how it reacts with alloying elements is also clearly important. Magnesium in particular was found to lower surface tension even when present in small amounts. Likewise, how alloying elements affect the surface tension temperature coefficient is not well understood or documented for aluminum and deserves attention.

Pore Growth

Measurements of the amount of hydrogen retained in the weld metal were not made, however, the in-situ data showed that macro-pores appeared only when enough hydrogen was introduced to the weld pool considering the combination of travel speed and associated welding parameters. Therefore not every welded sample contained measureable macro-pores. Although there was varied amounts of micro-porosity present in the weld samples, not every micro-pore contributed to macro-pore growth. Due to the complex shape of the Alloy 1100 pore and the lack of macro-pores in Alloy 4047, no pore growth measurements were taken for these alloys. Alloy 6061 macro-pores, as mentioned above, were circular and easier to track through the frames. Pore growth measurements reported in the following sub-section were based on one pore from each weld. Limited data was available for each parameter set and, in some cases, only one pore was present in the weld. This limitation can be overcome in future studies by duplicating welds with the same parameter sets and measuring more than one pore per weld to get an average.

Figure 25 shows that when the amount of shielding gas hydrogen was held constant and travel speed was varied, the travel speed had a direct effect on macro-pore growth rate in Alloy 6061. Although the fast speed is actually where most gas tungsten arc welding is performed, the pores observed at slow speed give great insight into what is happening in the weld pool with respect to pore migration and pore growth.

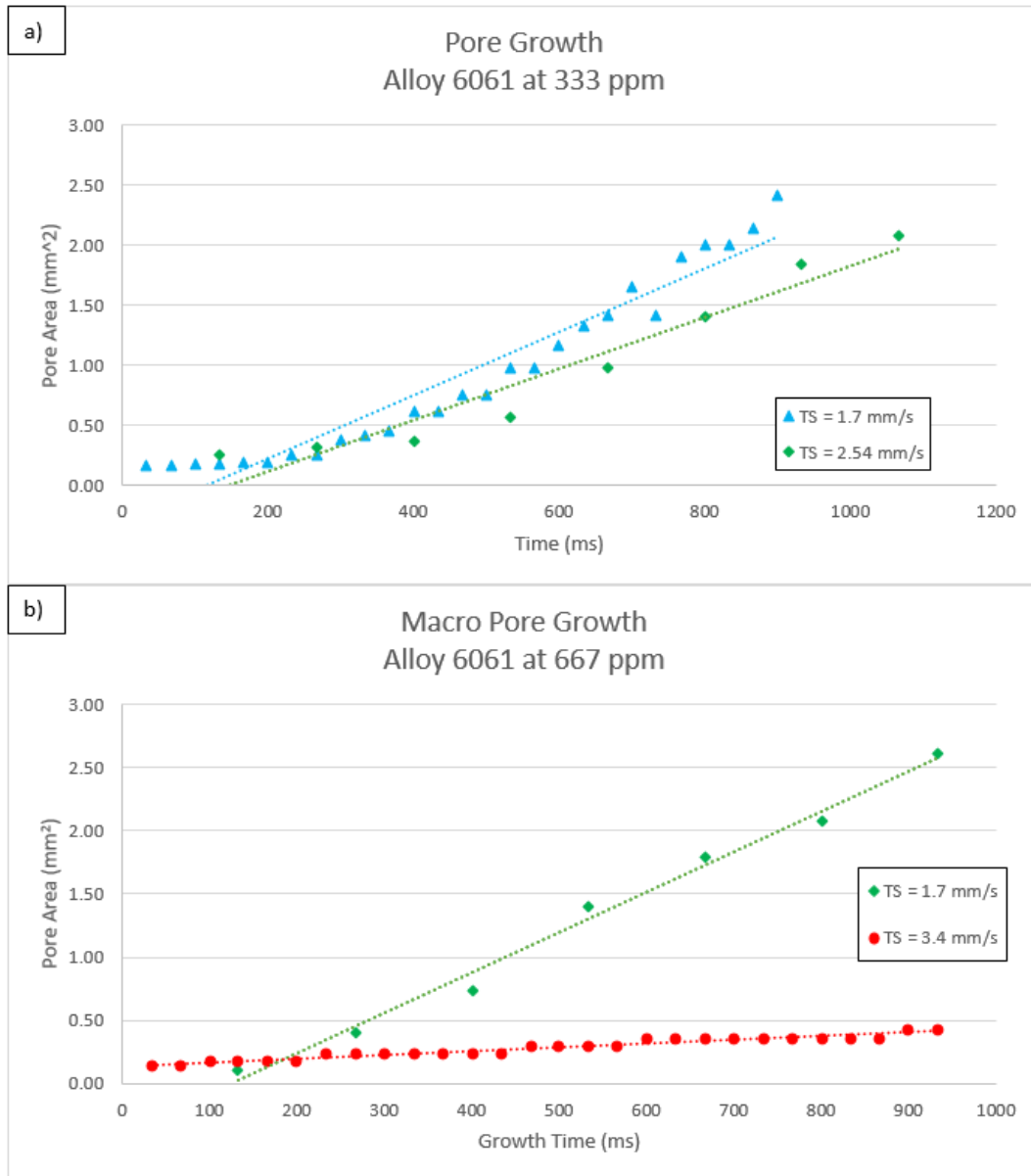


Figure 25: The effect of travel speed can be seen with in-situ data pore measurements when comparing the macro- pore area (mm²) observed during the different travel speeds at a) 333 ppm of shielding gas hydrogen and b) 667 ppm of shielding gas hydrogen.

Figure 26 shows the growth of three pores measured from the in-situ data, welded with a travel speed of 2.5 mm/s using different amounts of hydrogen in the shielding gas.

When the travel speed was kept constant and the amount of hydrogen in the shielding gas was varied, Alloy 6061 showed an increase in growth rate.

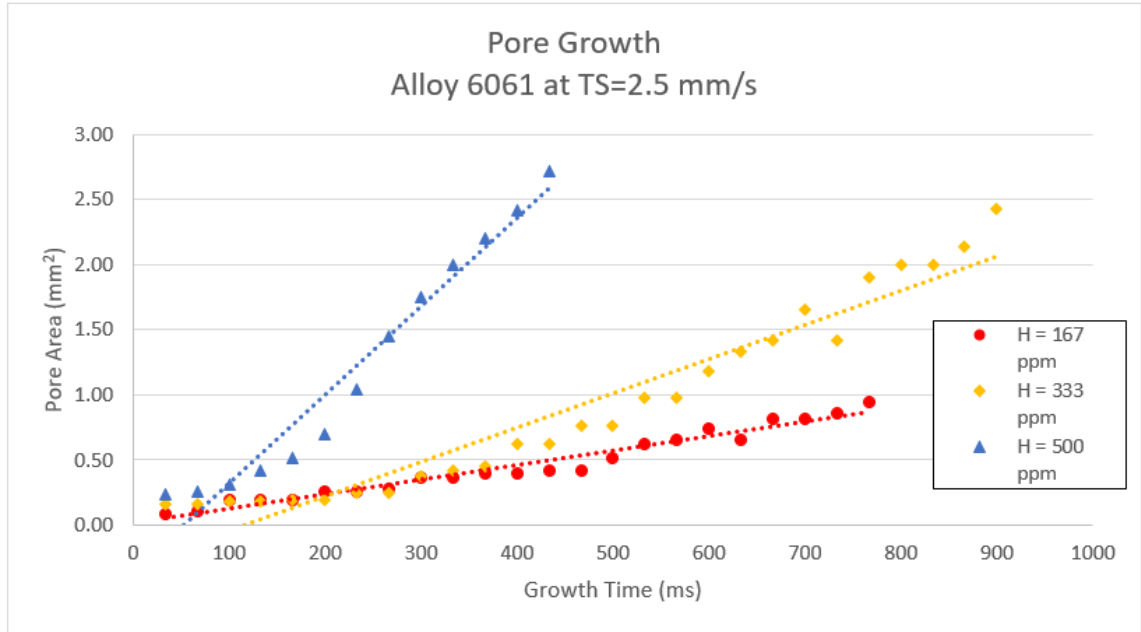


Figure 26: The effect of shielding gas hydrogen can be seen with in-situ data pore measurements when comparing the macro- pore area (mm²) observed during the amounts of shielding gas hydrogen at a travel speed of 2.5 mm/s.

Table 7: Alloy 6061 tabulation of final pore diameter and average growth rate based on in-situ data.

Hydrogen (ppm)	Travel Speed (mm/s)	Initial Pore Diameter (mm)	Final Pore Diameter (mm)	Average Cross-Sectional Area Growth Rate (mm ² /sec)
167	2.54	0.34	1.10	1.1
333	1.69	0.56	1.63	3.2
333	2.54	0.45	1.76	2.6
500	1.69	0.66	2.09	2.4
500	2.54	0.55	1.86	6.8
667	1.69	0.35	1.82	3.2
667	3.39	0.43	0.73	0.3
833	1.69	0.43	1.63	2.8

Table 7 shows a tabulation of the final pore diameter measurements and its growth rate for the measured macro-pores in Alloy 6061. Each reporting of macro-pore measurements were based on one pore selected from the weld sample video. It was observed that pore growth is directly affected by the amount of hydrogen in the shielding gas and the travel speed.

The growth time reported in Figure 25 and Figure 26 is the time between the first resolvable appearances of the macro-pore in the weld pool to the time either the pore popped or became entrapped in the solidified metal. This is different than the weld exposure time. The welding travel speed determined the length of time the weld pool was exposed to the shielding gas hydrogen thus affecting how much hydrogen was transferred to the weld pool, allowing pores to form, grow and travel in the molten weld pool. The weld pool exposure time to the hydrogen in the shielding gas can be calculated by dividing the width of the weld pool by the travel speed, Equation 8 and can be seen in Figure 27. At fast travel speed, there may be less hydrogen pick up due to the exposure time which could explain the slower pore growth. The resolution on the in-situ data did not allow for accurate measurement of the weld pool length, therefore it was not possible to confirm the weld pool exposure time.

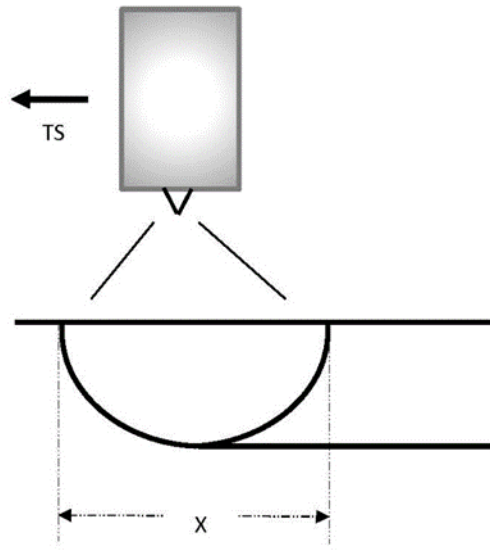


Figure 27: Schematic showing the exposure time the weld pool experiences.

$$\text{Exposure Time} = \frac{x}{TS} \quad \text{Equation 8}$$

where

x = weld pool length

TS = travel speed

Diffusional Pore Growth

Gas pores can grow in liquid by the diffusion of hydrogen to the pore from its surroundings. Studies typically distinguish between confined interdendritic pores and pores growing freely independent of the solid/liquid interface. Regarding the latter, pore growth in liquid has been formally modeled for castings [39] [40] [41] and weld metal

[42] based upon the assumption that concentration gradients change over time. If instead a condition of steady state is assumed as a first approximation, the flux of hydrogen atoms to a spherical pore follows Fick's first law, whereby the flux of atoms is the product of diffusivity (D) and concentration gradient ($\frac{\Delta C}{\Delta r}$) at the interface:

$$flux = \frac{atoms}{area \cdot time} = -D \frac{\Delta C}{\Delta r} \quad \text{Equation 9}$$

The diffusivity of hydrogen in molten aluminum near the melting point is reported to be $1.63 \times 10^{-3} \frac{cm^2}{s}$ [43]. Assuming spherical pores of radius r , it follows that the rate of atom movement at the interface is defined to be:

$$\frac{dn}{dt} = -(4\pi r^2)D \frac{(C_{\infty} - C_o)}{\delta} \quad \text{Equation 10}$$

where C_{∞} is hydrogen supersaturation, C_o is equilibrium solubility, and δ is the boundary layer thickness at the liquid/gas interface. C_{∞} is determined by how much hydrogen is charged into the weld pool by way of the shielding gas. C_o is determined by the equilibrium Sieverts law equation, Equation 1, and δ is unknown.

Relating atom accumulation to increased pore size, use of the ideal gas law relating pressure (P), volume (V), number of moles of gas(n), temperature (T) and the ideal gas constant (R):

$$PV = nRT \text{ (Ideal Gas Law)} \quad \text{Equation 11}$$

Rearranging

$$n = \frac{PV}{RT} \quad \text{Equation 12}$$

Taking the derivative of Equation 12 yields the change in number of moles of gas over time to become

$$\frac{dn}{dt} = \frac{P}{RT} \frac{dV}{dt} = \frac{4\pi r^2 P}{RT} \frac{dr}{dt} \quad \text{Equation 13}$$

since

$$V_{\text{spherical pore}} = \frac{4}{3}\pi r^3 \quad \text{Equation 14}$$

Equating this with Equation 13 and applying Equation 10:

$$\frac{dr}{dt} = \frac{\frac{dn}{dt} RT}{P4\pi r^2} = \frac{-(4\pi r^2)D(C_{\infty} - C_o)}{\delta} * \left(\frac{RT}{P4\pi r^2} \right) \quad \text{Equation 15}$$

Hence the growth rate becomes

$$\frac{dr}{dt} = \frac{RTD(C_{\infty} - C_o)}{\delta P} \quad \text{Equation 16}$$

This shows that the growth rate is proportional to the degree of supersaturation as depicted in Figure 28 [42].

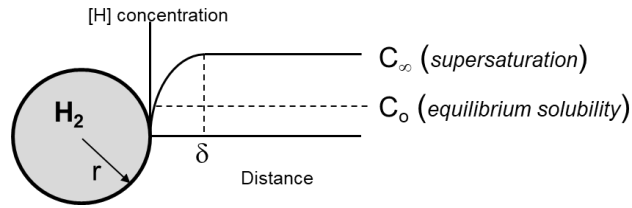


Figure 28: Schematic of hydrogen diffusion controlled pore formation [42].

The radial pore growth in Alloy 6061 at travel speed of 2.5 mm/s, Figure 29, shows an increase in growth rate as the amount of shielding gas hydrogen increases. This indicates there was an increase in the difference between the degree of supersaturation and the equilibrium solubility, $(C_{\infty} - C_o)$, as the amount of shielding gas hydrogen was increased. Thus indicating that the more hydrogen dissolved, the faster the pore growth rate.

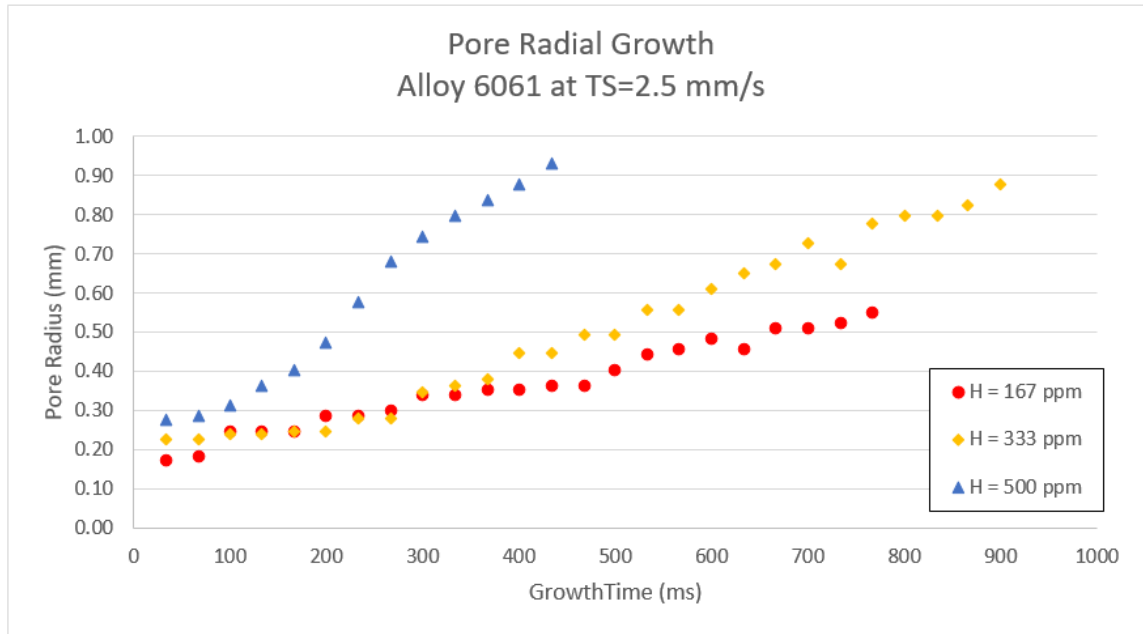


Figure 29: Radial pore growth in Alloy 6061 over time at travel speed 2.5mm/s and varying levels of shielding gas hydrogen.

Percent Porosity

Table 8 presents the metallography and gravimetric analysis data side by side. Metallography performed on each sample confirmed the presence of pores that have been entrapped in the solidified weld metal, even though they were not always resolvable with radiography. Each micrograph was used to compute the area percent porosity based on area of the weld metal, thus allowing us to indirectly obtain the volume of hydrogen held in the weld metal in the form of porosity. Gravimetric measurements performed on each sample yielded the absorbed gas as determined by density measurement calculations giving volume porosity. There is a certain amount of hydrogen gas in solution while the rest of it is present as porosity. The metallography data captured one cross-section along the weld whereas the gravimetric data looked at a volume of material reporting a more representative measurement of percent porosity of the weld.

Table 8: Percent Porosity for welded samples based on metallography and gravimetric testing

Alloy	Shielding Gas Hydrogen (ppm)	Travel Speed (mm/s)	Area porosity from Metallography (%)	Volume Porosity from Gravimetric Testing (%)
1100	0	1.69	0.509	1.44
	167		4.348	1.98
	333		2.164	2.71
	333		0.676	-
	333		-	3.31
	500		3.980	6.07
	667		2.518	3.42
	833		6.028	3.86
	667	2.54	3.043	2.31
	0	3.39	0.055	-
	333		0.818	0.09
	667		1.119	0.94
	1000		1.886	1.50
4047	0	2.54	0.019	0.05
	333		0.226	0.45
	667		0.528	1.14
	1000		0.319	1.59
	1000		1.029	1.22
	0	3.39	0.048	0.20
	333		0.465	0.50
	667		0.937	1.23
	1000		0.503	1.74
6061	0	1.69	1.052	1.27
	167		1.510	-
	500		3.613	2.13
	667		2.502	2.90
	833		1.029	1.70
	0	2.54	0.060	0.75
	167		1.327	1.56
	333		2.998	1.74
	500		1.286	1.70
	500		1.270	4.16
	0	3.39	0.006	-
	333		0.094	0.02
	667		0.703	1.16
	1000		1.509	1.22

- No data captured for sample

What follows is a summary of individual alloy behavior.

Alloy 1100

Figure 30 shows a set of images from the metallography samples from Alloy 1100 at a travel speed of 3.39 mm/s with varying amounts of shielding gas hydrogen. In Figure 30c the larger pores are located in the lower region of the weld pool, supporting the in-situ data.

In Alloy 1100 welding sample volumetric data, shown in Figure 31, showed that as the travel speed increased the amount of volumetric porosity decreased. In the percent volumetric porosity, Alloy 1100 welding samples showed an increase in percent porosity as the amount of hydrogen in the shielding gas increased as the travel speed was held constant.

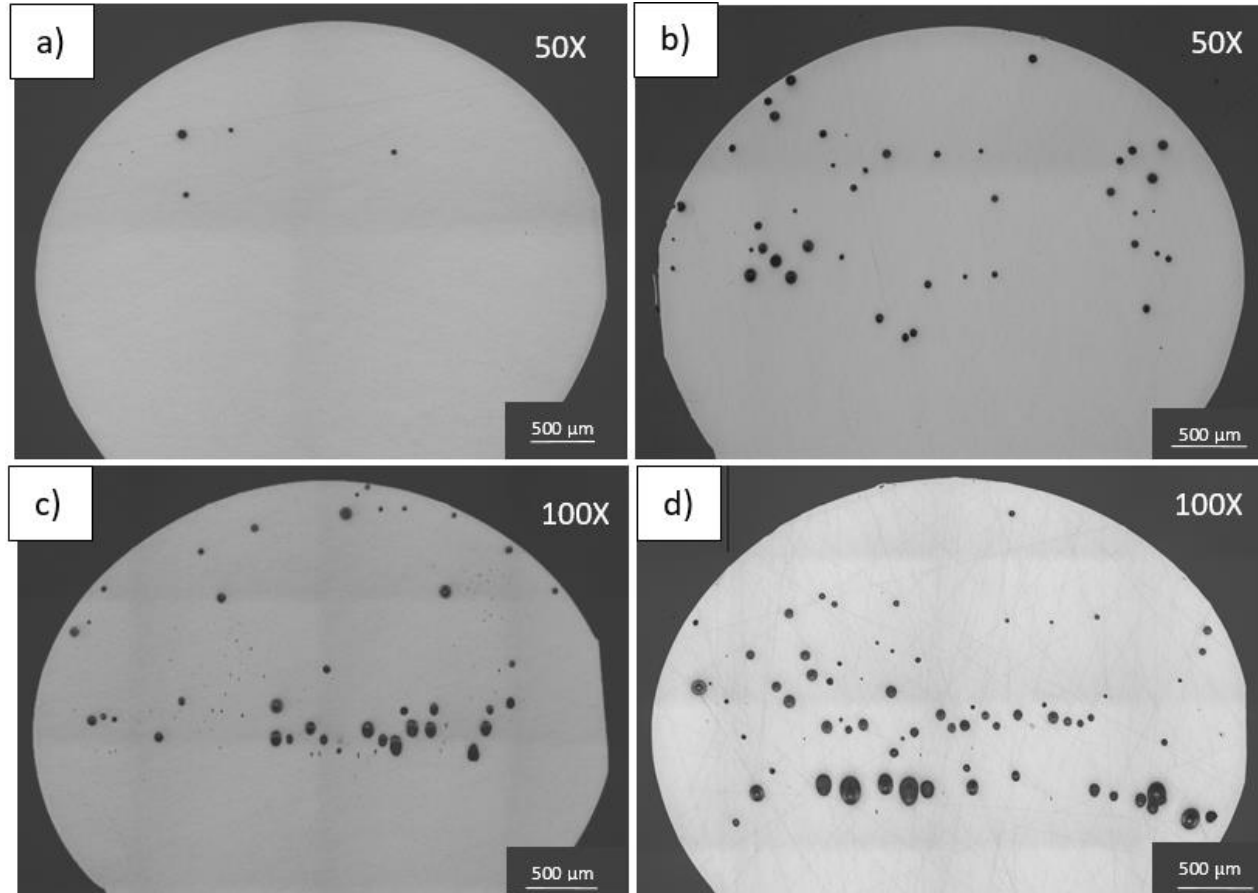


Figure 30: Alloy 1100 at travel speed of 3.39 mm/s using a) 0 ppm of shielding gas hydrogen with 0.055% porosity, b) 333 ppm of shielding gas hydrogen with 0.82% porosity, c) 667 ppm of shielding gas hydrogen with 1.12% porosity, and d) 1000 ppm of shielding gas hydrogen with 1.89% porosity.

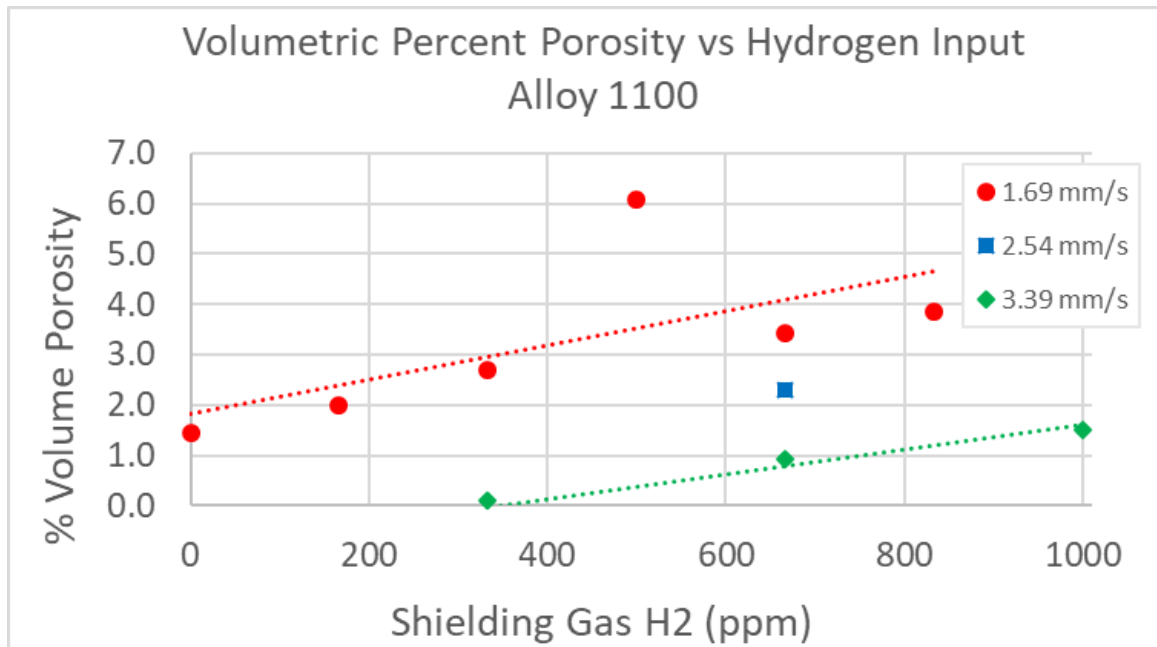


Figure 31: Volumetric percent porosity calculated from gravimetric testing showing the results from varying the amount of shielding gas hydrogen at different travel speeds in Alloy 1100.

Alloy 4047

Figure 32 shows the images from the metallography samples for Alloy 4047 at travel speed of 3.39 mm/s with varying amounts of shielding gas hydrogen. It is clear, as these micrographs are correlated to the in-situ data, that these pores show effervescence at the pool surface. Figure 32(a) has a calculated area porosity of 0.048% and a corresponding volume porosity of 0.20% with 0 ppm of shielding gas hydrogen. Figure 32 (d) has a calculated area porosity of 0.50% and a corresponding volume porosity of 1.74% with 1000 ppm of shielding gas hydrogen. No large macro-pores were observed. Figure 33 shows there is a smaller change in volumetric porosity percentage when looking at the difference between the 2.54 mm/s and 3.39 mm/s travel speed. There is

still an increase of percentage porosity as the amount of shielding gas hydrogen was increased when the travel speed is held constant.

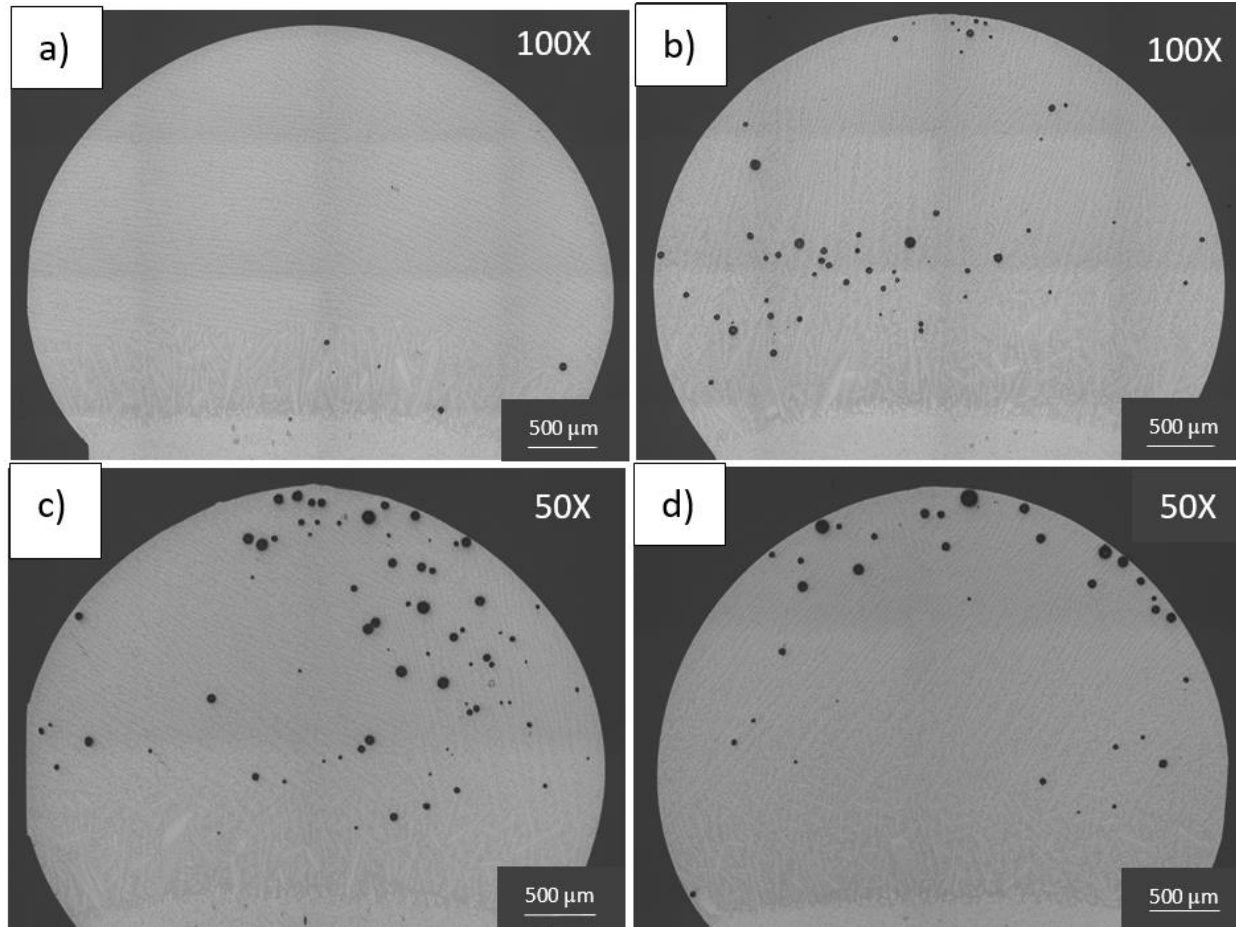


Figure 32: Alloy 4047 at travel speed of 3.39 mm/s with the following levels of shielding gas hydrogen: a) 0 ppm contained 0.048% porosity, b) 333 ppm contained 0.47% porosity, c) 667 ppm contained 0.94% porosity, and d) 1000 ppm contained 0.50% porosity.

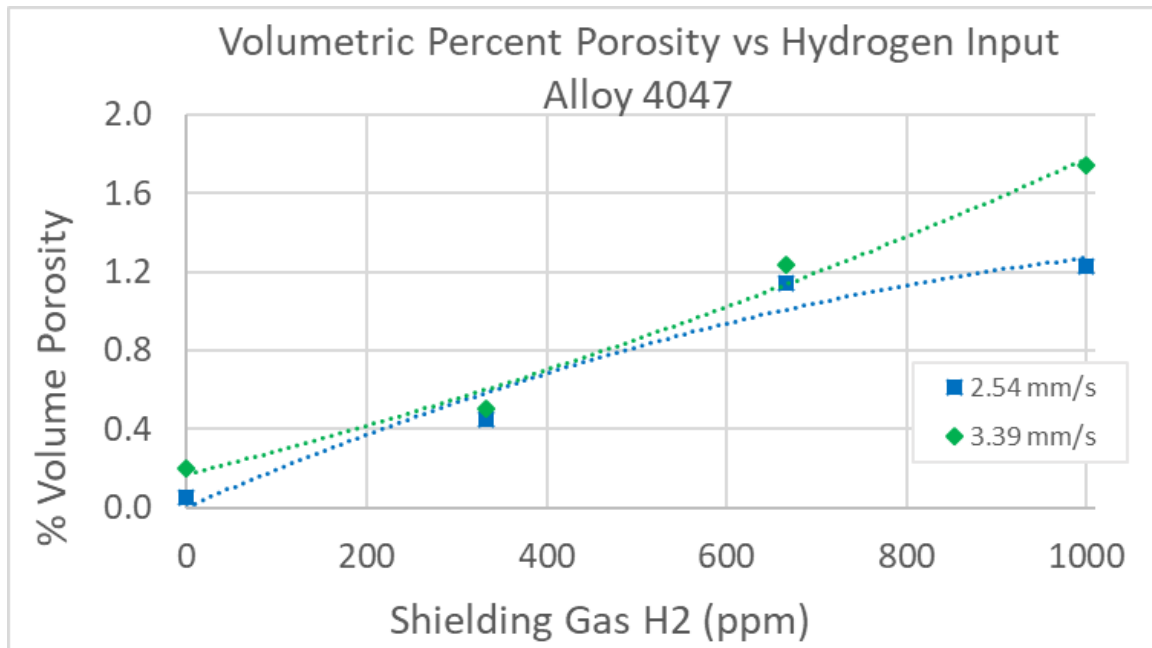


Figure 33: Volumetric percent porosity using various amounts of shielding gas hydrogen at different travel speeds in Alloy 4047.

Alloy 6061

Figure 34 shows the images from the metallography samples for Alloy 6061 at a travel speed of 3.39 mm/s with varying amounts of shielding gas hydrogen. Figure 34a) 0 ppm of shielding gas hydrogen contained 0.006% porosity, b) 333 ppm of shielding gas hydrogen contained 0.094% porosity, c) 667 ppm of shielding gas hydrogen contained 0.70% porosity, and d) 1000 ppm of shielding gas hydrogen contained 1.51% porosity. As shown in Figure 35, it can be seen that as travel speed is increased there is a reduction in macro-porosity formation. As the travel speed is increased in Alloy 6061, while keeping the amount of shielding gas constant, the amount of volumetric porosity decreases. Figure 35 shows there is a relationship between porosity volume percentage and travel speed. There is still a decrease of percentage porosity as the amount of

shielding gas hydrogen was increased when the travel speed is increased. This could be due to the exposure time the molten weld pool has under the shielding gas.

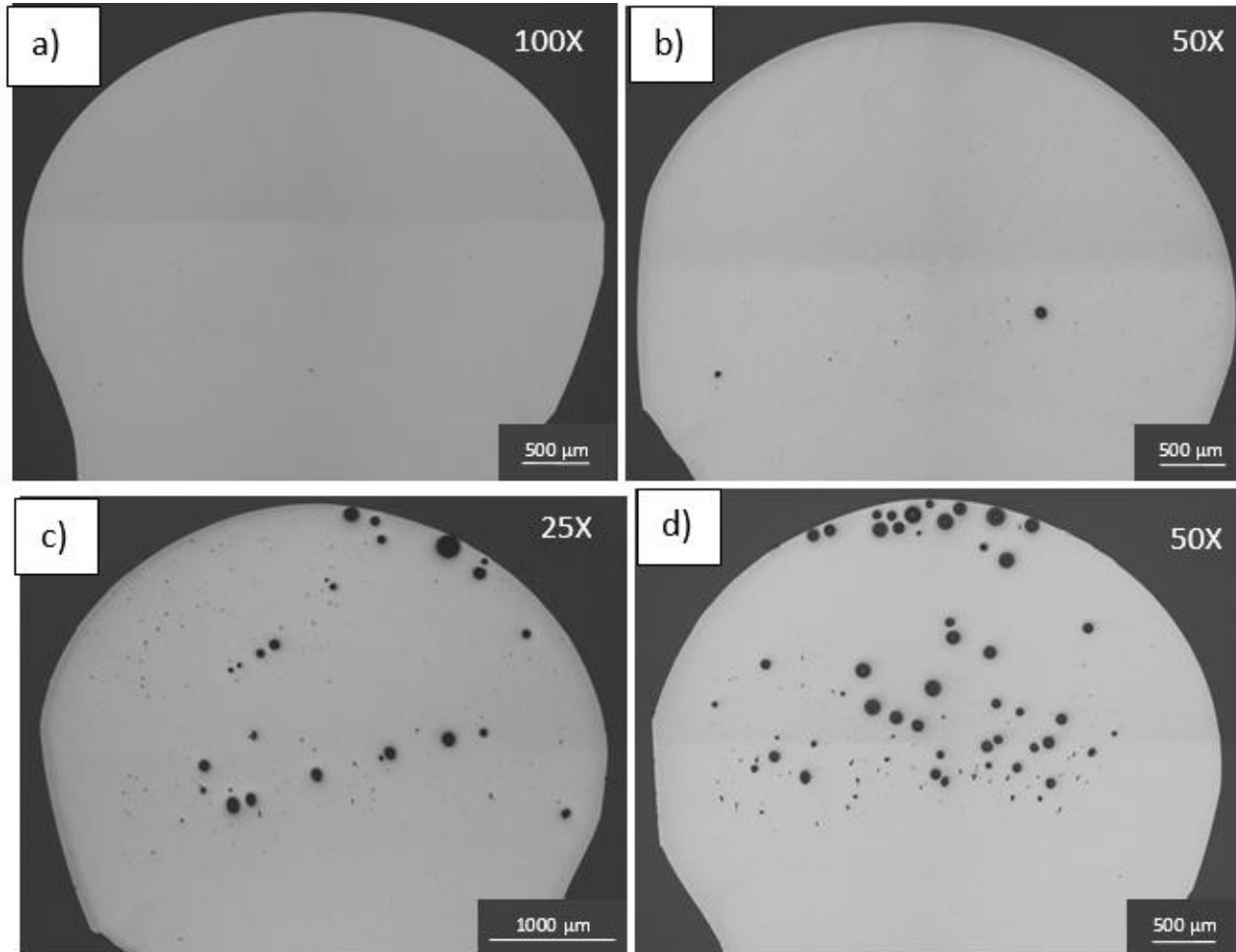


Figure 34: Alloy 6061 at travel speed of 3.39 mm/s with the following levels of shielding gas hydrogen: a) 0 ppm, b) 333 ppm, c) 667 ppm, and d) 1000 ppm.

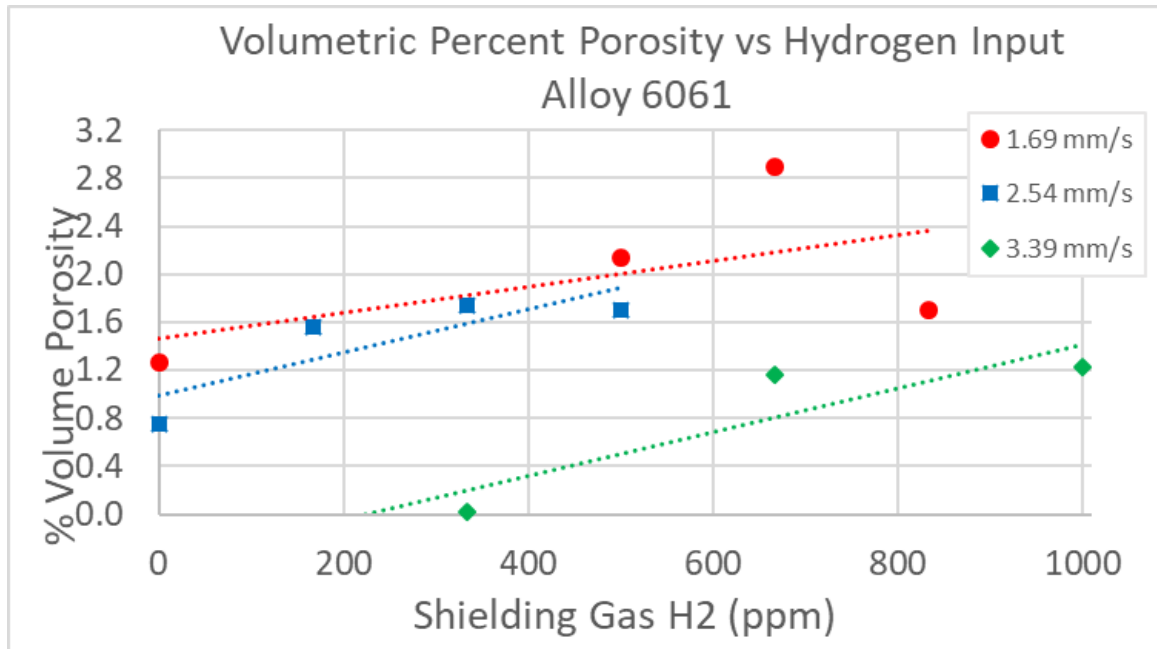


Figure 35: Volumetric percent porosity using various amounts of shielding gas hydrogen at different travel speeds in Alloy 6061.

It can be seen across all alloys, that there is an increase in volumetric percent porosity as the travel speed is decreased. Thus agreeing with the in-situ pore growth measurements from Figure 25. At slower travel speed the molten puddle is under the arc for a longer period of time which increases the exposure time to shielding gas.

When comparing the difference between the area percent porosity from metallography, Figure 36 and the volumetric percent porosity from gravimetric testing, Figure 37, there is a difference in the results. There are some outliers that do not comply due to the chance sectioning of the metallography sample. It can be seen that with the metallography, for a given amount of hydrogen added to the shielding gas, Alloy 1100 generates the highest area of pores and 6061 the least. With the volumetric results from this section, Alloy 4047 highest level of volumetric porosity, while 6061 had the least.

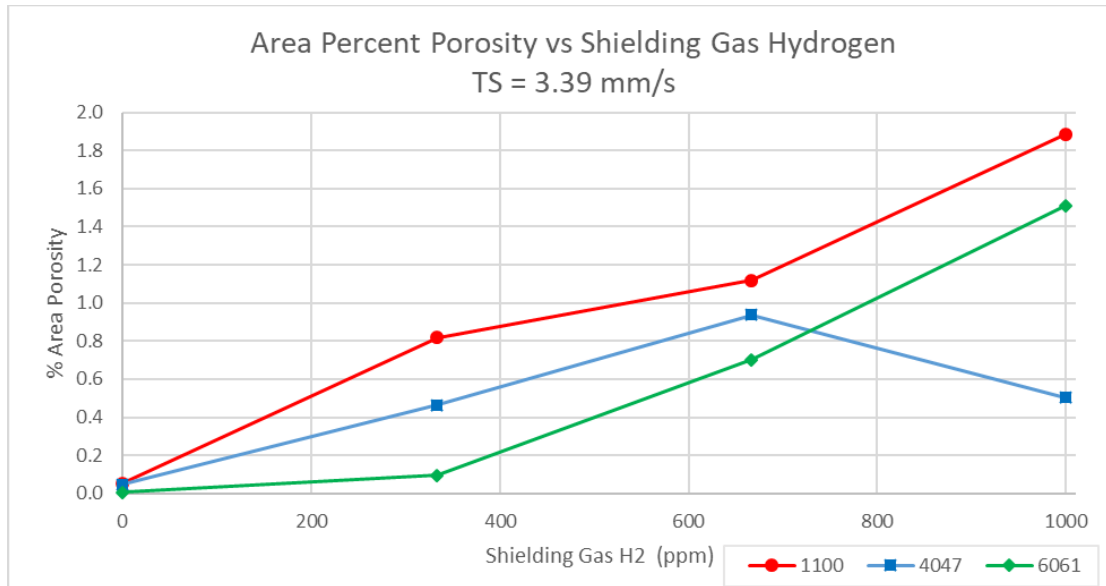


Figure 36: Area percent porosity using various amounts of shielding gas hydrogen on different alloys at a travel speed of 3.39 mm/s.

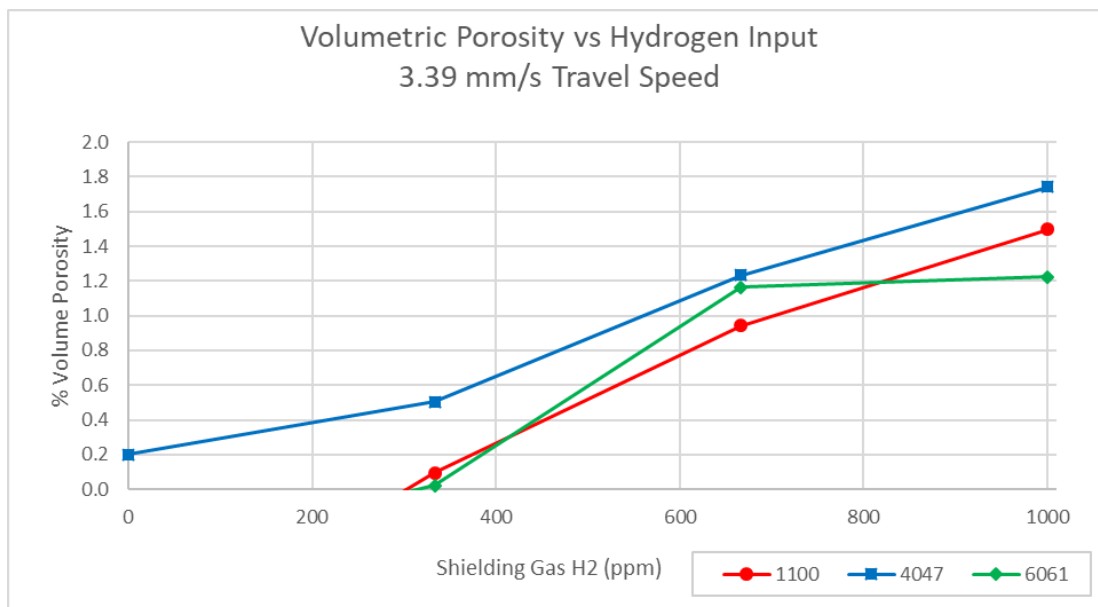


Figure 37: Volumetric percent porosity using various amount of shielding gas hydrogen on different alloys at a travel speed of 3.39 mm/s.

Engulfment/Banding

Pore Engulfment. Engulfment of gas pores has also been studied [44] [45] and they are believed to be influenced by size and travel speed in a manner similar to inclusions. The difference is that a pore can change shape (i.e. become elongated) and can grow from partitioned solute (e.g. hydrogen) streaming to the pore from the solid/liquid interface. The observed rapid growth of macro-pores in this study, as mentioned in the in-situ results section, may be related to this phenomenon. Pores located away from the solidification front depend upon diffusion of hydrogen through the surrounding liquid, whereas pores in direct contact with the solidification front have access to concentrated hydrogen partitioned during solidification.

Catalina et al. [22] modeled the action of pushing versus engulfment of oxide inclusions at the solidification interface in castings. Specifically, inclusions will become engulfed, i.e. undergo push-engulf transition (PET), if the critical velocity is exceeded for a given particle size. For a given inclusion size and increasing travel speed, the drag force on a particle will increase to the point where it becomes energetically favorable to engulf, creating new solid-inclusion interfaces. Using the force balance equation of force (F) equals mass (m) times the acceleration (a), this critical condition, as defined by Catalina et al., can be defined between particle acceleration, interface force F_i , and drag force F_d :

$$m \frac{dv}{dt} = F_i - F_d \quad \text{Equation 17}$$

where *acceleration* = $\frac{dv}{dt}$ and *v* = *velocity*.

Their analysis resulted in a prediction for critical velocity for PET on an aluminum-zirconia system based on particle size (r) [22]:

$$v_c = 1e^{-11}r^{-1.3883} \quad \text{Equation 18}$$

Thus Equation 18 shows as the aluminum-zirconia particle radius increases, the critical velocity decreases. If the solidification velocity is below the critical velocity for particle engulfment, the particle will continue to be pushed. This relationship may be similar to what the pore is experiencing in the weld pool.

It is not clear why only some pores experience rapid growth, but those that do, appear to be only partially engulfed; i.e. part of the pore remains in the liquid and part of it is anchored in the solid. As the part of the pore in the liquid grows rapidly, it migrates upward influenced by buoyancy. Continued growth on a partially engulfed pore results in an elongated wormhole, angled upward, smaller at the start, and sometimes escaping at the surface. It may be that in certain instances, the growth of a pore occurs very rapidly and it breaches the surface before the solidification front reaches it.

The in-situ radiography showed rows of micro-pores solidified in the weld. This is believed to be caused by the oscillatory motion of the weld pool and has been observed elsewhere as first noted by D'Annessa who referred to this as "banding" [46]. Banding, periodic engulfment of the micro-pores, was only evident during the in-situ data for Alloy

1100 and mainly at a travel speed of 1.69 mm/s, as seen in Figure 38. The average frequency of the banding observed was measured to be 3.1 Hz. According to D'Annessa, this oscillation may be attributed to the current frequency of the power source and the shape of the weld pool. The lack of banding observed in Alloy 4047 and 6061 may be the limitation of the radiography parameters used during this study both due to the resolution and ability to see micro-pores of a certain size.

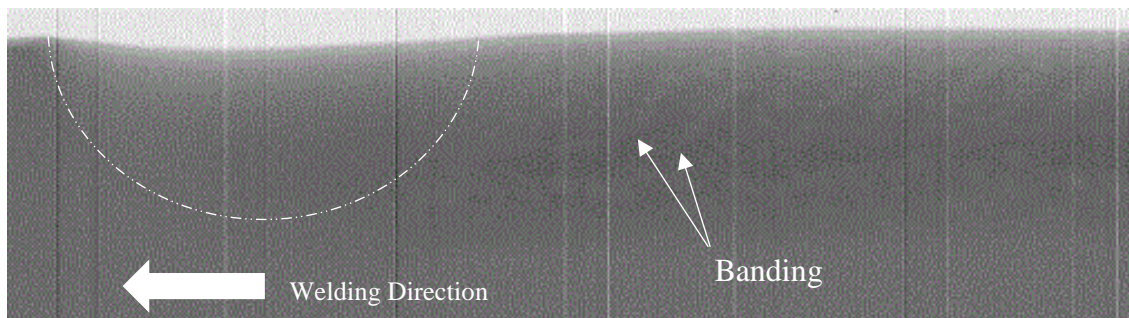


Figure 38: Welded sample using 667 ppm of shielding gas hydrogen, is an Alloy 1100 showing pore banding forming and solidification.

The observation of periodic entrapment of a row of pores is likely due to a natural oscillation frequency of the weld pool triggered by the pulsing arc. As the pool oscillates back and forth, the forward motion of the pool will add to the normal transitional velocity of the torch, which may exceed the critical velocity for PET.

Effervescence

Effervescence, the rapid escape of multiple micro-gas pores at the weld pool surface, was observed during in-situ radiographs. Figure 39 shows an example of the effervescence seen in an Alloy 4047 radiograph. Micro-pores are present at the leading

and trailing edge of the weld pool near the surface. These micro-pores can be physically seen on the solidified weld surface with a portion of them open to the surface. Figure 40, Figure 41 and Figure 42 are photographs of the top surface of the final weld surface from samples welding at 3.39 mm/s with varying levels of hydrogen in Alloy 1100, Alloy 4047, and Alloy 6061, respectively. Alloy 4047 showed more effervescence activity in the in-situ radiographs compared to Alloy 1100 and 6061. Although it wasn't always visible in the radiographs, the photographs show this effect in all the alloys. Generally, Alloy 6061 was less susceptible than Alloy 4047 potentially due the chemical composition of the base material.

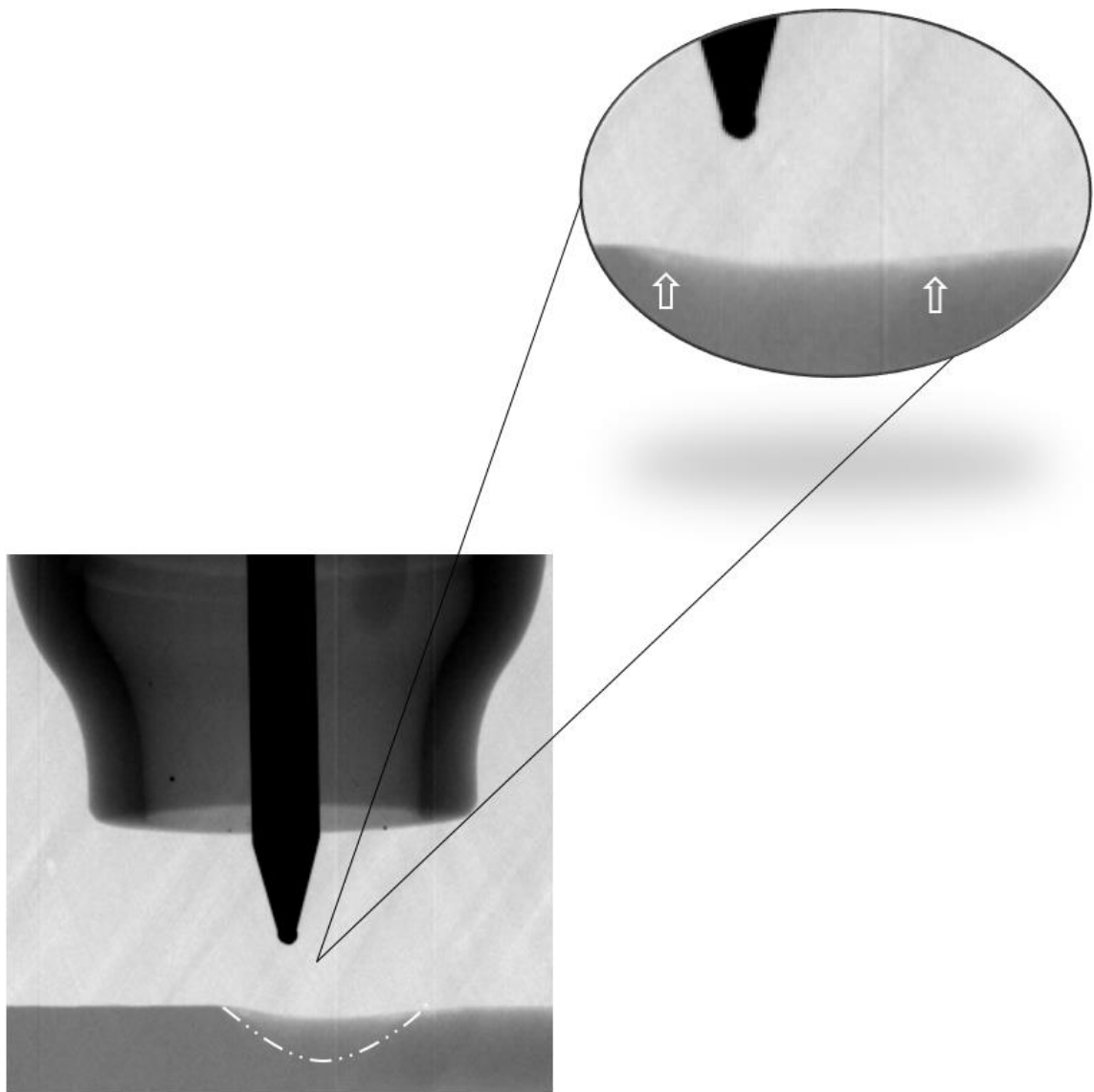


Figure 39: Alloy 4047 showing effervescence at the leading and trailing edge of the weld pool surface.

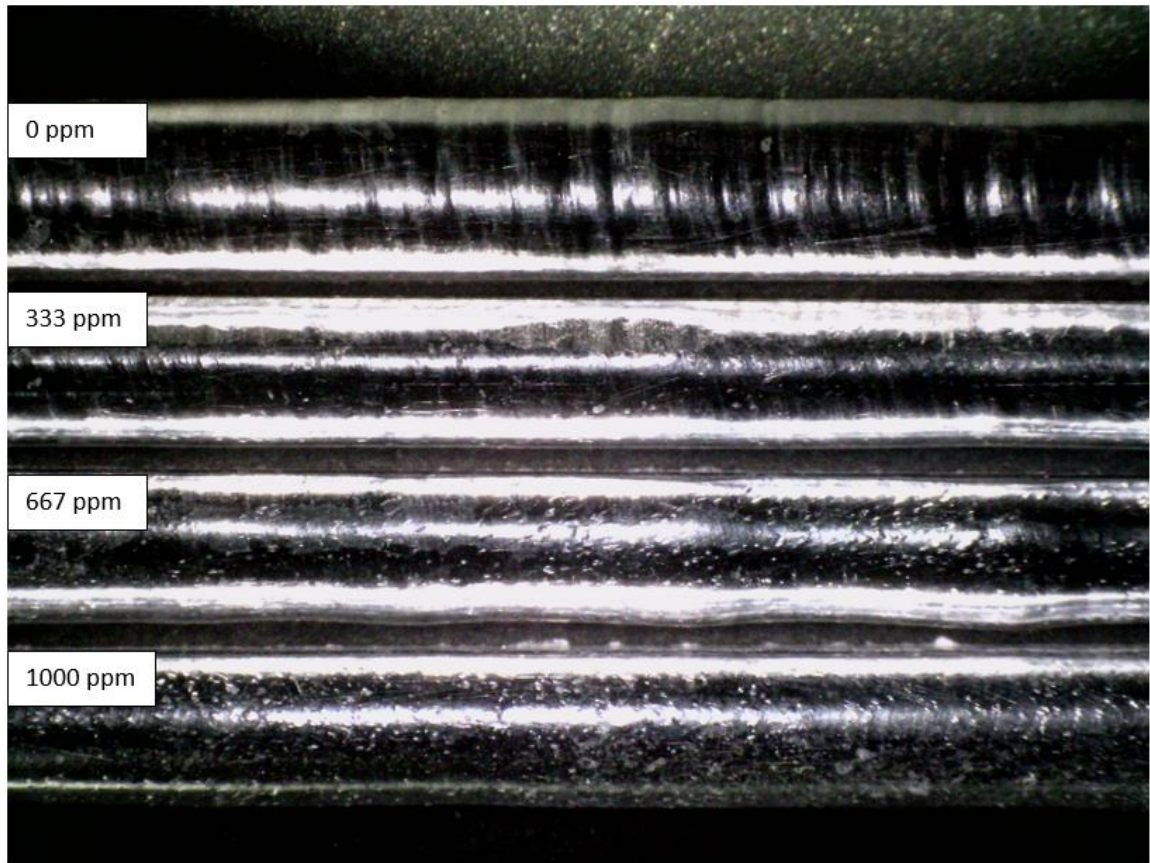


Figure 40: Photograph of 1100 weld metal, exhibiting sub-surface porosity with varying amounts of shielding gas hydrogen at a travel speed of 3.39 mm/s.

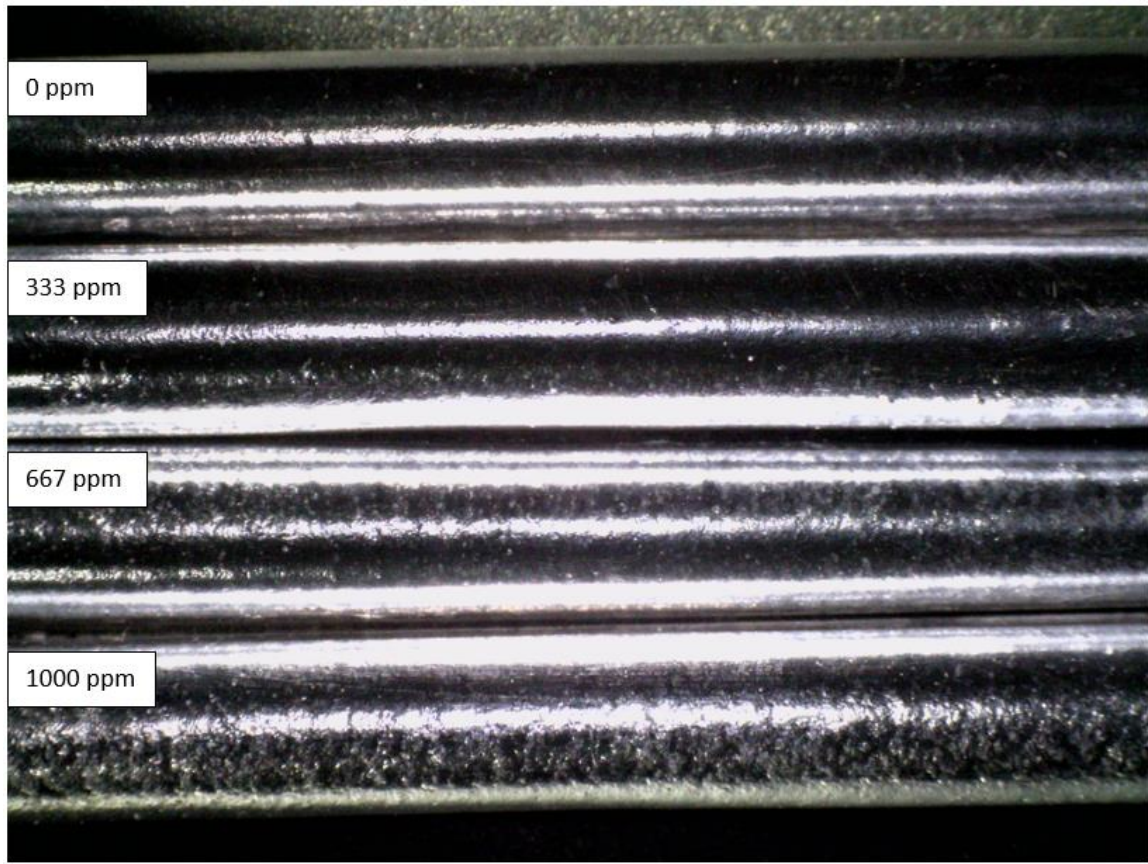


Figure 41: Photograph of 4047 weld metal, exhibiting sub-surface porosity with varying amounts of shielding gas hydrogen at a travel speed of 3.39 mm/s.

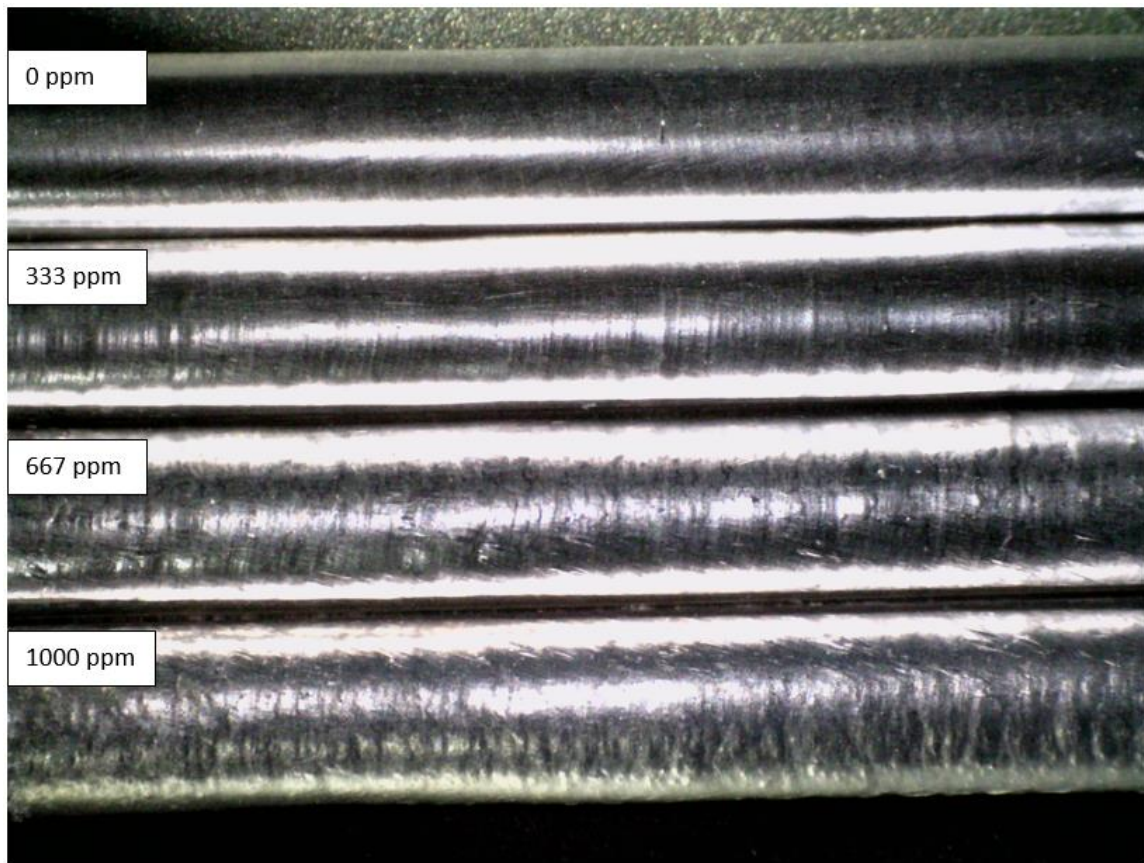


Figure 42: Photograph of 6061 weld metal, exhibiting sub-surface porosity with varying amounts of shielding gas hydrogen at a travel speed of 3.39 mm/s.

Limitations:

This experimental set-up and execution of this study was limited by time and resources. The radiography parameters were selected based on brief period of testing. Further testing with the equipment is needed to observe the limitation of this radiography technique, i.e. to improve resolution and the frames per second. Recommendation for future work would also include finding a baseline set of welding parameters, a control, to ensure all equipment is functioning appropriately. It is recommended that a future study would duplicate welding samples to ensure consistent results, control electrode shape, and measure the retained hydrogen in the weld metal.

Chapter IV. Conclusion

Radiographic Technique.

1. The radiographic technique used in this study for in-situ observation proved a useful means to study macro-porosity formation and growth in aluminum alloys 1100, 4047, and 6061.
2. Resolution, image detail, is influenced by the material (aluminum), its thickness (4 mm), and the x-ray energy (150 keV), in addition to the frame rate (7.5 fps or 30 fps) and magnification (10x). The smallest pore that could be measured was roughly 0.09 mm (90 μm).

Influence of shielding gas hydrogen and travel speed.

1. The amount of hydrogen added in the shielding gas played an important role in the observation of macro-pore formation. In Alloy 1100, micro-porosity was observed with all levels of shielding gas hydrogen. The macro-pore growth began at shielding gas hydrogen levels of 333 ppm and greater. In Alloy 4047, obvious micro-porosity was observed at shielding gas hydrogen levels of 333 ppm and greater. Macro-pore growth was only observed, briefly, at weld start while welding with 1000ppm of shielding gas hydrogen. In Alloy 6061, micro-porosity

was observed with all levels of shielding gas hydrogen. Macro-pore growth was observed at shielding gas hydrogen levels greater than 167 ppm.

2. Travel speed had a strong effect on pore size on Alloys 1100 and 6061, where the slowest speed (1.69 mm/s) had the largest pores, and the fastest speed (3.39 mm/s) resulted in no resolvable pores.
3. In Alloy 1100, the macro-pore groups could be prevented by increasing travel speed to 2.54 mm/s at a shielding gas hydrogen levels of 333 ppm. Macro-pore growth could be prevented by increasing travel speed to 3.39 mm/s at shielding gas hydrogen level of 333 ppm.
4. In Alloy 6061, the macro-pore growth could be prevented by increasing travel speed to 2.54 mm/s at a shielding gas hydrogen levels of 333 ppm. Macro-pore growth could be prevented by increasing travel speed to 3.39 mm/s at a shielding gas hydrogen level of 333 ppm.
5. Gravimetric results showed that an increase in travel speed to 3.39 mm/s yielded a smaller percent of volumetric porosity compared to the 2.54 mm/s travel speed.

Pore Formation.

1. The macro-pores originated at the bottom of the weld pool for Alloy 1100 while for Alloy 6061, macro-pores originated at the leading edge of the weld pool.
2. The pore formation appeared to be related to fluid flow patterns as affected by Marangoni fluid flow. The nucleation of macro-pores arise from the rapid

movement of hot metal under the arc to the cooler region at the pool's outer boundary resulting in super saturation.

3. In general the micrographs showed Alloy 1100 had macro-pores in an elliptical shape and mostly near the bottom of the weld pool; Alloy 4047 micro-pores were circular in shape and densely populated near the surface of the weld pool; Alloy 6061 had macro-pores circular in shape and were at their largest near the weld pool surface.

Pore Movement.

1. The porosity remained on the outer “still” fusion boundary of the weld pool. Pores did not enter the bulk of the weld pool. In Alloy 6061, when the macro-pore grew to a certain size at the leading edge of the weld pool, the pore migrated towards the trailing edge of the weld pool by moving along the pool bottom. Pore movement upward is influenced by buoyancy and fluid flow. In Alloy 1100, macro-pores remained at the trailing edge of the weld pool as they grew upward.
2. Fluid flow observed during in-situ radiography was very rapid and tracked by the movement of the macro-pores in Alloy 1100 and Alloy 6061. Alloy 1100 displayed fluid flow indicating an inward flow as the macro-pores were observed first at the bottom of the weld pool while Alloy 6061 displayed macro-pores forming at the leading edge indicating an outward fluid flow.

Pore Growth.

1. It was observed there was rapid growth of single pores to large dimensions of 1 mm and occasional escape. Pore growth rate increased with increased hydrogen saturation and slower travel speeds. Commercially pure aluminum 1100 had the greatest amount of porosity formed.

Engulfment.

1. Micro-pores became fully engulfed with periodic oscillation of the weld pool leading to banding. The banding followed the shape of the weld pool.
2. In Alloy 1100, when macro-pores were partially engulfment this resulted in elliptical-shaped pores growing in the direction of the weld.
3. Macro-pores in Alloy 6061 were not partially engulfed and remained circular in shape.

This research offered confirmation and enlightenment for both theory and practical use in the understanding of porosity in aluminum welds. This work confirmed 1) Woods [13] hypothesis that macro-pores nucleated at the bottom of the weld pool or at the leading edge of the pool on the surface, not requiring interdendritic segregation of hydrogen; 2) Marangoni forces, dependent on alloying elements, affected pore movement in the weld pool, similar to what Kou, et al [6] predicted; and 3) the method of adding hydrogen through the shielding gas was an effective and controllable way to introduce hydrogen into the weld pool to simulate hydrogen contamination coming from the filler wire or moisture in the shielding gas. For practical purposes, it was shown that 1) even with its limited resolution, digital radiographic equipment can be used to study in-situ macro-pore formation at slow travel speed; 2) aluminum-silicon alloys were not prone to macro pore formation; and 3) use of travel speeds greater than 3 mm/s helped to eliminate macro-pores from the weld pool.

Bibliography

- [1] D. Talbot, The Effects of Hydrogen in Aluminum and Its Alloys, Maney Pub., 2004.
- [2] E. M. Honig, Effects of Cluster Porosity on the Tensile Properties of Butt Weldments in T-1 Steel, Champaign, Illinois: Army Construction Engineering Reserch Laboratory, 1974.
- [3] Welding Handbook, vol. Volume 1: Welding Science and Technology, American Welding Society, 1981.
- [4] S. W. Pierce, "Thermocapillarity and Arc Phenomena in Stainless Steel Welds," Colorado School of Mines, Golden, Colorado, 1993.
- [5] P. G. Jonsson, J. Szekely, R. Choo and T. P. Quinn, "Mathematical models of transport phenomena associated with arc-welding processes: a survey," *Modelling and Simulation in Materials Science and Engineering*, pp. 995-1016, 1994.
- [6] S. Kou and Y. H. Wang, "Weld Pool Convection and Its Effect," *Welding Journal*, vol. 65, pp. 63s-70s, 1986.
- [7] D. L. Olson, R. Dixon and A. L. Liby, Welding Theory and Practice, The Netherlands: Elsevier Science Publishers BV, 1990.
- [8] C. Heiple and J. Roper, "MEchanism for Minor Element Effect on GTA Fusion Zone Geometry," *Welding Research Supplement*, pp. 97s-102s, 1982.
- [9] R. C. Andrew, "Sources of Hydrogen Prosoity in Aluminum Alloy Welds," *Aust. Weld. Res.*, vol. 4(2), pp. 1-19, 1975.
- [10] C. Ransley and H. Neufeld, "The Solubility of Hydrogen in Liquid and Solid Aluminum," *J. J. Inst. Metals*, vol. 74, pp. 599-620, 1948.
- [11] W. R. Opie and N. J. Grant, "Hydrogen Solubility in Aluminum and Some Aluminum Alloys," *Transactions AIME*, vol. 188, pp. 1237-1241, 1950.
- [12] T. Zacharia, A. H. Eraslan and D. K. Aidun, "Modeling of Autogeneous Welding," *Welding Research*, pp. 53s-62s, March 1988.
- [13] R. A. Woods, "Porosity and Hydrogen Absorption in Aluminum Welds," *Welding Research Council*, pp. 97-108, March 1974.
- [14] S. A. Gedeon and T. W. Eagar, "Thermochemical Analysi sof Hydrogen Absorption in Welding," *Welding Research Council*, pp. WRC Bulletin 347, 264-271, July 1989.

- [15] C. E. Cross, D. L. Olson and S. Liu, "Chapter 9: Aluminum Welding," in *Handbook of Aluminum: Physical Metallurgy and Processes*, CRC Press, LLC, 2003, pp. 481-532.
- [16] N. Coniglio and C. E. Cross, "Mechanism for Solidification Crack Initiation and Growth in Aluminum Welding," *The Minerals, Metals & Materials Society*, vol. 40A, pp. 2718-2728, November 2009.
- [17] J. Campbell, Castings, Oxford, Great Britain: Butterworth-Heinemann, 1991.
- [18] J. F. Rudy and E. J. Rupert, "Effects of Porosity on Mechanical Properties of Aluminum Welds," *Welding Research Supplement*, pp. 322s-336s, July 1970.
- [19] R. J. Shore and R. B. McCauley, "Effects of Porosity on High Strength Aluminum 7039," *Welding Research Supplement*, pp. 311s-321s, July 1970.
- [20] A. Farzadi, S. Serajzadeh and A. H. Kokabi, "Investigation of weld pool in aluminum alloys: Geometry and solidification microstructure," *International Journal of Thermal Sciences*, pp. 809-819, 2010.
- [21] K. D. Carlson, Z. Lin and C. Beckermann, "Modeling the Effect of Finite-Rate Hydrogen Diffusion on Porosity Formation in Aluminum Alloys," *Metallurgical and Materials Transactions B*, vol. 38B, pp. 541-555, August 2007.
- [22] A. V. Catalina, S. Mukherjee and D. M. Stefanescu, "A Dynamic Model for the Interaction between a Solid Particle and an Advancing Solid/Liquid Interface," *Metallurgical and Materials Transactions A*, vol. 31A, pp. 2559-2568, 2000.
- [23] D. M. Stefanescu, F. R. Juretzko, B. K. Dhindaw, A. Catalina, S. Sen and P. A. Curreri, "Partial Engulfment and Pushing by Solidifying Interfaces: Part II. Microgravity Experiments and Theoretical Analysis," *Metallurgical and Materials Transactions A*, vol. 29A, pp. 1697-1706, June 1998.
- [24] S. I. Rokhlin and A. C. Guu, "Computerized Radiographic Sensing and Control of an Arc Welding Process," *Welding Journal*, vol. 69, pp. 83s-97s, 1990.
- [25] S. Fujinaga, H. Takenaka, T. Narikiyo, S. Katayama and A. Matsunawa, "Direct Observation of Keyhole Behaviour during Pulse Modulated High-Power Nd:YAG Laser Irradiation," *Journal of Applied Physics*, vol. 33, pp. 492-497, 2000.
- [26] S. Katayama, Y. Kobayashi, M. Mizutani and A. Matsunawa, "Effect of Vacuum on Penetration and Defects in Laser Welding," *Journal of Laser Applications*, vol. 13, pp. 187-192, 2001.
- [27] T. Yamada, T. Shobu, S. Yamashita, A. Nishimura, T. Muramatsu and U. Komizo, "Visualization of Technique for Quantitative Evaluation in Laser Welding Process," in *In-Situ Studies with Photons, Neutrons, and Electrons Scattering II*, Springer Publications, 2014, pp. 201-215.
- [28] F. T. Boateng, U. Ewert, T. Kannengiesser, A. Griesche, U. Zscherpel, A. Kromm, S. Hohendorf and B. Redmer, "Real-Time Radiography for Observation of Crack Growth during GTA Welding," *Welding in the World*, vol. 60, pp. 931-937, 2016.
- [29] S. M. Hojjatzadeh, N. Parab, W. Yan, Q. Guo, L. Xiong, C. Zhao, M. Qu, L. Escano, X. Xiao, K. Fezzaa, W. Everhart, T. Sun and L. Chen, "Pore Elimination

- Mechanisms during 3D Printing of Metals," *Nature Communications*, pp. 1-8, 2019.
- [30] T. A. Association, Aluminum Standards and Data, The Aluminum Association, 1984.
 - [31] D. Sekulic, "Brazing of Aluminum Alloys," in *ASM Handbook ,Volume 2A, Aluminum Science and Technology*, ASM International, 2018, pp. 763-782.
 - [32] M. Suban and J. Tusek, "Influence of hydrogen in argon as a shielding gas in arc welding of high-alloy stainless steel.," in *Annual Assembly of the International Institue of Welding*, Hamburg, 1998.
 - [33] C. Cross, A. Barraza, C. Stull, J. Martinez and C. Fink, *Hydrogen Contamination and Porosity Formation in Aluminum Welds*, Los Alamos National Laboratory, 2018.
 - [34] "Mettler Toledo," Aug 2020. [Online]. Available: https://www.mt.com/de/en/home/applications/Laboratory_weighing/density-measurement.html. [Accessed August 2020].
 - [35] S. Kou and D. K. Sun, "Fluid Flow and Weld Penetration in Stationary Arc Welds," *Metal. Trans.*, vol. 16A, pp. 203-213, 1985.
 - [36] R. A. Saravanan, J. M. Molina, J. Narciso, C. Garcia-Cordovilla and E. Louis, "Surface Tension of Pure Aluminum in Argon/Hydrogen and Nitrogen/Hydrogen Atmospheres at High Temperatures," *J. Mater. Sci. Letters*, vol. 21, pp. 309-311, 2002.
 - [37] S. Kou and Y. Wang, "WeldPool Convection and Its Effect," *Welding Research Supplement*, pp. 63s-70s, 1986.
 - [38] I. Bainbridge and J. A. Taylor, "The Surface Tension of Pure Aluminum and Aluminum Alloys," *Metal. Mater. Trans.*, vol. 44A, pp. 3901-3909, 2013.
 - [39] P. D. Lee and J. D. Hunt, "Hydrogen Porosity in Direction Solidified Aluminum-Copper Alloys," *Metal.Mater. Trans.*, vol. 44A, pp. 3901-3909, 2013.
 - [40] R. C. Atwodd, S. Sridhar, W. Zhang and P. D. Lee, "Diffusion-Controlled Growth of Hydrogen Pores in Aluminum-Silicon Castings: In Situ Observation and Modelling," *Acta. Mater.*, vol. 48, pp. 405-417, 2000.
 - [41] K. Dai, B. Wand, F. Xue, S. Liu, J. Huang and J. Zhang, "Formation of Nitrogen Bubbles During Solidificaion of Duples Stainless Steels," *Metal. Mater. Trans.*, vol. 49B, pp. 2011-2020, 2018.
 - [42] J. L. Huang, N. Warnken, J. Gebelin, M. Strangwood and R. C. Reed, "On the Mechanism of Porosity Formation During Welding of Titanium Alloys," *Acta. Mater.*, vol. 60, pp. 3215-3225, 2012.
 - [43] C. E. Ransley and D. Talbot, *Z.Metallkunde*, vol. 46, p. 328, 1955.
 - [44] D. Shangguan and D. M. Stefanescu, "In Situ Observaion of Interactions Between Gaseous Inclusions and an Advancing Solid/Liquid Interface," *Metal. Trans.*, vol. 22B, pp. 385-388, 1991.

- [45] A. V. Catalina, D. M. Stefanescu, S. Sen and W. F. Kaukler, "Interaction of Porosity with Planar Solid/Liquid Interface," *Metallurgical and Materials Transactions A*, vol. 35A, pp. 1525-1538, May 2004.
- [46] A. D'Annessa, "Sources and Effects of Growth Rate Fluctuations During Weld Metal Solidification," *Welding Journal*, vol. 49, pp. 41s-45s, 1970.
- [47] D. E. Talbot, *The Effects of Hydrogen in Aluminum and Its Alloys*, London: Maney Publishing, 2004.
- [48] S. Kou, T. Kanevsky and S. Fyfe, "Welding Thin Plates of Aluminum Alloys-A Quantitative Heat-Flow Analysis," *Welding Research Council*, pp. 175-181, June 1982.
- [49] B. Dixon, N. Baldwin and M. Coghill, "Real Time Radiography of Weld Solidification," *Australian Welding Research*, vol. 16, pp. 70-74, 1988.
- [50] A. V. Catalina, S. Mukherjee and D. M. Stefanescu, "A Dynamic Model for the Interaction between a Solid Particle and an Advancing Solid/Liquid Interface," *Metallurgical and Materials Transactions A*, vol. 31A, pp. 2559-2568, 2000.

Appendix A. Sample Weld Parameters

Table 9: Weld Sample Parameters

Welding Parameters				Radiography Machine				
Alloy	Shielding Gas Hydrogen (ppm)	Current (A)	Travel Speed (mm/s)	Energy (keV)	Current (μA)	Frame Rate (fps)	Source to Detector (mm)	Source to Part (mm)
1100	0	50-52	1.69	100	100	7.5	762	76.2
1100	0	75	3.39	100	100	30	381	38.1
1100	167	52	1.69	100	100	7.5	762	76.2
1100	333	55	1.69	100	100	7.5	762	76.2
1100	333	50	1.69	100	100	7.5	762	76.2
1100	333	85	1.69	100	100	7.5	762	76.2
1100	333	70	3.39	100	100	30	381	38.1
1100	500	52	1.69	100	100	7.5	762	76.2
1100	667	52	1.69	100	100	7.5	762	76.2
1100	667	60	2.54	100	100	30	381	38.1
1100	667	65	3.39	100	100	30	381	38.1
1100	833	52	1.69	100	100	7.5	762	76.2
1100	1000	64	3.39	100	100	30	381	38.1
4047	0	57	2.54	100	100	30	381	38.1
4047	0	62	3.39	100	100	30	381	38.1
4047	333	57	2.54	100	100	30	381	38.1
4047	333	63	3.39	100	100	30	381	38.1
4047	667	57	2.54	100	100	30	381	38.1
4047	667	60	3.39	100	100	30	381	38.1
4047	1000	54	2.54	100	100	30	381	38.1
4047	1000	54	2.54	100	100	30	381	38.1
4047	1000	60	3.39	100	100	30	381	38.1
6061	0	55	1.69	100	100	7.5	762	76.2
6061	0	60	2.54	100	100	30	762	38.1
6061	0	68	3.39	100	100	30	381	38.1
6061	167	55	1.69	100	100	7.5	762	76.2
6061	167	60	2.54	100	100	30	381	38.1
6061	333	55	1.69	100	100	7.5	762	76.2
6061	333	60	2.54	100	100	30	762	38.1
6061	333	68	3.39	100	100	30	381	38.1
6061	500	55-50	1.69	100	100	7.5	762	76.2
6061	500	60	2.54	100	100	30	381	38.1
6061	500	55	2.54	100	100	30	381	38.1
6061	667	50	1.69	100	100	7.5	762	76.2
6061	667	67	3.39	100	100	30	381	38.1
6061	833	50-45	1.69	100	100	7.5	762	76.2
6061	1000	67	3.39	100	100	30	381	38.1

Appendix B. Additional Data

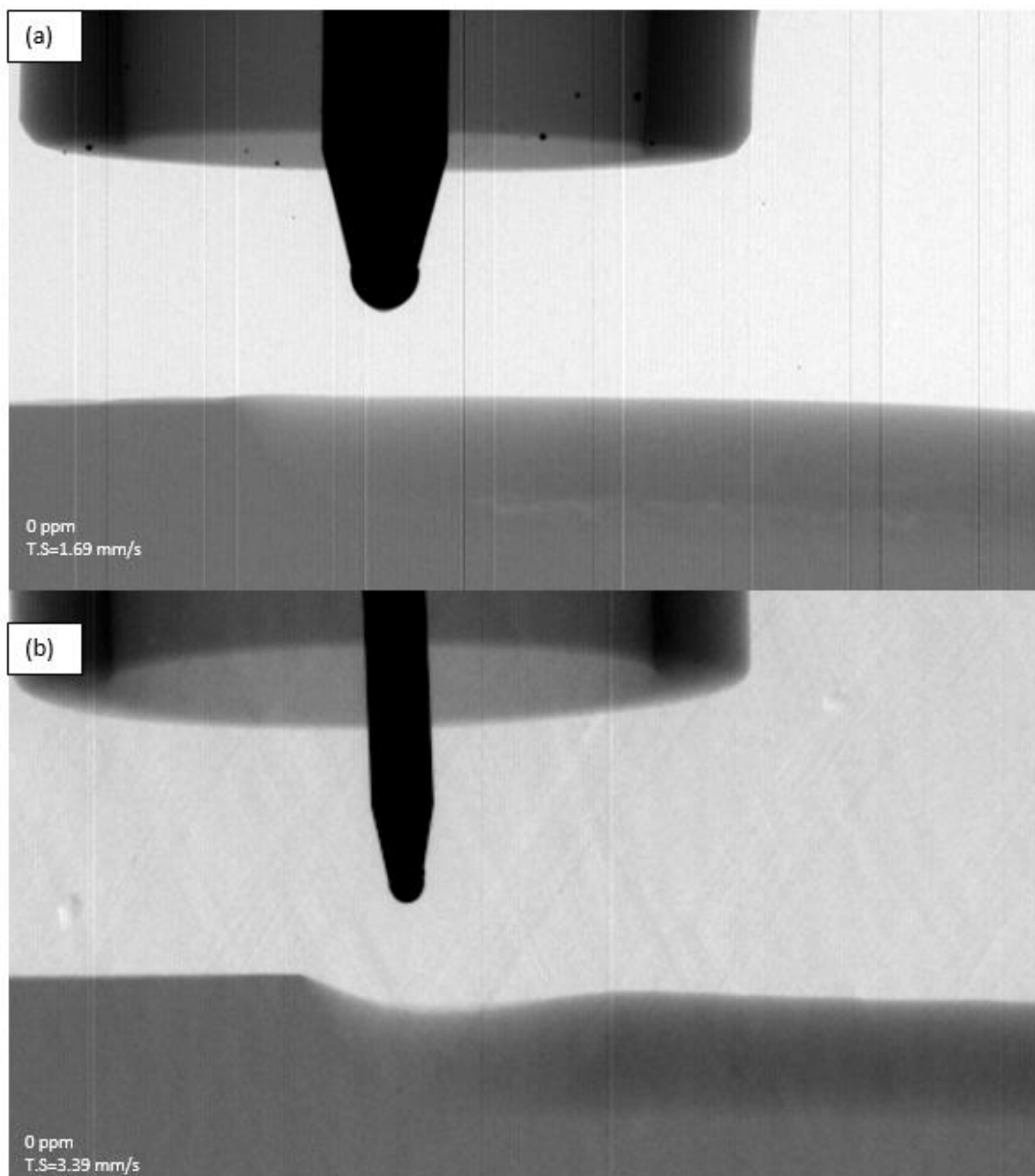


Figure 43: Alloy 1100 welded sample welded with 0 ppm of hydrogen at a) 1.69 mm/s and b) 3.39 mm/s.

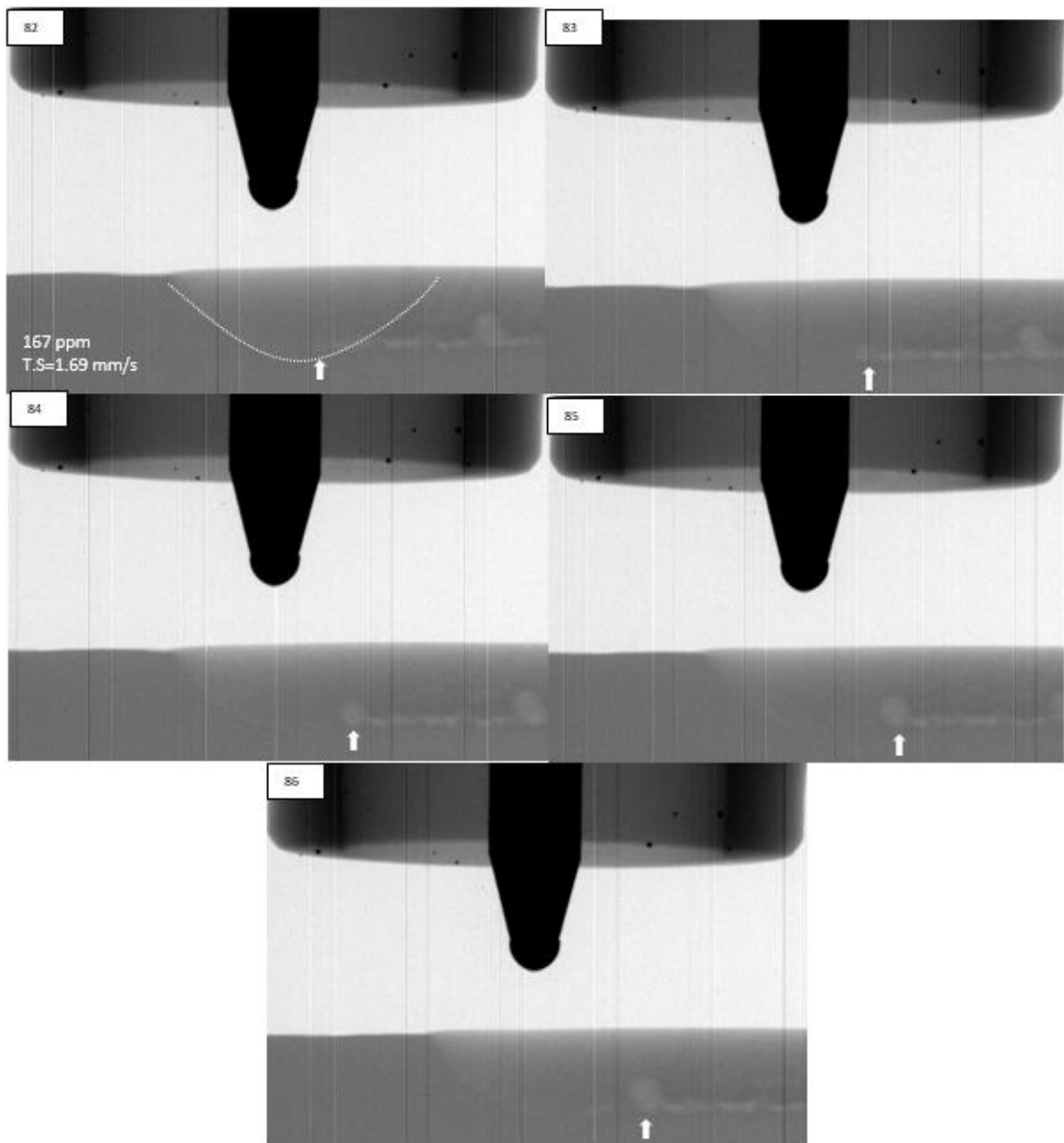


Figure 44: Alloy 1100 welded using 167 ppm of shielding gas hydrogen at 1.69 mm/s.

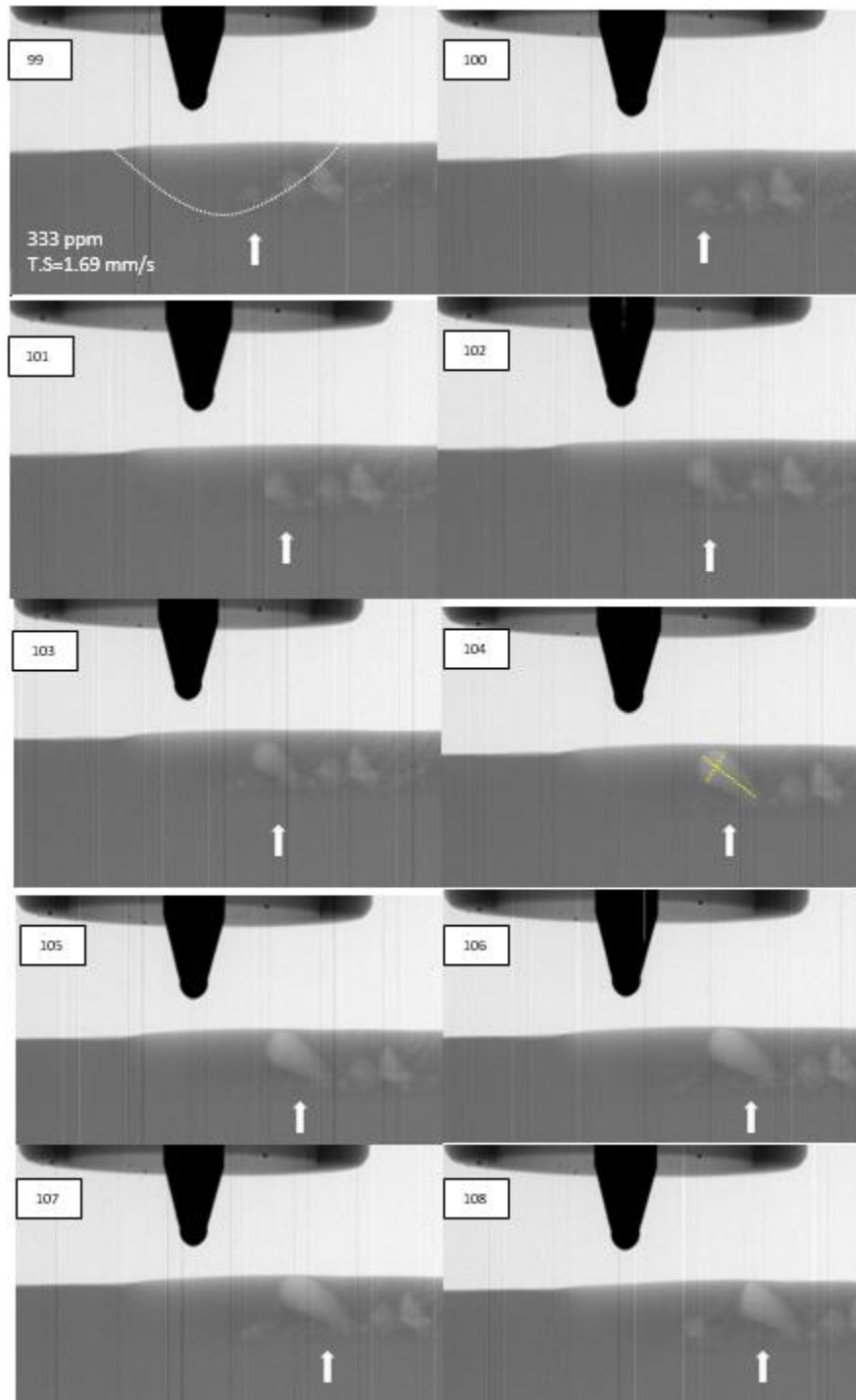


Figure 45: Alloy 1100 welded using 333 ppm of shielding gas hydrogen at 1.69 mm/s.

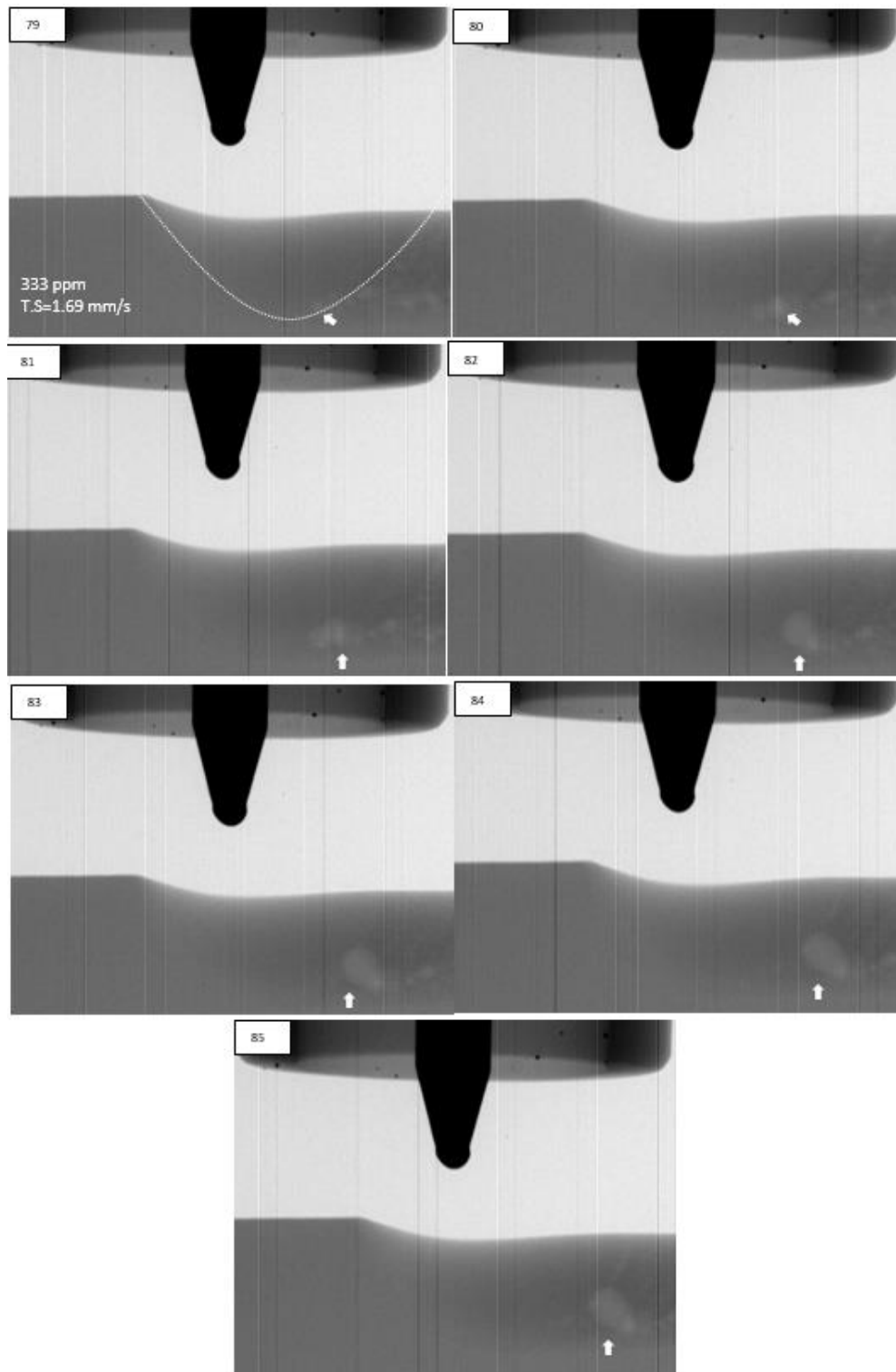


Figure 46: Alloy 1100 welded using 333 ppm of shielding gas hydrogen at 1.69 mm/s.

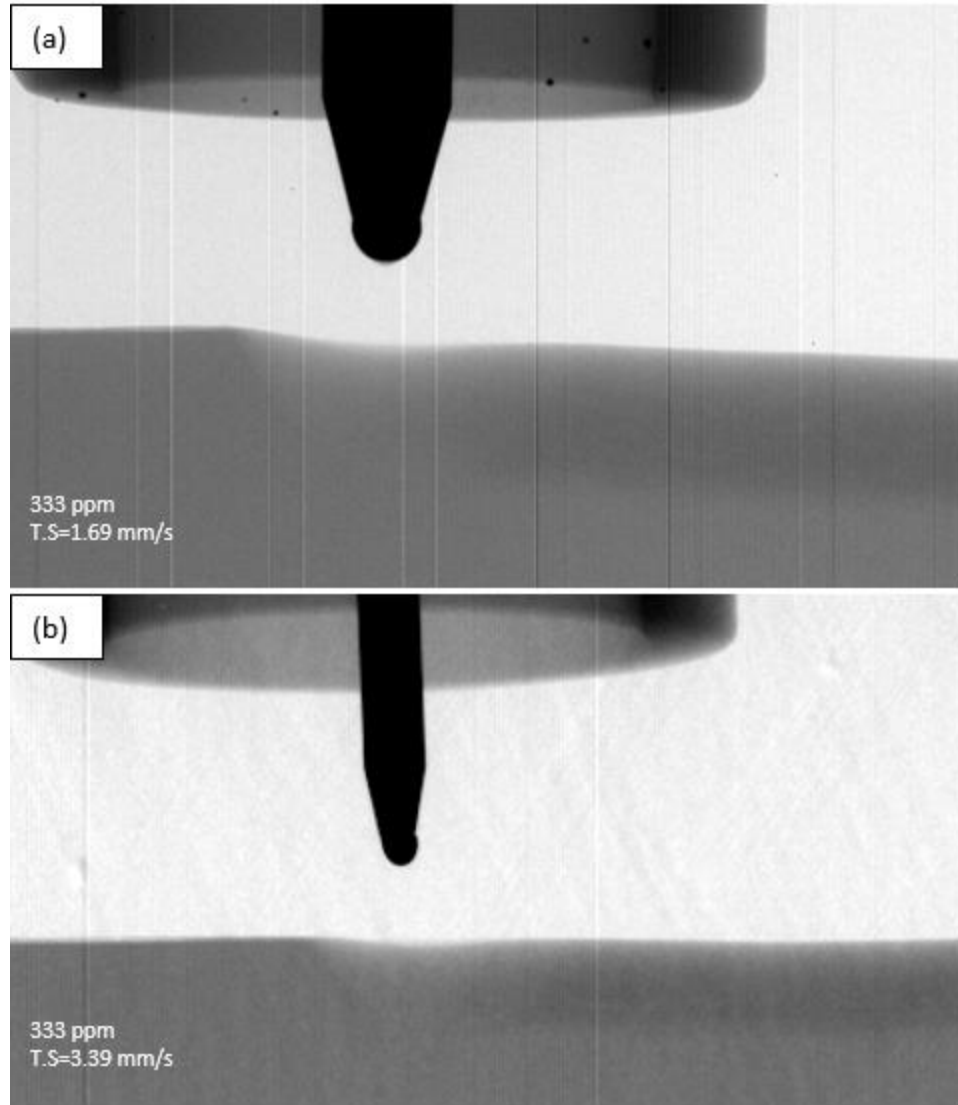


Figure 47: Alloy 1100 welded using 333 ppm of shielding gas hydrogen at a) 1.69 mm/s and b) 3.39 mm/s.

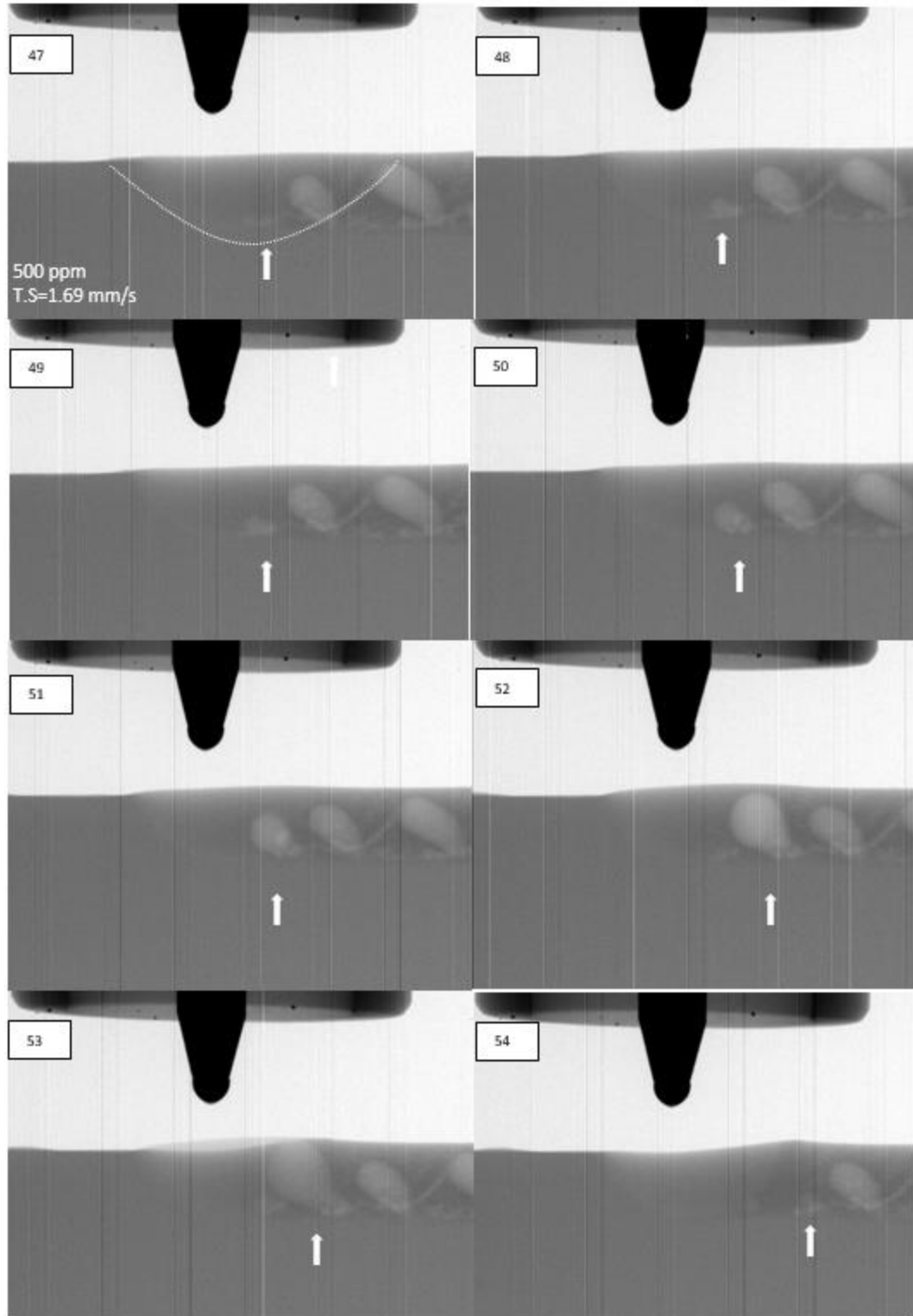


Figure 48: Alloy 1100 welded using 500 ppm of shielding gas hydrogen at 1.69 mm/s.

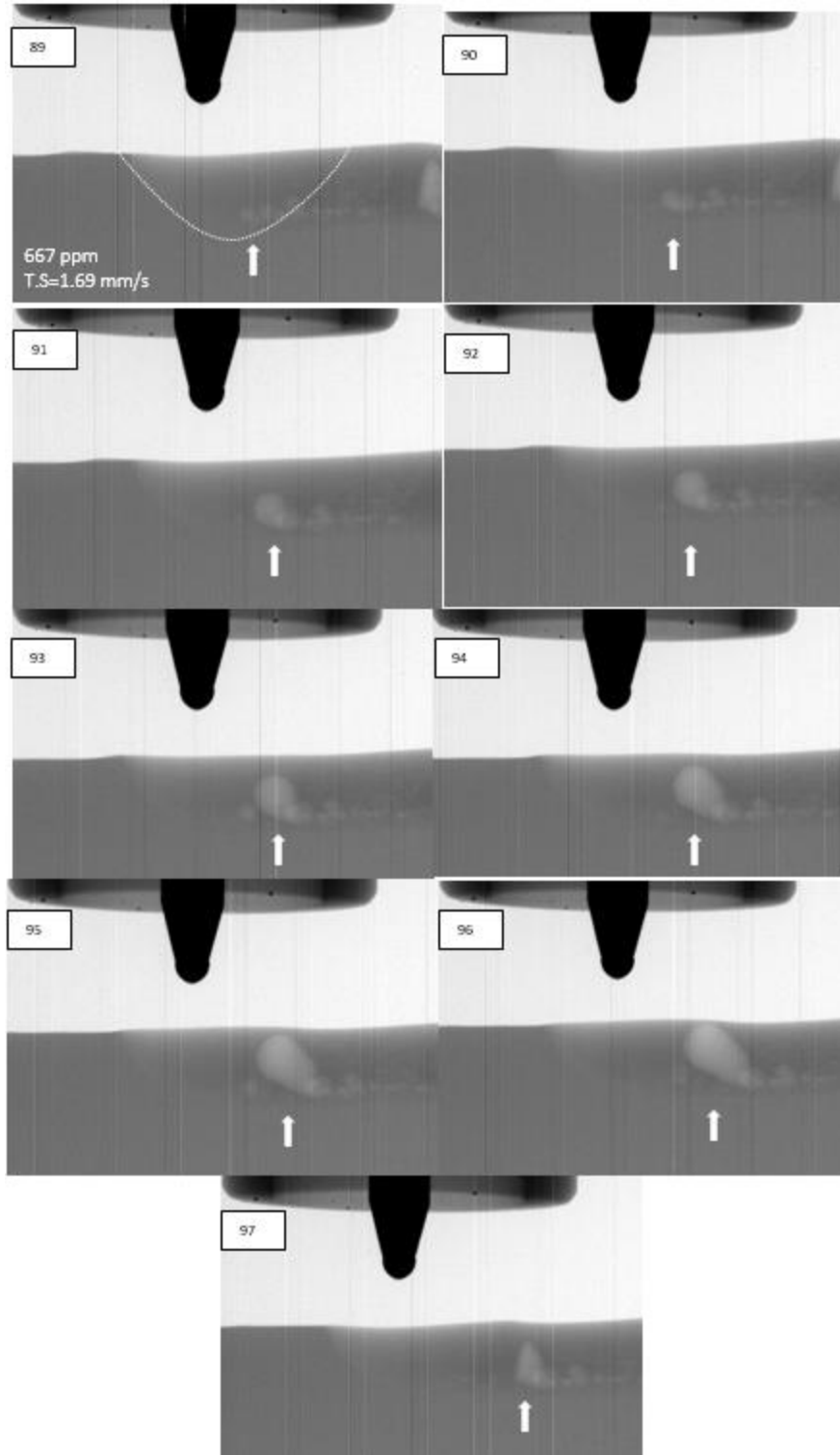


Figure 49: Alloy 1100 welded using 667 ppm of shielding gas hydrogen at 1.69 mm/s.

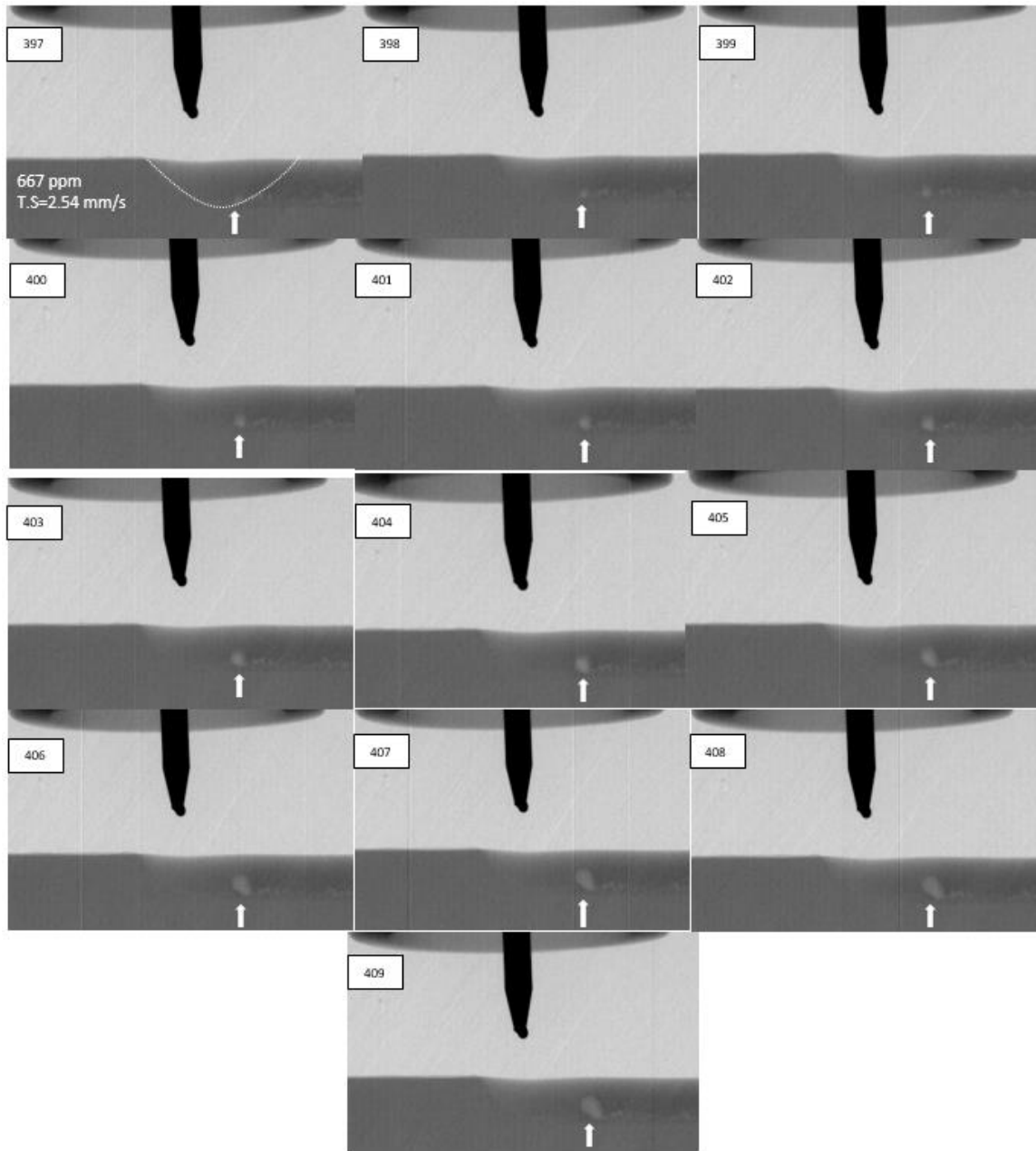


Figure 50: Alloy 1100 welded using 667 ppm of shielding gas hydrogen at 2.54 mm/s.

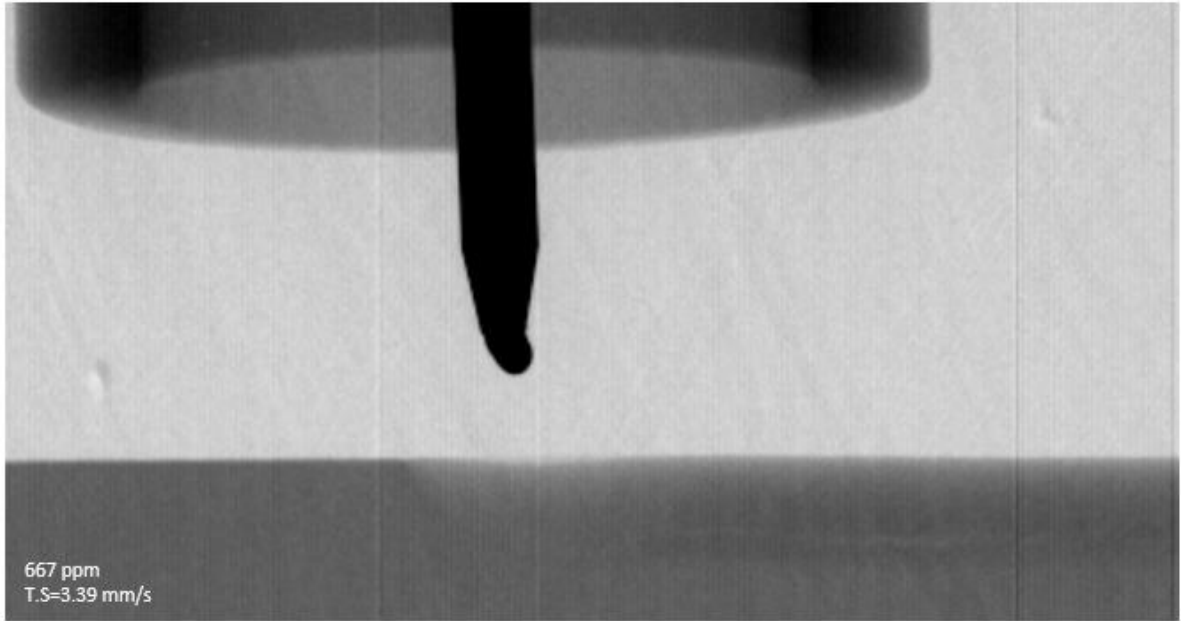


Figure 51: Alloy 1100 welded using 667 ppm of shielding gas hydrogen at 3.39 mm/s.

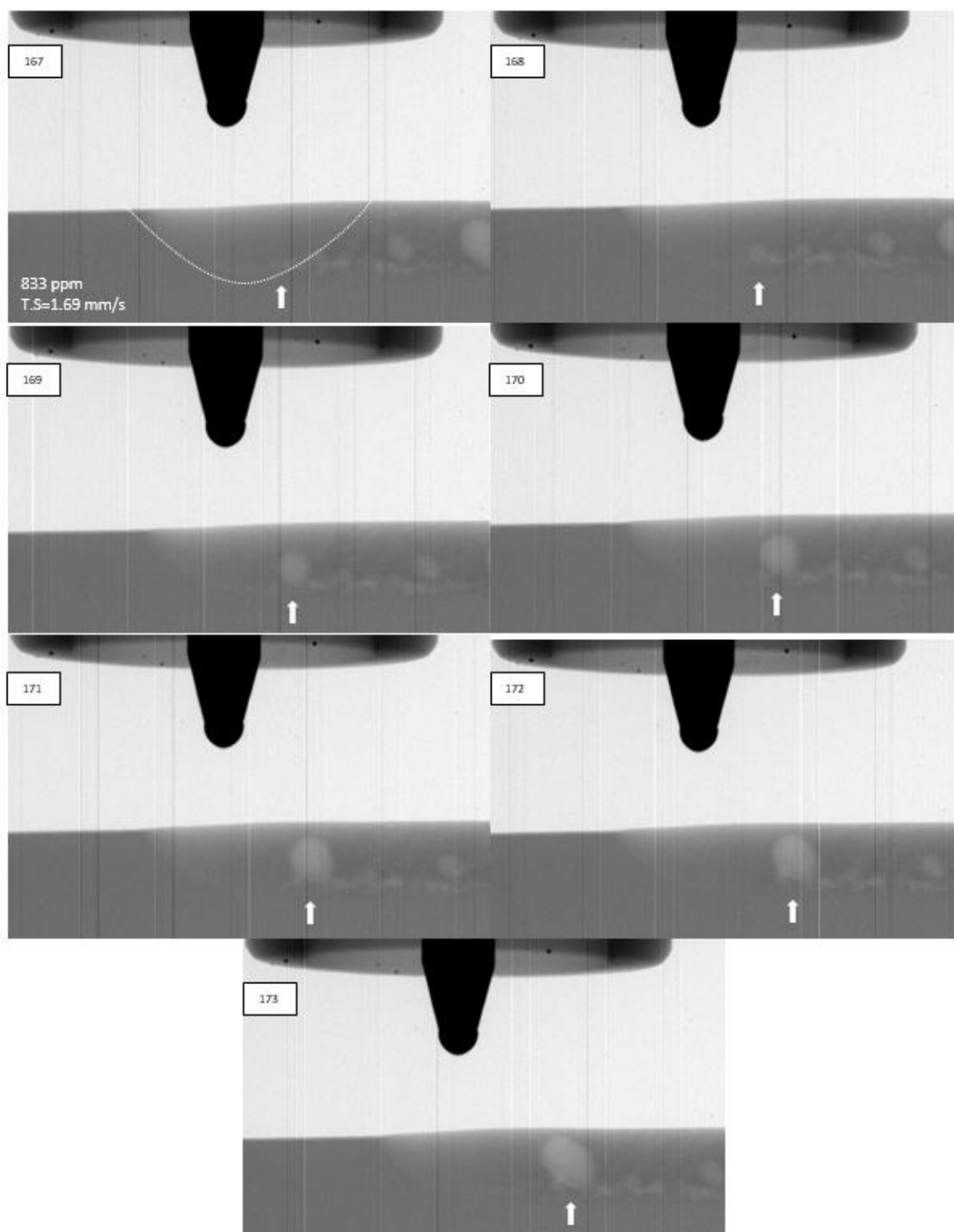


Figure 52: Alloy 1100 welded using 833 ppm of shielding gas hydrogen at 1.69 mm/s.

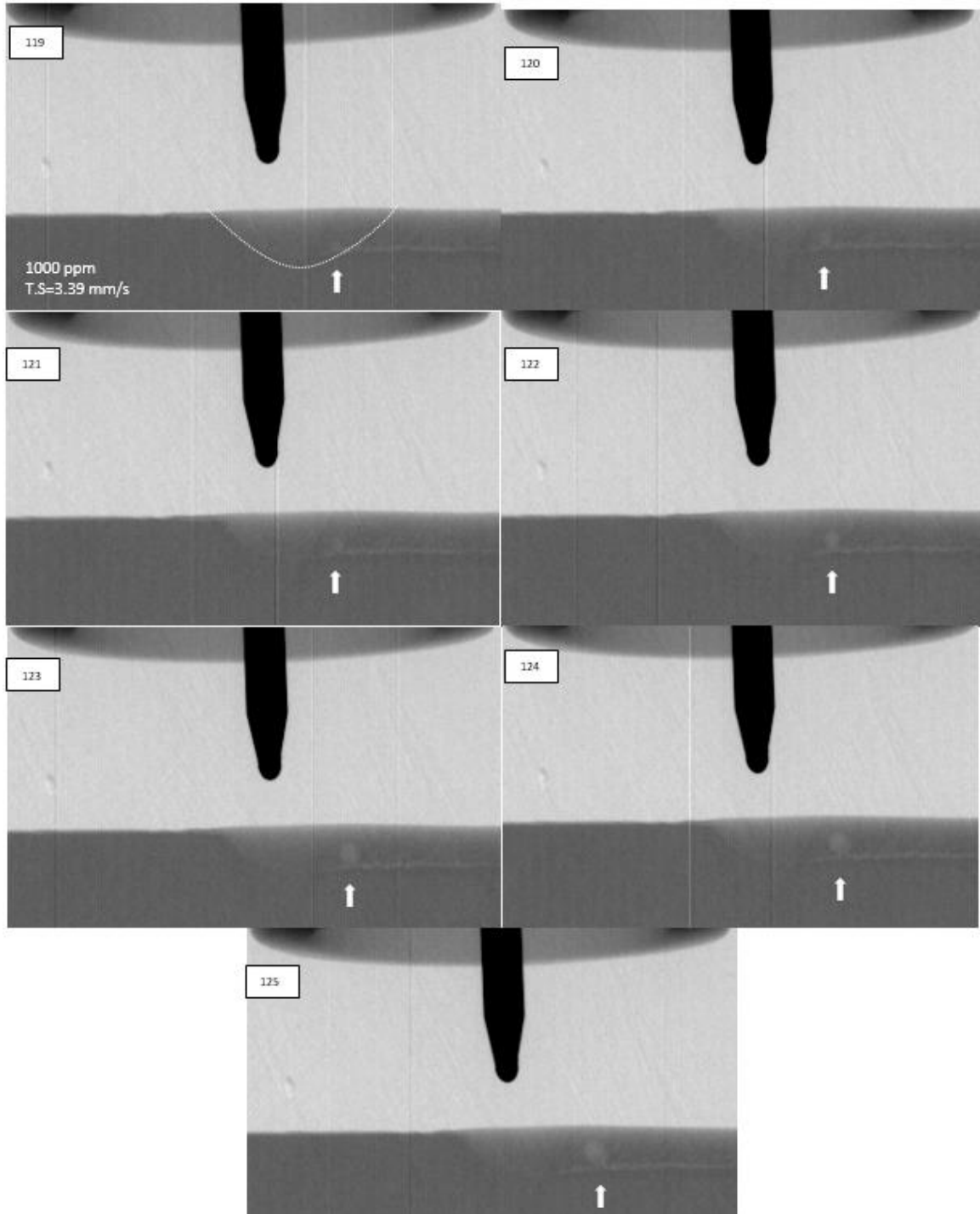


Figure 53: Alloy 1100 welded using 1000 ppm of shielding gas hydrogen at 3.39 mm/s.

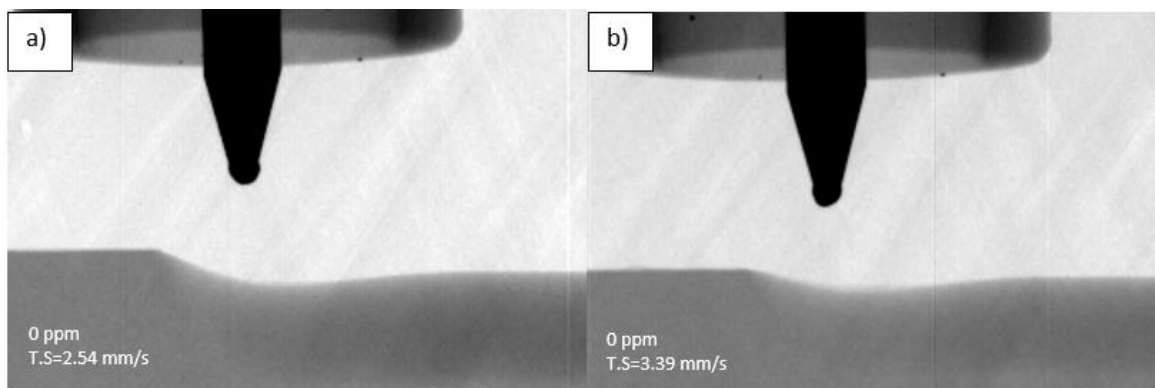


Figure 54: Alloy 4047 welded using 0 ppm of shielding gas hydrogen at a) 2.54 mm/s and b) 3.39 mm/s.

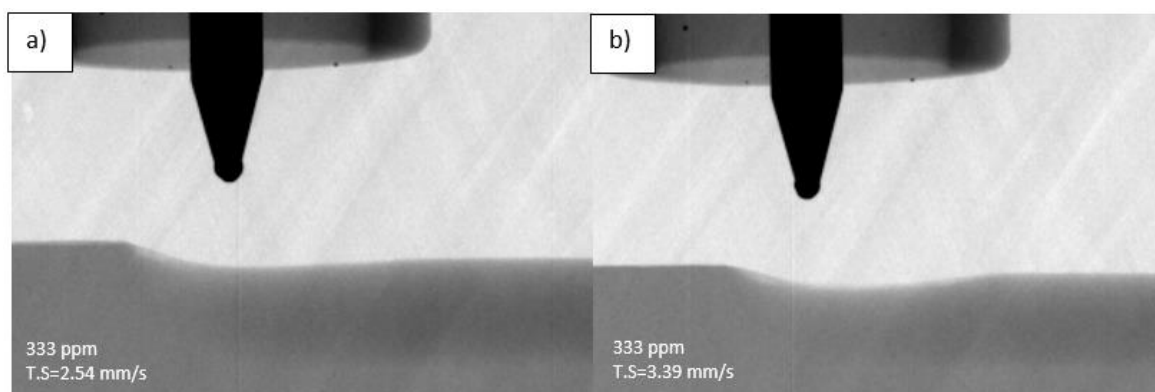


Figure 55: Alloy 4047 welded using 333 ppm of shielding gas hydrogen at a) 2.54 mm/s and b) 3.39 mm/s.

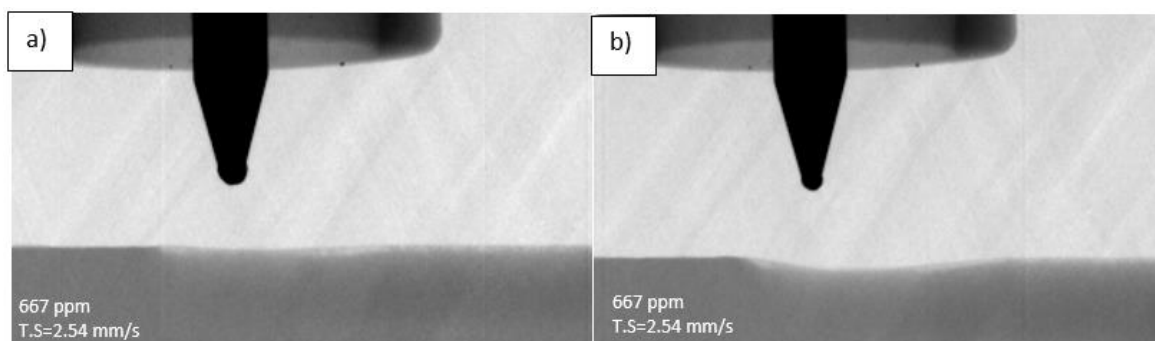


Figure 56: Alloy 4047 welded using 667 ppm of shielding gas hydrogen at a) 2.54 mm/s and b) 3.39 mm/s.

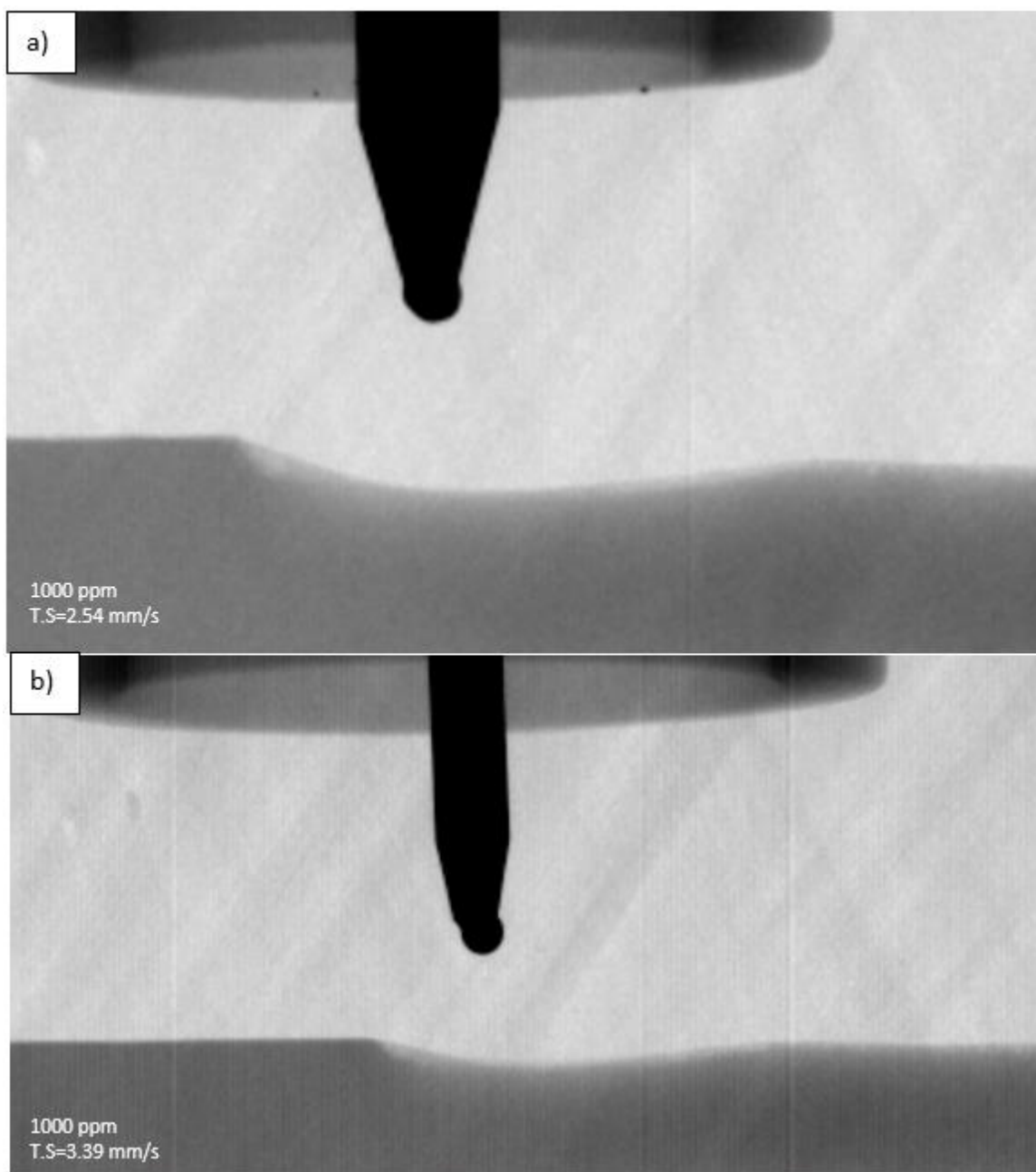


Figure 57: Alloy 4047 welded using 1000 ppm of shielding gas hydrogen at a) 2.54 mm/s and b) 3.39 mm/s.

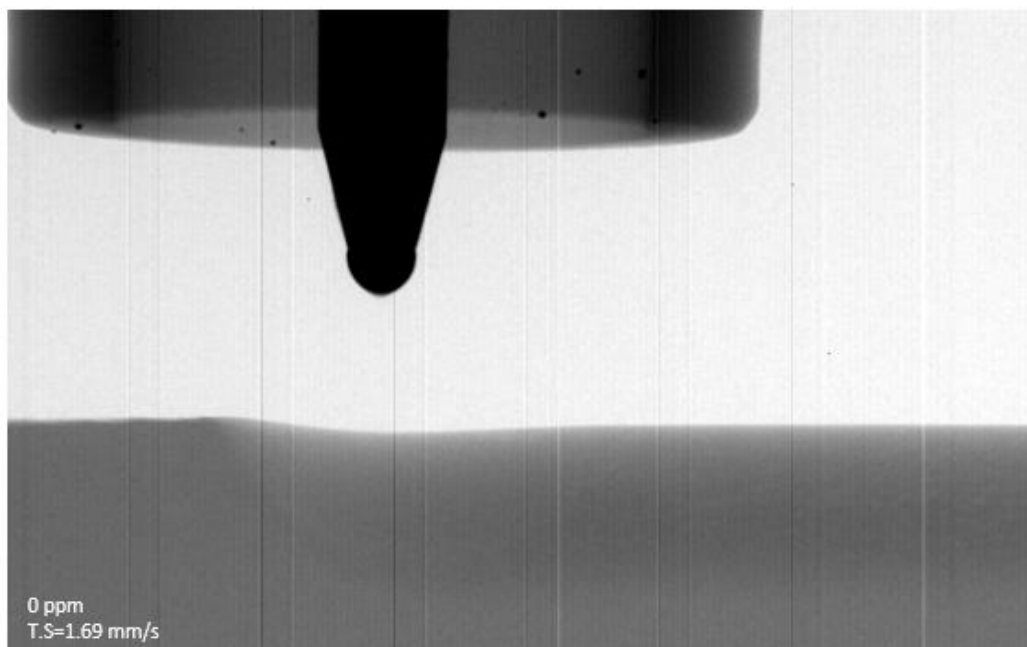


Figure 58: Alloy 6061 welded using 0 ppm of shielding gas hydrogen at 1.69 mm/s

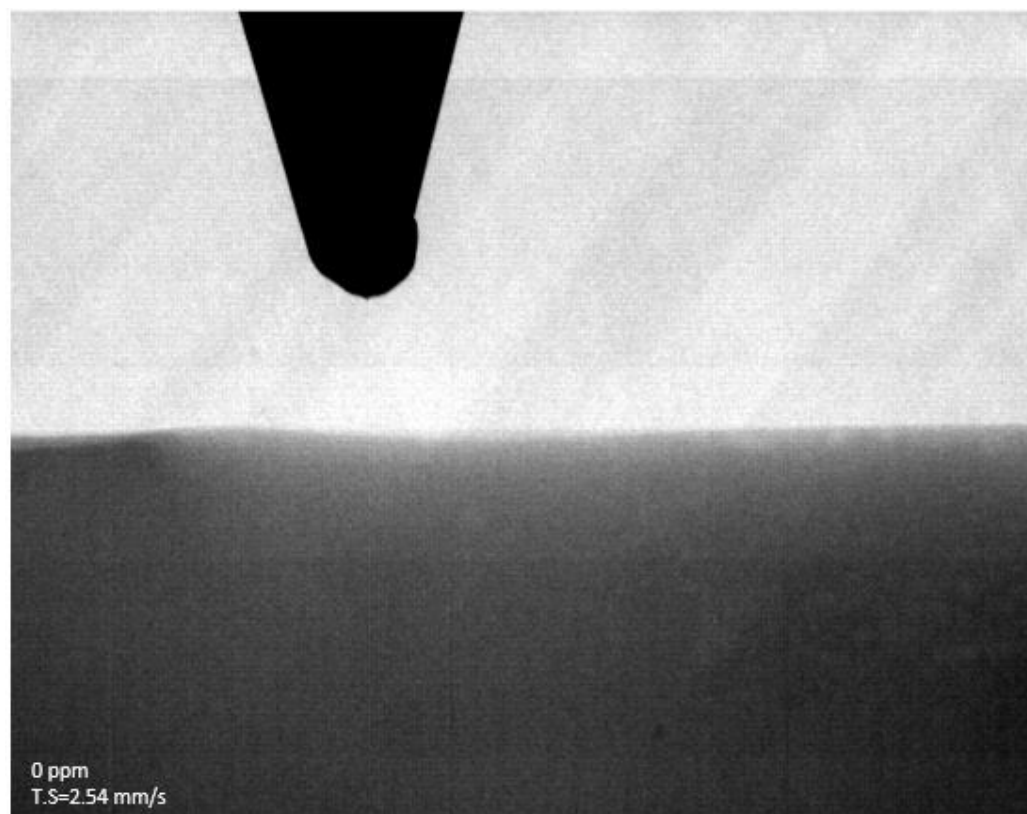


Figure 59: Alloy 6061 welded using 0 ppm of shielding gas hydrogen at 2.54 mm/s.

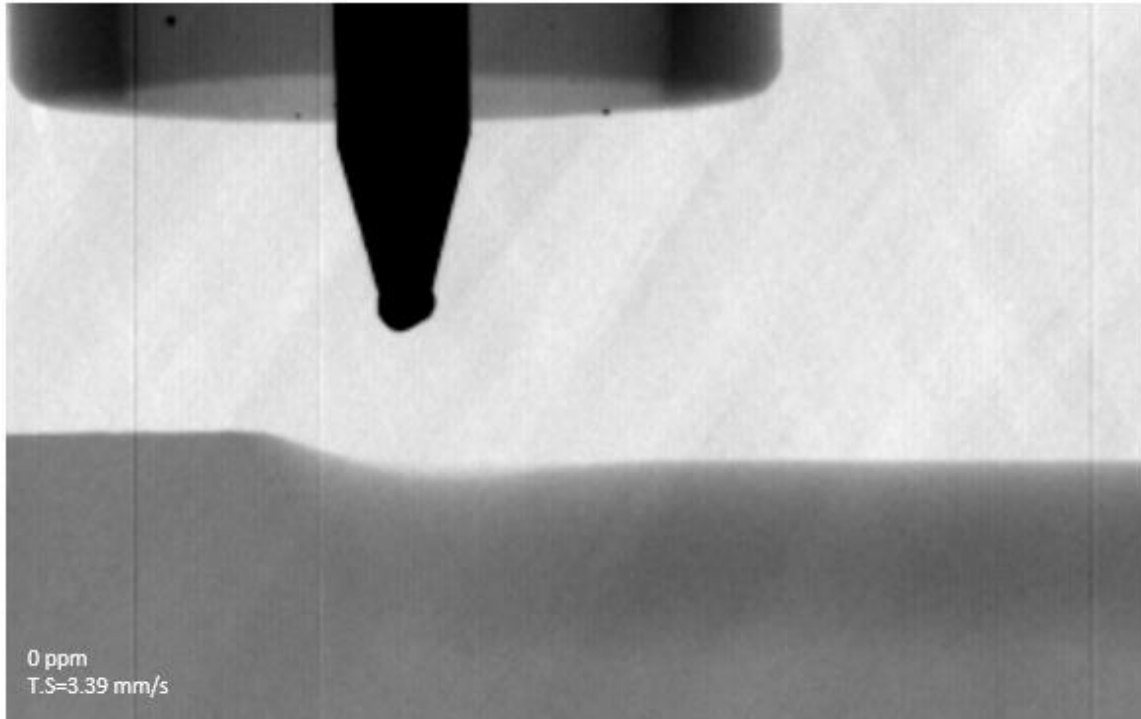


Figure 60: Alloy 6061 welded using 0 ppm of shielding gas hydrogen at 3.39 mm/s.

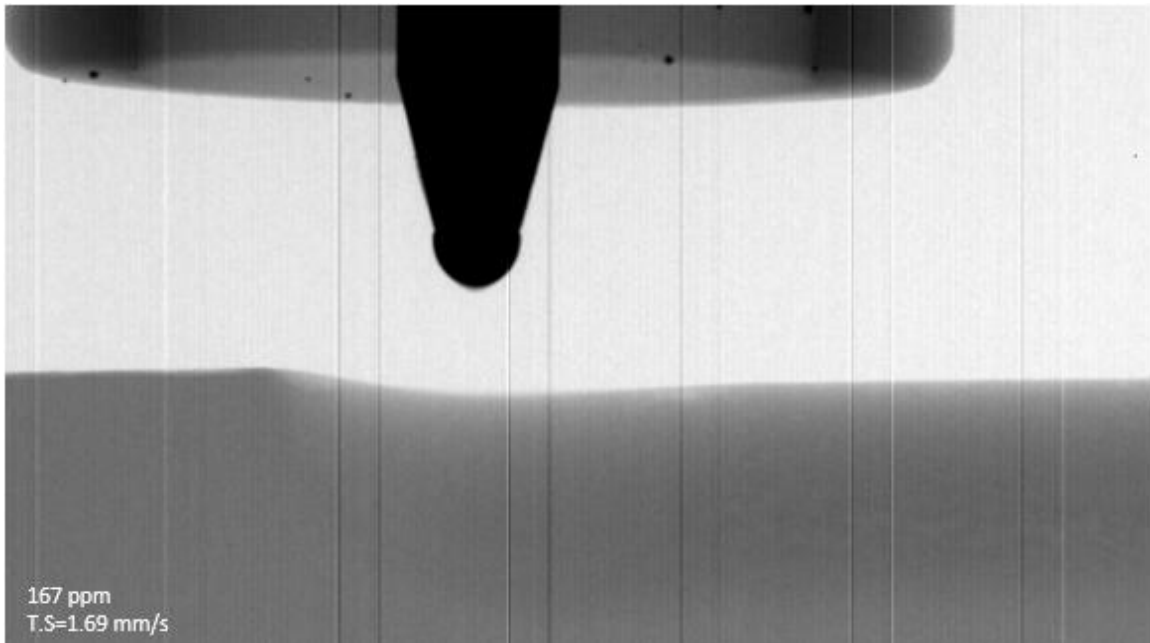


Figure 61: Alloy 6061 welded using 167 ppm of shielding gas hydrogen at 1.69 mm/s.

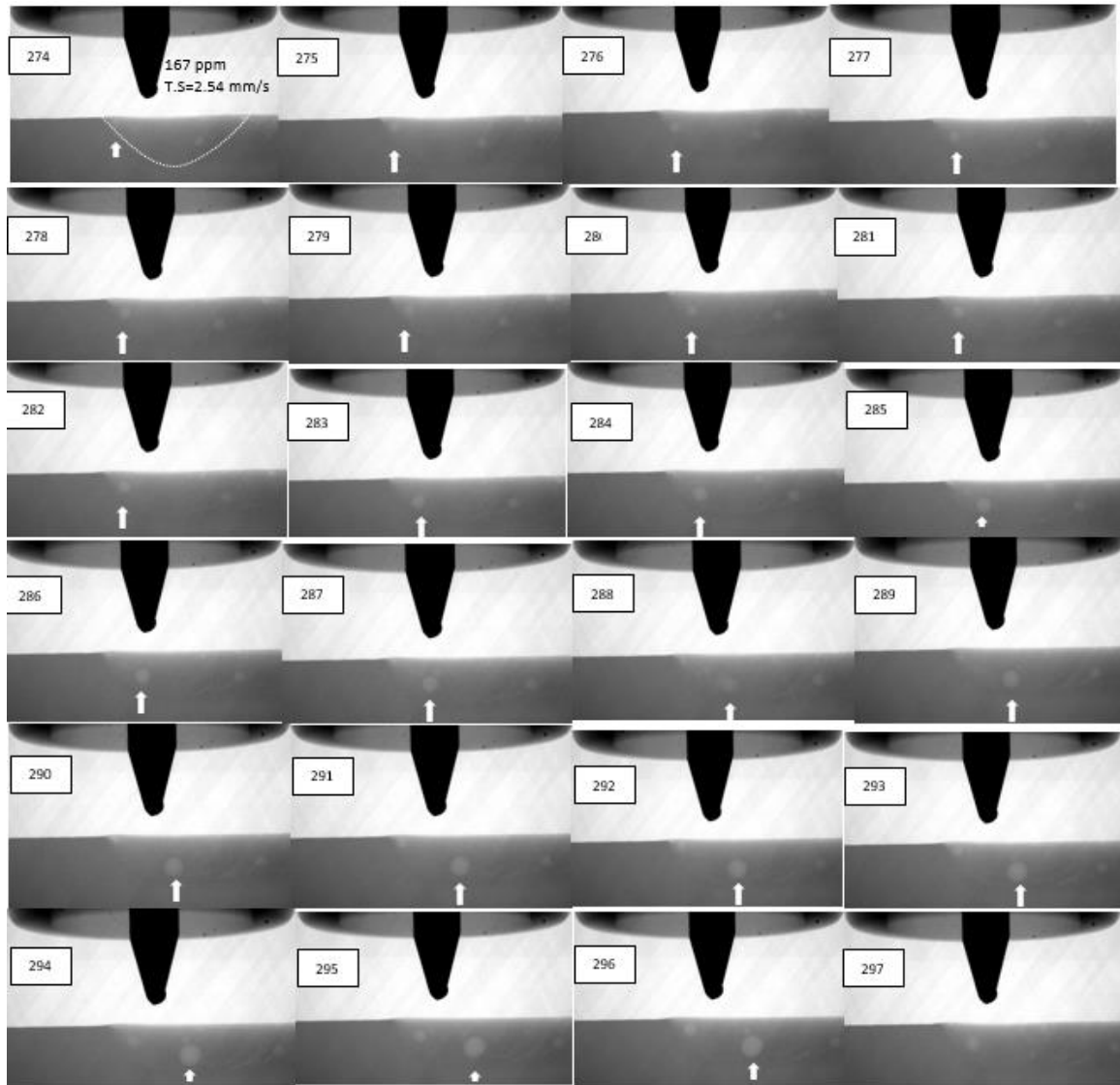


Figure 62: Alloy 6061 welded using 167 ppm of shielding gas hydrogen at 2.54 mm/s.

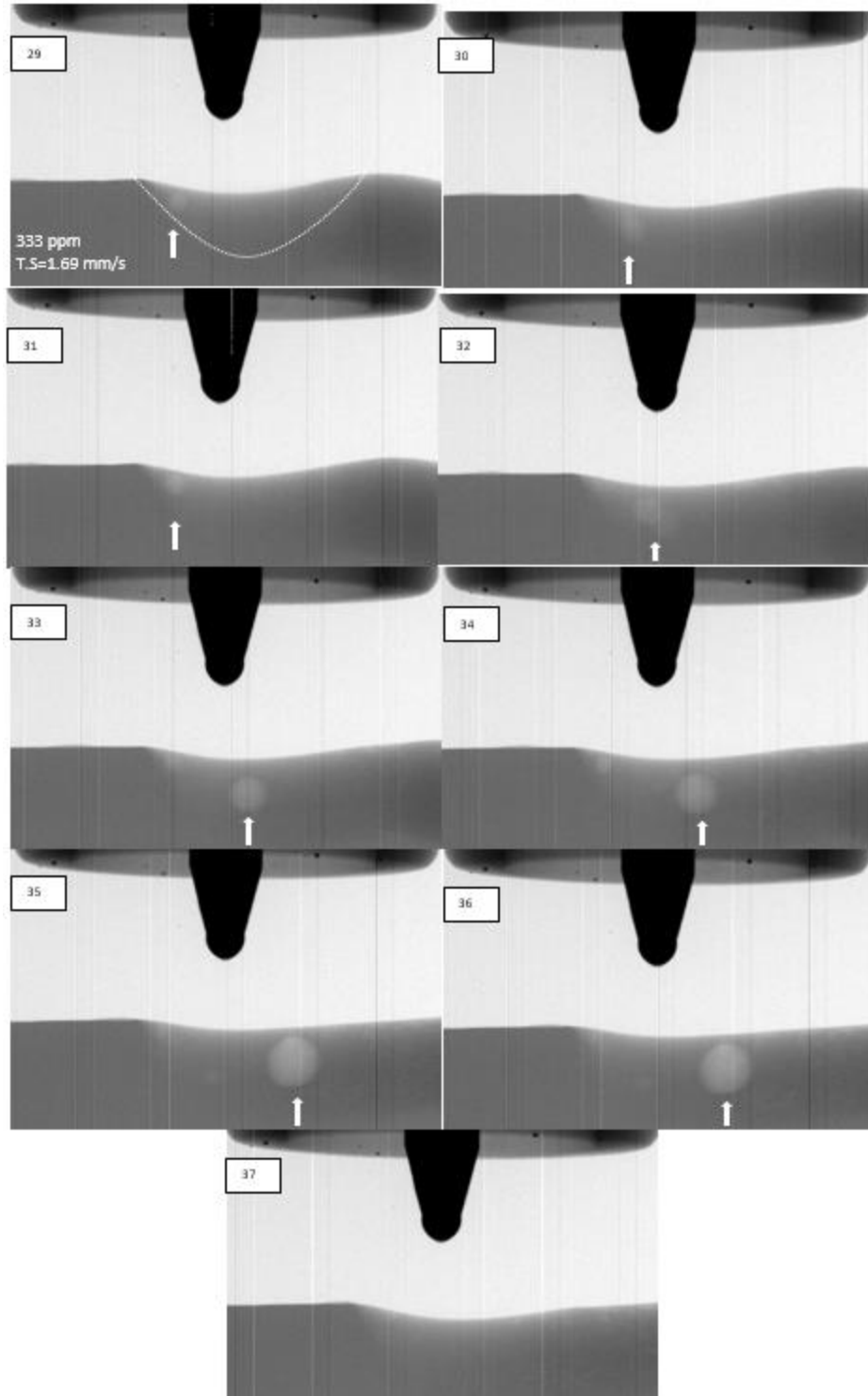


Figure 63: Alloy 6061 welded using 333 ppm of shielding gas hydrogen at 1.69 mm/s.

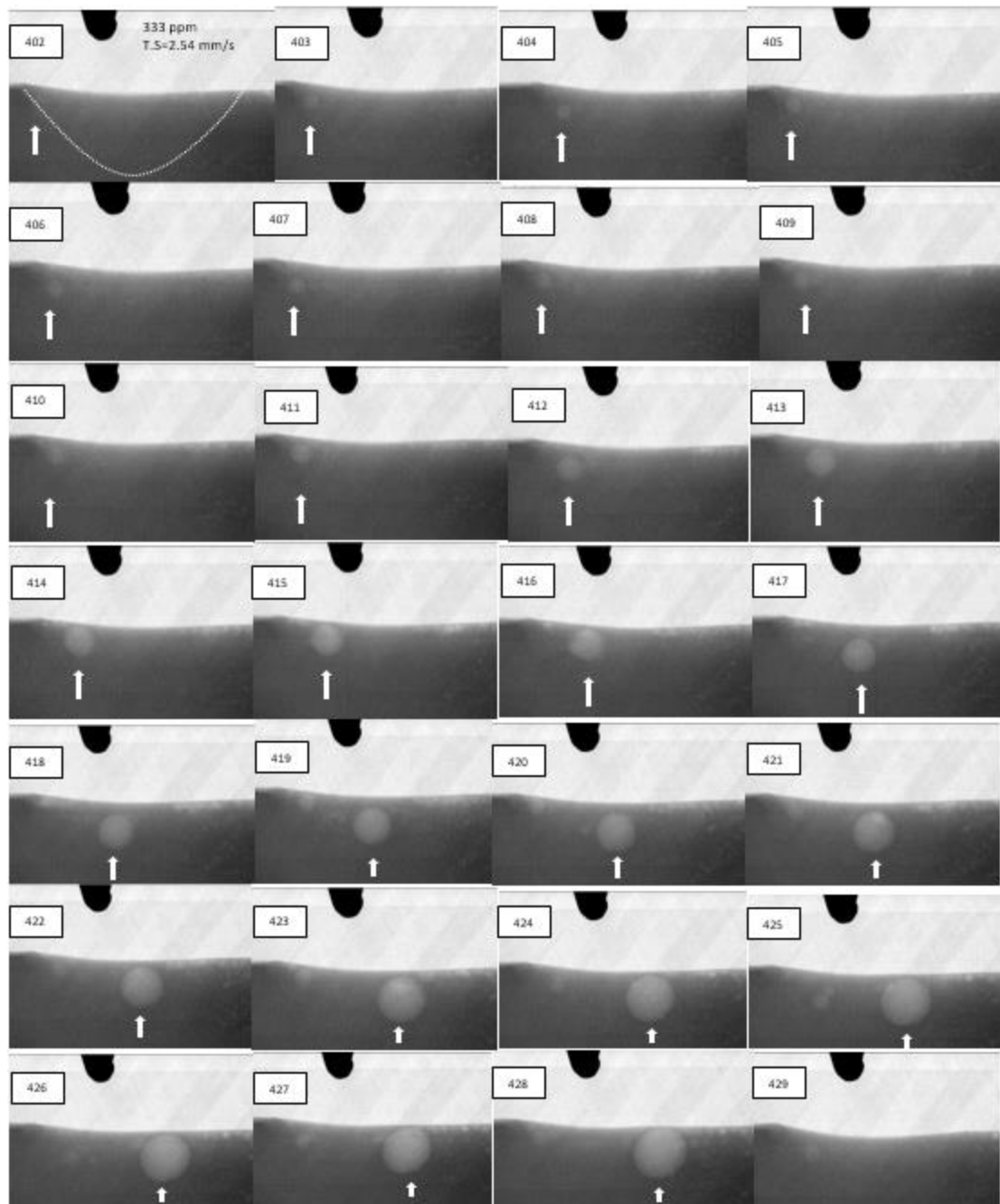


Figure 64: Alloy 6061 welded using 333 ppm of shielding gas hydrogen at 2.54 mm/s.

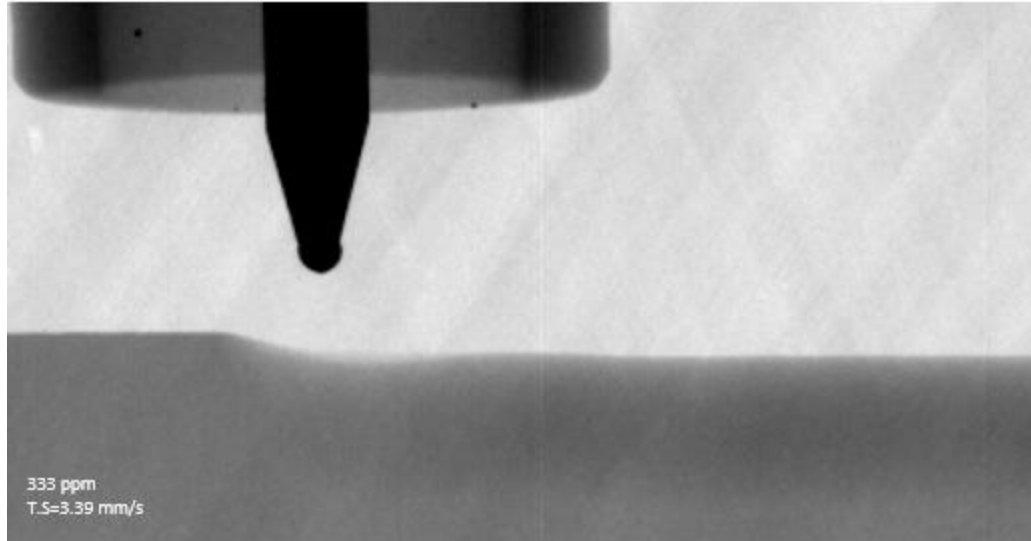


Figure 65: Alloy 6061 welded using 333 ppm of shielding gas hydrogen at 3.39 mm/s.

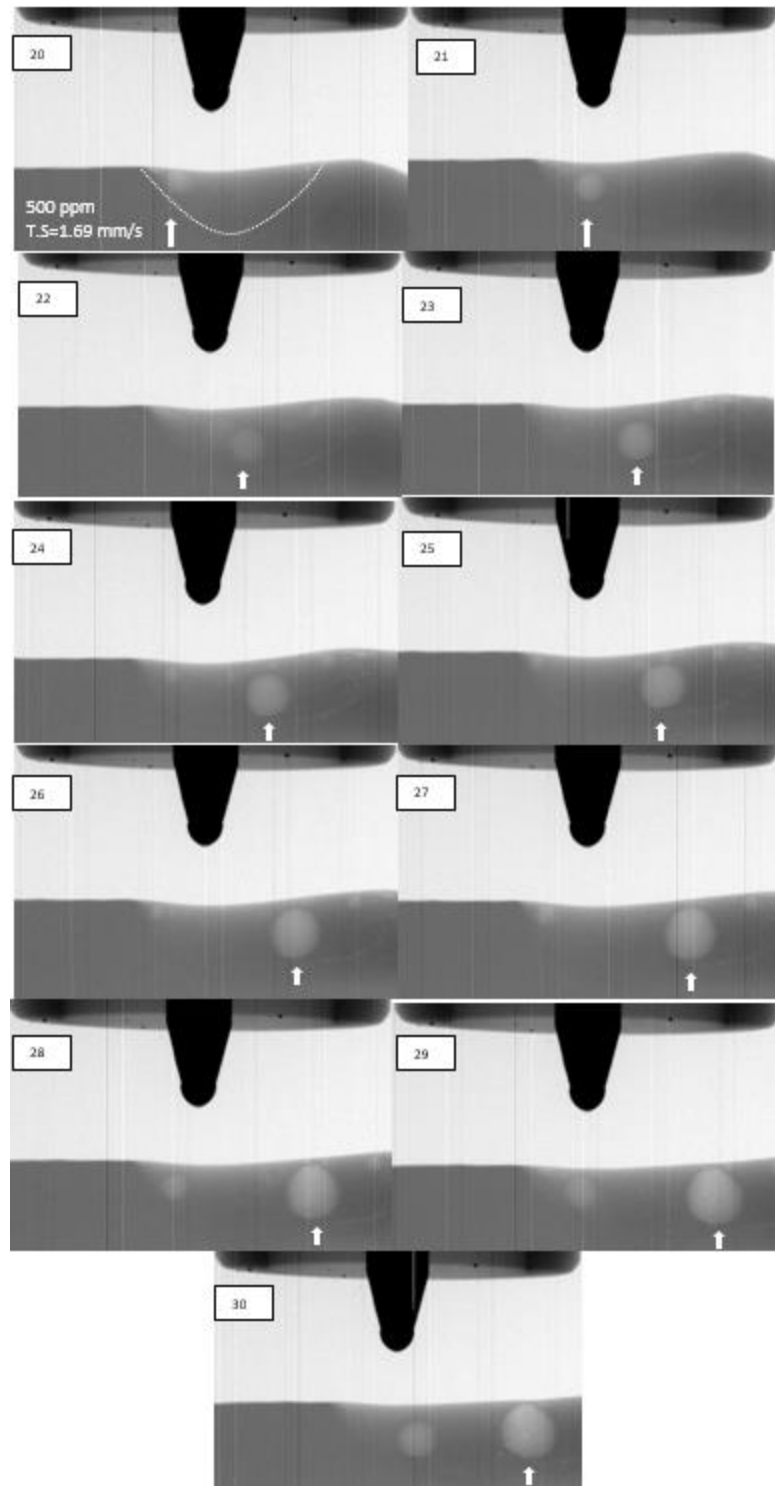


Figure 66: Alloy 6061 welded using 500 ppm of shielding gas hydrogen at 1.69 mm/s.

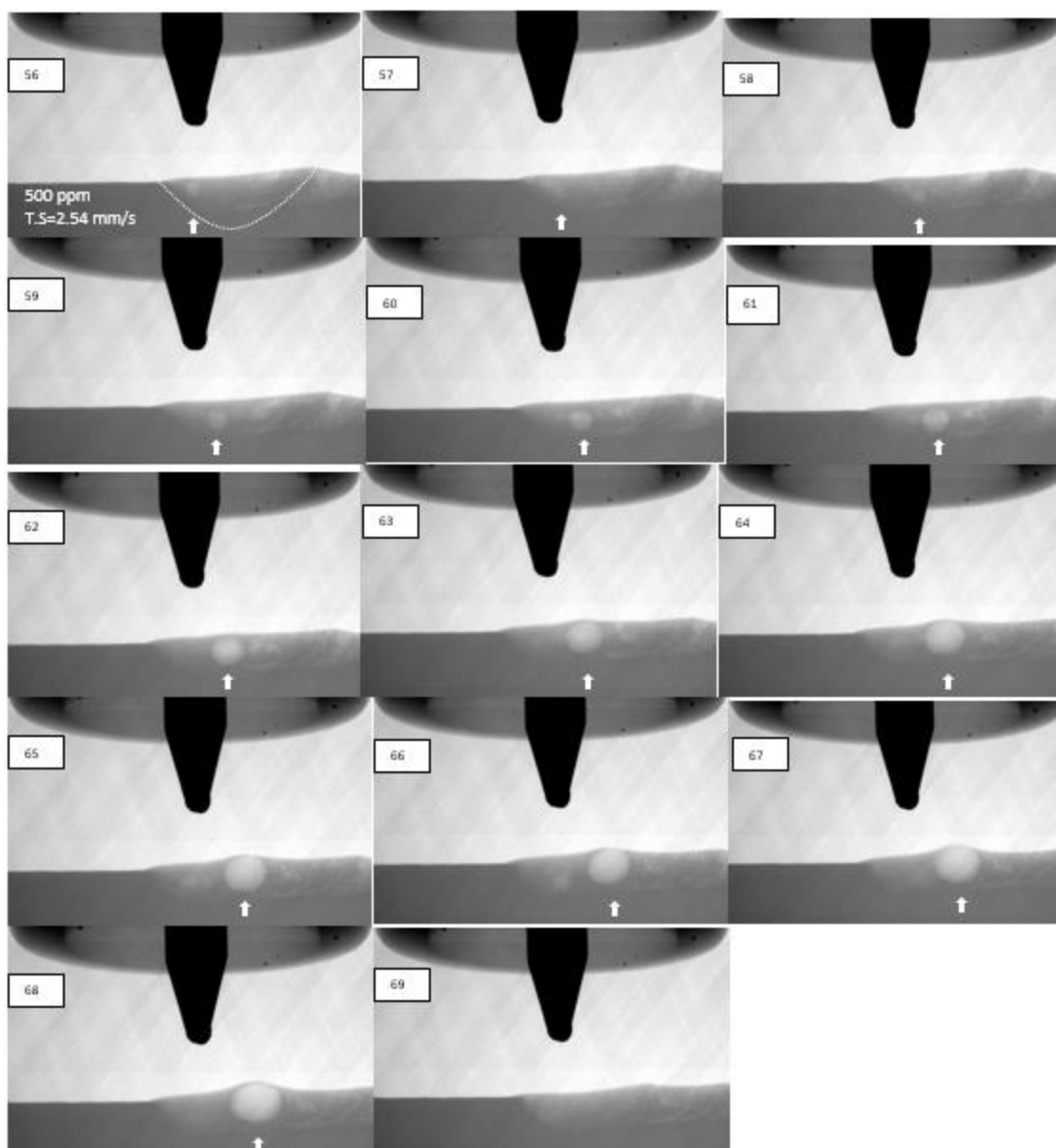


Figure 67: Alloy 6061 welded using 500 ppm of shielding gas hydrogen at 2.54 mm/s.

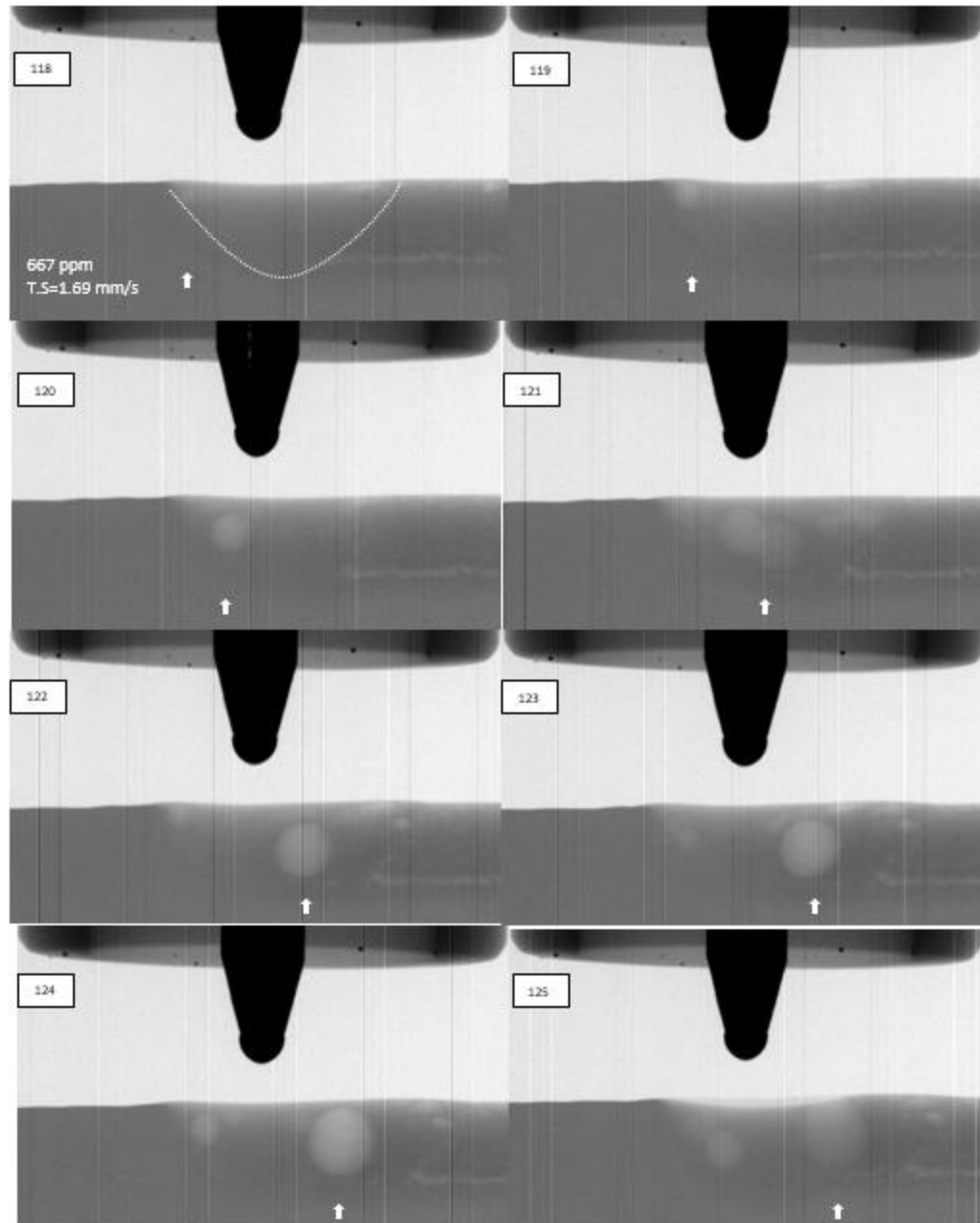


Figure 68: Alloy 6061 welded using 667 ppm of shielding gas hydrogen at 1.69 mm/s.

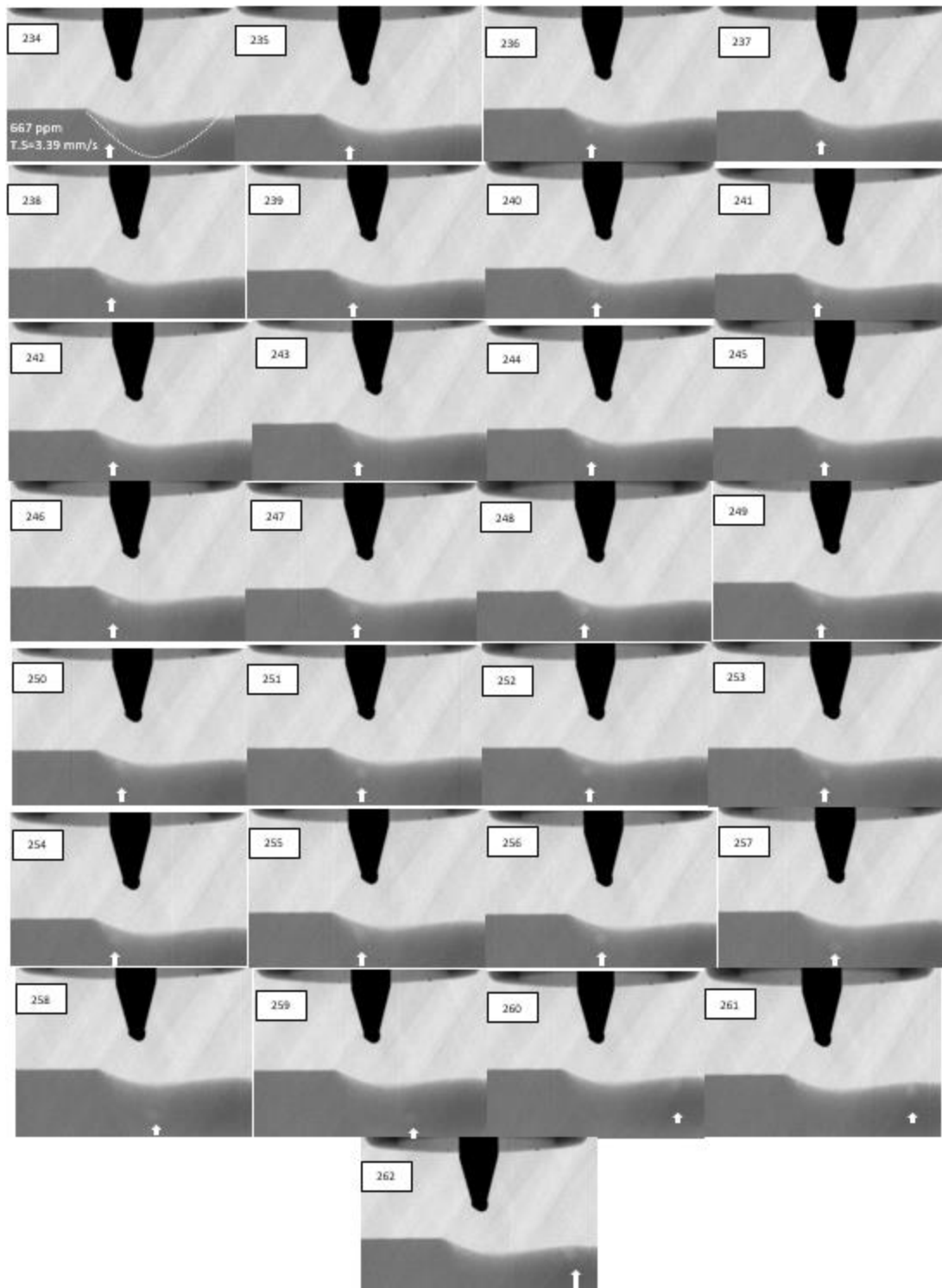


Figure 69: Alloy 6061 welded using 667 ppm of shielding gas hydrogen at 3.39 mm/s.

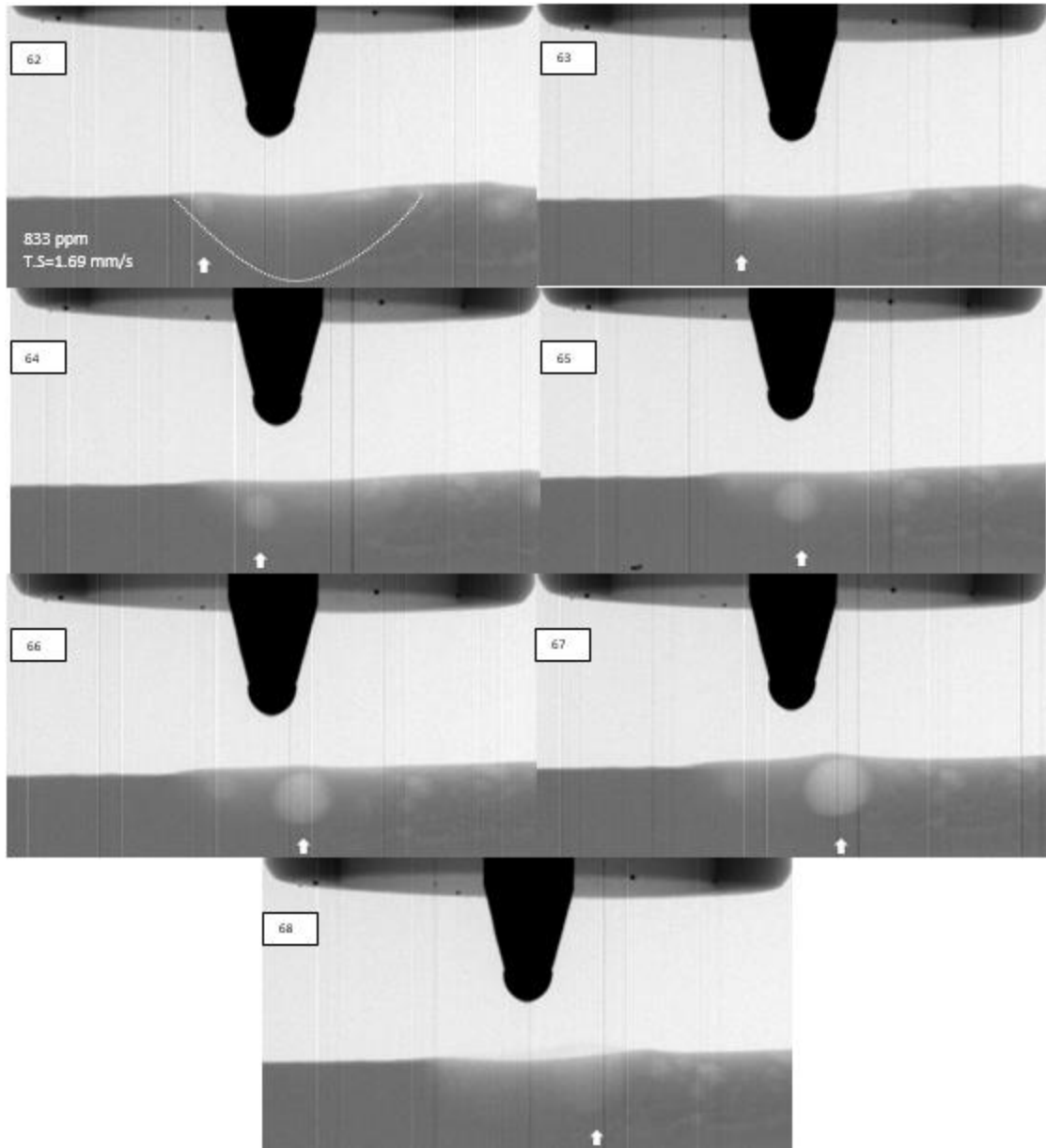


Figure 70: Alloy 6061 welded using 833 ppm of shielding gas hydrogen at 1.69 mm/s.

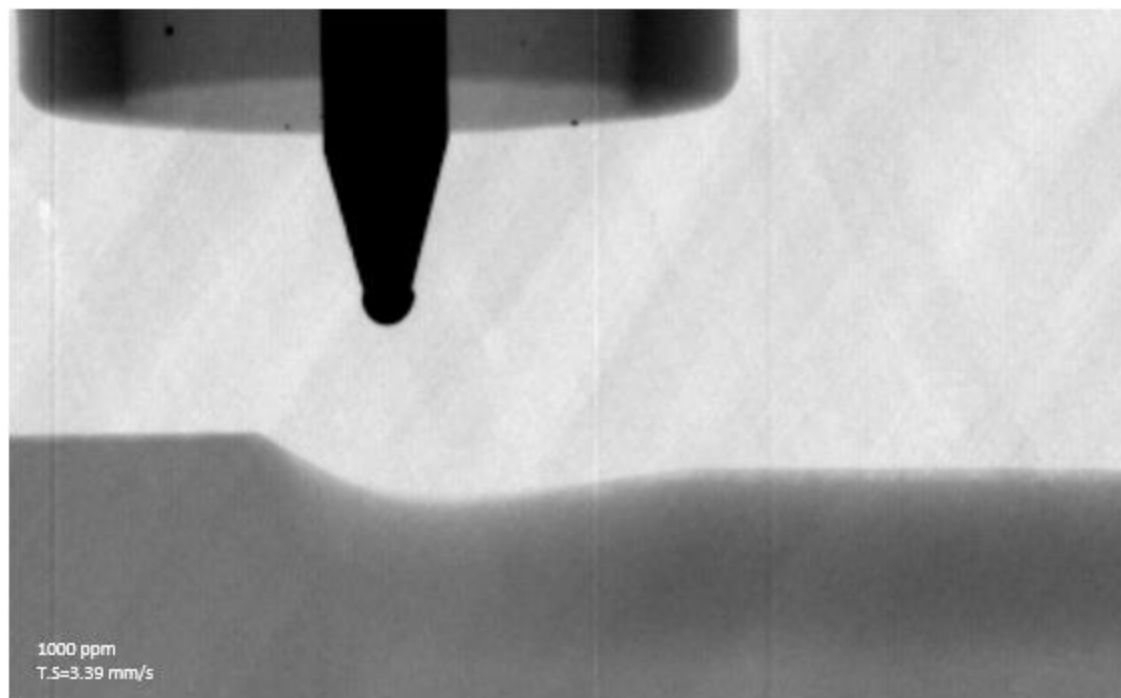


Figure 71: Alloy 6061 welded using 1000 ppm of shielding gas hydrogen at 3.39 mm/s